I. STRUCTURAL EFFECTS OF CARBOHYDRATE-CONTAINING POLYCATIONS ON GENE DELIVERY

II. DEVELOPMENT OF A NANOPARTICLE-BASED MODEL DELIVERY SYSTEM TO GUIDE THE RATIONAL DESIGN OF GENE DELIVERY TO THE LIVER

Thesis by

Stephen R. Popielarski

In Partial Fulfillment of the Requirements for the

Degree of

Doctor of Philosophy

CALIFORNIA INSTITUTE OF TECHNOLOGY

Pasadena, California

2005

(Defended March 4, 2005)

To Marci,
for always believing in me

Acknowledgements

I would like to begin by recognizing my advisor, Mark Davis, for giving me the freedom over the years to chart my own course, wherever it led. My experiences while at Caltech allowed me to discover aspects of my personality that I didn't realize existed, and for this I am truly grateful. Mark's constant flurry of great ideas has always been inspirational, as has his desire to solve some of the world's greatest problems.

Ken Pickar and Chris Halliwell have been great mentors to me and have had a profound influence on my vision of myself in the future. Despite Ken's extremely busy schedule, he has always found time to lend an ear whenever asked. Through many hours of conversation, Ken has pushed me to think and dream big and has provided ongoing encouragement to support my missteps along the way. Ken's willingness to share his vast network of contacts has benefited me immensely many times, and I look forward to being a valuable resource to Ken's students in the future.

Within a month of having Chris Halliwell as a mentor, she had more confidence in me than I had in myself. At times when I doubted myself, a simple call to Chris managed to prop me back up and prime me to push forward again. Chris also gave me invaluable advice on how to handle a variety of situations in which I found myself. I am finding that it is the soft skills that are so difficult to summarize.

My colleagues in the Davis lab, both past and present, have supported me in countless ways during my time here. My friends outside of Caltech have also been more understanding of my situation than I possibly could have asked. Thanks for always being there for me!

I would also like to thank some of the people who contributed technically to my projects. Siwen Hu was always available when I had questions, and she taught me just about everything I know about immunohistochemistry and working with mice. Samuel French acquired the TEM images of liver sections shown in this thesis and entertained me with many helpful discussions. Tim Triche provided encouragement along the way as well as expert analysis of the immunohistochemistry images. Shelley Diamond went out of her way to assist with my *in vitro* FACS experiments. Hide Tsukamoto generously isolated non-parenchymal liver cells for my project. And I thank George McNamara of the CHLARI Image Core for advice and assistance acquiring images following immunohistochemical staining.

Finally, everything that I have done over the past six years has been possible thanks to the support of my wonderful wife, Marci. I cannot even imagine where I would be right now without you.

Abstract

Linear cationic β-cyclodextrin (β-CD)-based polymers can bind with plasmid DNA to form colloid-sized composite particles (denoted as polyplexes) that are able to transfect cultured cells. The effectiveness of gene delivery and the cellular toxicity have been related to structural features of the polycation. β-CD polycations are prepared by the co-condensation of $6^A,6^D$-dideoxy-$6^A,6^D$-diamino-β-CD monomers with other difunctionalized monomers such as dimethylsuberimidate (DMS). In the first part of this thesis, synthetic variations of the β-CD structure are used to probe structure-function gene delivery properties. The type of cyclodextrin and its functionalization are investigated by synthesizing numerous $3^A,3^B$-dideoxy-$3^A,3^B$-diamino-β- and γ-CD monomers. Both alkyl- and alkoxy-diamines are prepared in order to vary the nature of the spacing between the CD and the primary amines in the CD monomers. These diamino-CD-monomers are polymerized with DMS to yield amidine-based polycations. The nature of the spacer between the CD-ring and the primary amines of each monomer is found to influence both molecular weight and polydispersity of the polycations. When these polycations are used to form polyplexes with plasmid DNA, longer alkyl regions between the CD and the charge centers in the polycation backbone increase transfection efficiency and toxicity in BHK-21 cells, while increasing the hydrophilicity of the spacer (alkoxy versus alkyl) provides for lower toxicity. Further, γ-CD-based polycations are shown to be less toxic than otherwise identical β-CD-based polycations.

Linear, cyclodextrin-based gene delivery systems, such as those described in the first part of this thesis, are amenable to forming polyplexes with a wide range of physicochemical properties that include size, surface charge, and density and type of ligand presented. However, it is not known how to best design these particles without having a set of physicochemical design constraints that have been optimized for the intended gene-delivery application. In the second part of this thesis, I developed a model delivery system that can mimic the surface properties of the cyclodextrin-based gene-delivery particles and used it to define design constraints that should be applied to next generation gene delivery particles. As a test case, a well-defined nanoparticle-based system is developed to guide the rational design of gene delivery to hepatocytes in the liver. The synthetic scheme allows for the variation of mean particle size and particle size distribution through variation in reaction conditions. The nanoparticle synthesis is also amenable to incorporation of various ligand types, e.g., galactose, at tunable densities. The synthesized nanoparticles are further shown to have PEGylated surfaces that resist aggregation in serum. Finally, the availability of galactose to receptor binding is demonstrated by agglutination with RCA_{120}.

Four nanoparticles are synthesized specifically for the purpose of identifying design constraints to guide next generation gene delivery to the liver. These nanoparticles are synthesized and described: Gal-50 and Gal-140 are galactosylated 50 nm and 140 nm nanoparticles, while MeO-50 and MeO-140 are methoxy-terminated 50 nm and 140 nm nanoparticles. All four particles have the same surface charge, and Gal-50 and Gal-140 have the same surface galactose density.

The hepatocyte uptake *in vitro* and hepatic distribution *in vivo* of these four nanoparticles is investigated. In freshly isolated hepatocytes, Gal-50 nanoparticles are taken up to a greater extent than are MeO-50, but both 50 nm beads are taken up to a much greater extent than are either of the 140 nm nanoparticles. However, about 90% of the *in vivo* dose of Gal-140 nanoparticles is found within the liver 20 minutes after tail-vein injection. TEM and immunohistochemistry images confirm that Gal-140 nanoparticles are primarily internalized by Kupffer cells, though isolated examples of a few Gal-140 in hepatocytes can also be found. On the other hand, Gal-50 nanoparticles are overwhelmingly found in vesicles throughout the cytoplasm of hepatocytes, with only isolated examples of Kupffer cell uptake. Despite similar surface charge and ligand density, 50 nm nanoparticles are primarily found in hepatocytes while 140 nm nanoparticles are primarily seen in Kupffer cells. It is therefore clear that slightly anionic, galactose-PEGylated nanoparticles should be about 50 nm in diameter to preferentially target hepatocytes while they should be about 140 nm in diameter to selectively target Kupffer cells.

Table of Contents

List of Figures

List of Schemes

List of Tables

CHAPTER ONE

INTRODUCTION AND ORGANIZATION OF THESIS PRESENTATION

Gene therapy involves the manipulation of cellular gene expression in such a way that it will be corrective to the patient but not inherited to the next generation. Gene therapy promises to revolutionize the clinical treatment of countless genetic disorders in decades to come, but human gene therapy today is still in its infancy. For clinical gene therapy to become commonplace, improvements must be made in the design of gene delivery vectors to improve gene expression efficiency, as well as in the overall physicochemical properties of the gene delivery particles to improve target selectivity. This thesis addresses issues aimed at improving the prospects of gene therapy.

This thesis is composed of two separate parts. In the first part, synthetic variations of linear, cyclodextrin-based polycations are used to probe structure-gene delivery properties. The synthesis and characterization of new cyclodextrin-polycations are described, followed by the results of *in vitro* assays that allow for the elucidation of structure-function relationships. In particular, the impact of cyclodextrin-type and nature of the spacer between the cyclodextrin and the charge center on toxicity and transfection efficiency in BHK-21 cells is investigated. A discussion follows that ties together the results and relates this work to other structure-function studies performed in our group.

Chapter Three through Chapter Six represent Part Two of this thesis. Part Two discusses the development, characterization and results of uptake experiments of a nanoparticle-based model system that approximates the physicochemical properties of linear, cyclodextrin-based polycations such as those discussed in Part One.

Chapter Three provides an introduction to gene delivery to the liver. First an overview of liver structure and physiology is presented, along with a number of images to clarify the discussion. A number of liver diseases are then discussed as candidates for treatment by gene therapy, and the potential advantages of gene therapy over conventional treatment are outlined. Specifically targeting non-viral gene delivery polyplexes to the desired liver cells to treat these diseases has proved difficult, and the importance of developing a nanoparticle-based model system that mimics the surface properties of our cyclodextrin-based polyplexes is discussed. Other requirements of the model system are also presented.

Chapter Four begins with a brief discussion of the importance of PEGylating nanoparticle-based systems for *in vivo* applications and then details the synthesis and characterization of the nanoparticles mentioned in Chapter Three. FITC-embedded carboxy-polystyrene nanoparticles were reacted with PEG to form protective coronas that shielded any hydrophobic surfaces from contact with other nanoparticles or massive protein adsorption from serum. By careful control of reaction conditions, the mean nanoparticle diameter as well as the particle size distribution could be varied and matched to the actual size distribution of polyplexes. Galactose can be conjugated to the nanoparticles at different surface densities, and the accessibility of the galactose moieties to lectin binding is demonstrated. Four nanoparticles are described that will be carried forward for *in vitro* and *in vivo* uptake experiments, which are presented in Chapter Five.

Chapter Five begins by discussing why freshly isolated hepatocytes were used for *in vitro* experiments instead of commonly used hepatocarcinoma cell lines. A discussion of *in vitro* results follows, in which plated hepatocytes and suspended hepatocytes are both utilized. A set of experimental conditions is then identified that maximizes hepatic uptake following injection of nanoparticles. The effects of dose and time gap between injection and liver removal are studied and results are presented. Once experimental conditions are set, the overall uptake of each of the four nanoparticles into hepatic tissue is studied and results are discussed. TEM analysis of liver cross-sections provides information on hepatic distribution and intracellular trafficking of the nanoparticles, and a number of representative images are presented. Finally, an immunohistochemical staining procedure is developed and introduced by way of illustration on an actual TEM image. Results of these three-color images are discussed and overall conclusions are drawn.

CHAPTER TWO

STRUCTURAL EFFECTS OF CARBOHYDRATE-CONTAINING POLYCATIONS ON GENE DELIVERY. 3. CYCLODEXTRIN TYPE AND FUNCTIONALIZATION

Reproduced with permission from [S. R. Popielarski, S. Mishra and M. E. Davis,

Bioconjugate Chemistry, **2003**, *14*, 672-678]

2.1 Introduction

Numerous non-viral gene delivery studies are involved in elucidating the relationships between vector structure and transfection efficiency by modifying promising systems and assaying their performance. This ongoing research has demonstrated the significant influence of polycation structure on the efficiency of gene delivery. Poly(ethyleneimine)s (PEIs) are a widely-studied class of polycations for gene delivery. PEI molecular weight has been shown to affect both cytotoxicity and transfection efficiency (1, 2). The charge density (1) and degree of branching (3) in the PEI backbone also significantly alter transfection efficiency *in vitro*. Furthermore, substituents grafted onto PEI affect the interaction of PEI with DNA as well as PEI/DNA polyplex interactions with cells (4-6, and references therein). Ionenes are another class of gene delivery vehicles whose structure has been related to stability of interaction with DNA (7) and to transfection efficiency (8). Structure-function studies have also been undertaken with systems based on chitosan (9), poly(L-lysine) (10), linear poly(amidoamine)s (11), polysaccharide-oligoamine conjugates (12) and others. It is clear from these reports that minor changes in the structure of the gene delivery vehicle can have dramatic effects on the gene delivery efficiency and toxicity of the vector.

We have prepared families of linear, β-cyclodextrin-containing polycations (βCDPs) and have shown that these polymers can be used as gene delivery vectors (13, 14). Cyclodextrins (CDs) are cup-shaped molecules formed of cyclic oligomers of glucose. Cyclodextrins comprised of 6, 7 and 8 glucopyranose units are called α-, β- and γ-CD, respectively (β-CD is represented in Figure 2.1). There are three distinct hydroxyls per glucopyranose unit; two secondary carbons and one primary carbon bear these hydroxyls and they are labeled C(2), C(3) and C(6), respectively (Figure 2.1). The glucopyranose units are denoted alphabetically starting with 'A' and proceeding around the cyclodextrin ring (Figure 2.1).

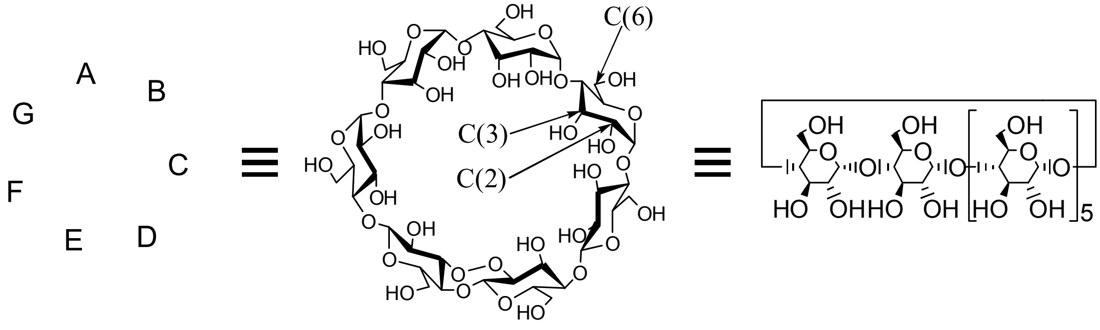

Figure 2.1. Representations and labeling of β-cyclodextrin.

Initial structure-function studies with βCDPs demonstrated the importance of inter-charge spacing to transfection efficiency and toxicity (14). Significant effects on transfection efficiency were observed when the inter-amidine distance was reduced by just 2Å. Based upon this finding, we initiated a more complete structure-function investigation using linear, cyclodextrin-containing polycations. In part 1 of our study, we showed that cellular toxicity was related to the distance of the charge center from the carbohydrate unit (whether it be a cyclodextrin or trehalose), and that increasing polycation hydrophilicity provides decreasing toxicity (15). Part 2 of our work revealed that the type of charge center can dramatically change the delivery efficiency (16). With the βCDPs, amidine charge centers give greater gene delivery than quaternary ammonium charge centers. Here, we vary the type of cyclodextrin (β and γ) and the functionalization at the cyclodextrin, i.e., $3^A,3^B$-dideoxy-$3^A,3^B$-diamino-β- and γ-CD, as compared to the previously used $6^A,6^D$-dideoxy-$6^A,6^D$-diamino-β-CD, to prepare a distinct series of linear, cyclodextrin-containing polycations. Additionally, we report the effects of spacer length between the cyclodextrin and the charge center in order to make direct comparisons between otherwise identical β- and γ-CD-based polyamidines. The polycations were characterized and assayed for plasmid DNA (pDNA) binding, polyplex size and ζ-potential, and *in vitro* transfection efficiency and toxicity.

2.2 Materials and Methods

β- and γ-cyclodextrins were purchased from Wacker Biochem Corp. (Adrian, MI) and dried *in vacuo* at 120°C overnight before use. Chlorosulfonic acid (Alfa Aesar; Ward Hill, MA) was distilled before use. Dimethyl suberimidate•2HCl (DMS) was purchased from Pierce Endogen (Rockford, IL) and used without further purification. All other reagents were obtained from commercial suppliers and were used as received. Ion-exchange chromatography was run on a Toyopearl SP-650M (TosoHaas; Montgomeryville, PA) column (NH_4^+ form) and products were eluted with aqueous ammonium bicarbonate up to 0.4M. Thin-layer chromatography was performed on Silica Gel 60 F 254 plates (EM Separations Technology; Gibbstown, NJ) and the amino-compounds were eluted with 5:3:3:1 *n*-PrOH:AcOEt:H_2O:NH_3(aq) and visualized by reaction with ninhydrin. Matrix-assisted, laser desorption/ionization time-of-flight mass spectroscopy (MALDI-TOF-MS) was performed on a PerSeptive Biosystems Voyager DE PRO BioSpectrometry Workstation in the positive ion mode using a 2,5-dihydroxy benzoic acid matrix. NMR spectra were recorded on a Bruker AMX500 spectrometer as dilute solutions of either D_2O or DMSO-*d*$_6$. Dialysis was carried out using a 3500 molecular weight cutoff regenerated cellulose dialysis cassette (Pierce Endogen).

2.2.1 Synthesis of Benzophenone-3,3'-disulfonyl Chloride (1, Scheme 2.1)

26.06 g (0.143 mol) of benzophenone were added in small portions to 190 mL (2.86 mol) of freshly distilled chlorosulfonic acid under an argon atmosphere. The solution was then heated to 120°C with reflux. After 20 hours at 120°C, the cooled solution was added slowly to about 1000 g of ice in a 2L Erlenmeyer flask. The slurry was poured into a separatory funnel then extracted with chloroform (350 mL then 300 mL) and washed with saturated $NaHCO_3$ (200 ml), water (200 mL) and saturated NaCl (200 mL, twice). The chloroform was removed under reduced pressure. The yellow solid obtained was recrystallized twice from chloroform/hexanes. The first-crop yielded 30 g of off-white crystals; thesecond-crop yielded 5.4 g. (65% yield). Anal. (C_{13}-$H_8Cl_2O_5S_2$) C, H, Cl, S.

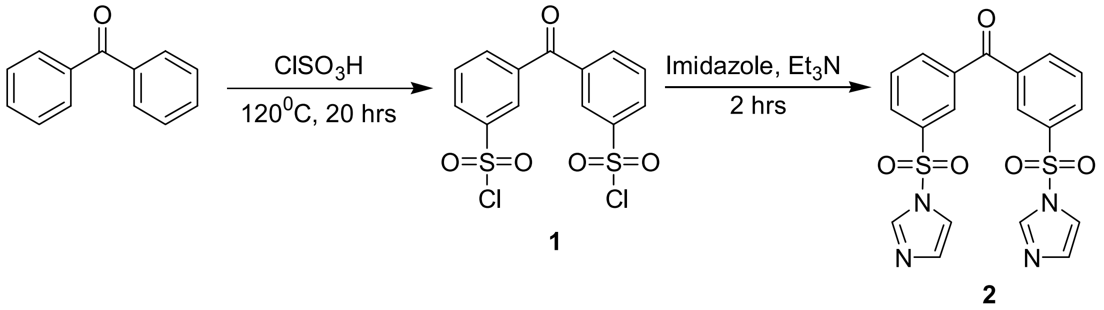

Scheme 2.1. Synthesis of Benzophenone-3,3'-disulfonyl Imidazole (**2**)

2.2.2 Synthesis of Benzophenone-3,3’-disulfonyl Imidazole (2, Scheme 2.1)

13 g (34.3 mmol) of **1** were dissolved in 150 mL chloroform. Imidazole (4.95g, 72.7 mmol) and Et_3N (10.2 ml, 73.2 mmol) were added. After about 30 minutes of stirring, 50 mL of dichloromethane were added to the slurry and allowed to stir for an additional 30 minutes. About 200 mL of dichloromethane were required to homogenize the reaction slurry, which was then washed with water (200 mL, twice) and dried with sodium sulfate. Benzophenone-3,3’-disulfonyl-imidazole, **2**, was recrystallized from dichloromethane/ethyl acetate giving 13.9 g of colorless needles (92% yield). Anal. (C_{19}-$H_{14}N_4O_5S_2$) C, H, N, S. NMR data were in agreement with published chemical shifts (17).

2.2.3 Synthesis of cyclodextrin-polycations (6a-d and 7a-d, Scheme 2.2).

Syntheses of $2^A,2^B$-disulfonated β-cyclodextrin (17) (**3a**) and $2^A,2^B$-disulfonated γ-cyclodextrin (18) (**3b**) were carried out according to literature methods. NMR and mass spectra data were in agreement with published values (17, 18). Syntheses of $3^A,3^B$-di(aminoalkylamino)-β- and $3^A,3^B$-di(aminoalkoxyamino)-γ-cyclodextrins (**4a-d** and **5a-d)** were carried out as exemplified by the following procedure.

Synthesis of 5c

Hexamethylenediamine (5.89 g, 50.7 mmol) was dissolved in 35 mL degassed water. **3b** (1.50 g, 0.88 mmol) was added at once and stirred at 37^{O}C under nitrogen for

19 hours. The reaction was further carried out at 70^{O}C for 3 hours then concentrated under reduced pressure. Cyclodextrins were precipitated with 11:1 acetone:methanol and collected by filtration. Ion-exchange chromatography yielded the pure product (855 mg, 54% yield). MALDI-TOF-MS $[M+H]^+$ = 1493.7.

The polycations were prepared as exemplified by the following procedure.

Synthesis of 7c

5c (100mg, 54.7 μmol) and DMS (15.5 mg, 56.7 μmol) were taken up in 108 μL 0.5M Na_2CO_3 and stirred for 13 hours. Acidification with 1N HCl to pH 2.0 followed by exhaustive dialysis yielded 58.4 mg of a white powder (56% yield).

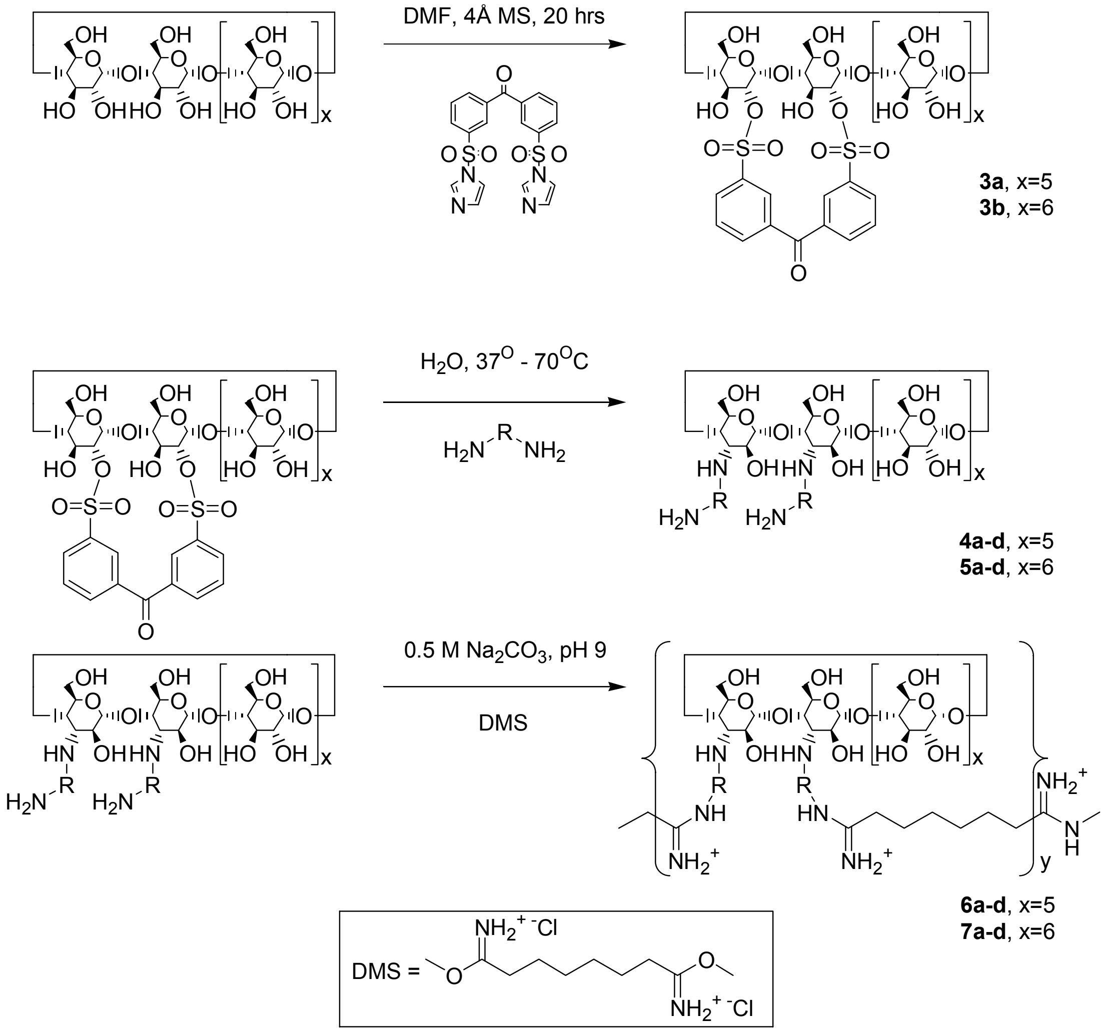

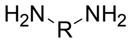	diamino-β-CD	diamino-γ-CD	β-CD-polycation	γ-CD-polycation
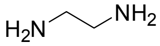	**4a**	**5a**	**6a**	**7a**
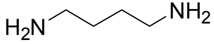	**4b**	**5b**	**6b**	**7b**
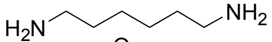	**4c**	**5c**	**6c**	**7c**
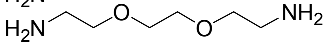	**4d**	**5d**	**6d**	**7d**

Scheme 2.2. Synthesis of Cyclodextrin-polycations (6a-d and 7a-d).

2.2.4 Light Scattering and Molecular Weight Determination

The specific refractive index (RI) increment, d*n*/d*c*, of each polycation was determined by fitting a linear curve to plots of RI versus concentration (five data points per polycation). Polycations were then analyzed on a Hitachi D6000 HPLC system equipped with an ERC-7512 RI detector and a Precision Detectors PD2020/DLS light scattering detector using a PL aquagel-OH column (Polymer Laboratories, Amherst, MA). The eluent was 0.8 M ammonium acetate with 0.05% sodium azide, adjusted to pH 2.8 with phosphoric acid and flowing at 0.7 mL/min. RI values were measured on a Carl Zeiss refractometer (Max Erb Instrument Co., Burbank, CA) in the same eluent as used for HPLC analysis.

2.2.5 Plasmid DNA

Plasmid pGL3-CV (Promega; Madison, WI) was amplified with the DH5α strain of E. coli (Gibco BRL; Gaithersburg, MD) and purified using the Ultramobius 1000 kit (Novagen; Madison, WI). This plasmid encodes the firefly luciferase gene under control of the SV40 promoter.

2.2.6 Polyplex Formation and Characterization

Polyplexes were formulated by adding polycation solutions in dH_2O to an equal volume of plasmid DNA (pDNA) in dH_2O (0.05 mg/mL final pDNA concentration) and incubating for 30 minutes. Desired charge ratios were achieved by using appropriate concentrations of polycation solution. Each polycation was examined for its ability to bind pDNA through a gel electrophoresis assay using a 0.8% agarose gel (30 μg ethidium bromide/50 mL TAE buffer). Particle size and ζ-potential of polyplexes were analyzed using a ZetaPALS instrument (Brookhaven Instruments; Holtsville, NY).

2.2.7 Cell Culture and Transfections

BHK-21 cells were maintained at 37°C in 5% CO_2 atmosphere in Dulbecco's Modified Eagle's Medium supplemented with 10% fetal bovine serum, 100 U/mL penicillin, 0.1 mg/mL streptomycin and 0.25 μg/mL amphotericin B (Gibco BRL). For transfections, cells were seeded at 50,000 cells/well in 24-well plates. Trypan blue exclusion was used to verify cell viability above 95%. At one day, cells were exposed to 200 μL serum-free medium containing 1 μg pGL3-CV plasmid pre-assembled with CD-containing polycations at various charge ratios. After four hours, polyplex solutions were removed from the cells and replaced with 1 mL regular growth medium. For measurement of luciferase activity and toxicity, cells were lysed two days after transfection with 1X Cell Culture Lysis Reagent (Promega). The Luciferase Assay System (Promega) was used to measure luciferase activity of cell lysates on a Monolight 2010 luminometer (Becton Dickinson Biosciences; San Jose, CA). Total protein content of cell lysates was assessed with the DC Protein Assay (Bio-Rad; Hercules, CA) that is a derivative of the Lowry assay.

Supporting Information Available: MALDI-TOF spectra of CD-monomers **4a-d** and **5a-d**. This material is available free of charge via the Internet at http://pubs.acs.org.

2.3 Results

2.3.1 Polycation Synthesis and Characterization

β- and γ-CDs were selectively di-functionalized through a stapling reaction with benzophenone-3,3'-disulfonyl-imidazole (Scheme 2.1). These intermediates react with various alkyl- and alkoxy-diamines to yield $3^A,3^B$-di(aminoalkylamino)-CDs with various spacing groups between the carbohydrate ring and the primary amine (Scheme 2.2). The difunctionalized amino-CD monomers were polymerized with DMS to give polycations with properties shown in Table 2.1.

Polycation	Polymerization Yield (%)	d*n*/d*c* (mL/g)	M_w (kDa)	M_w/M_n	Average degree of polymerization
6a	32	0.1029	10.0	1.1	6
6b	44	0.1406	8.1	1.3	5
6c	61	0.1515	13.9	1.7	8
6d	74	0.1322	13.0	1.4	7
7a	32	0.1085	9.3	1.1	5
7b	47	0.1386	9.6	1.4	5
7c	56	0.1237	14.7	1.6	8
7d	58	0.1279	13.3	1.3	7

Table 2.1. Effect of cyclodextrin comonomer structure on polymerization.

The choice of CD-comonomer influences the polymerization with DMS; polymerization yield increases with increasing distance between the cyclodextrin-ring and the primary amine on the CD-monomer. Similar yield trends were observed for otherwise identical β- and γ-CD polycation syntheses. CD-monomers with fewer than four methylenes between the cyclodextrin and the primary amine yielded polycations with an average degree of polymerization (DOP) of 5 or 6, while those synthesized from monomers with over four spacer methylenes produced an average DOP of 7 or 8. An increase in polydispersity accompanied the increase in polycation length.

2.3.2 Polyplex Formation and Characterization

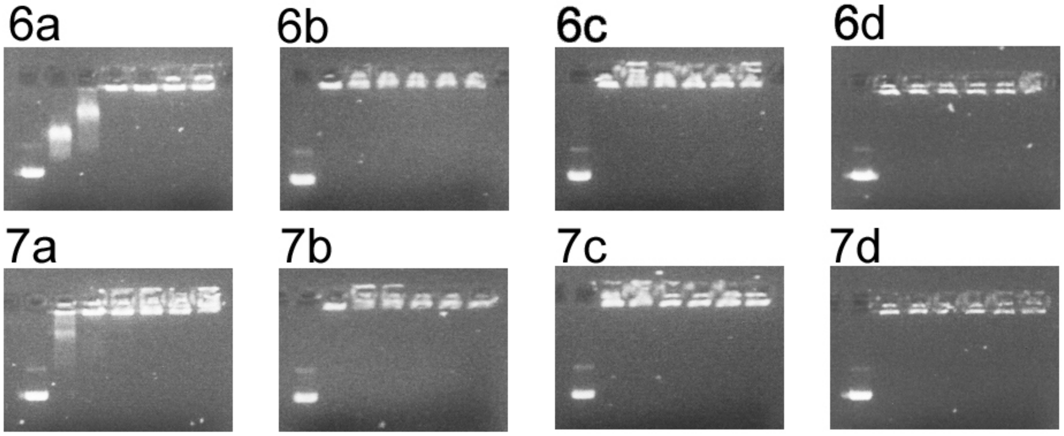

Figure 2.2. Agarose gel electrophoresis of polycation/pDNA complexes. For each polycation, complexes were formulated at charge ratios (+/-) of 0, 0.5, 1.0, 1.5, 2.0, 2.5, and 3.0 and run in order of increasing charge ratio (left to right) on a 0.8% agarose gel.

To demonstrate polycation interaction with pDNA, polyplexes were formulated and run on a 0.8% agarose gel at a range of charge ratios. Polycations **6a** and **7a** did not completely retard DNA below a charge ratio of 1.5, while **6b-d** and **7b-d** retarded DNA at charge ratios of 0.5 and above (Figure 2.2). The diameter of polycation/pDNA polyplexes varied between 100 and 150 nm, while the associated ζ-potentials were all found to be positive (Table 2.2).

Polycation	Particle diameter (nm)	Zeta potential (mV)
6a	121.5 ± 1.3	12.5 ± 0.3
6b	96.4 ± 1.1	6.4 ± 1.1
6c	107.7 ± 0.9	16.7 ± 1.7
6d	88.2 ± 6.9	27.7 ± 1.0
7a	124.1 ± 1.6	23.3 ± 0.5
7b	118.6 ± 23.9	17.5 ± 3.0
7c	153.3 ± 1.7	9.6 ± 1.1
7d	102.9 ± 1.0	30.7 ± 1.4

Table 2.2. Particle sizing and zeta-potential of polycation/pDNA complexes formulated at charge ratio (+/-) of 5.

2.3.3 *In Vitro* Transfection Efficiency

In vitro transfection efficiency to BHK-21 cells was assessed in triplicate at charge ratios (+/-) of 2, 4, 6, 8, 10, 15 and 20. Lysates of transfected cells were assessed for luciferase activity by measuring the relative light units (RLU) normalized by total protein content (Figure 2.3).

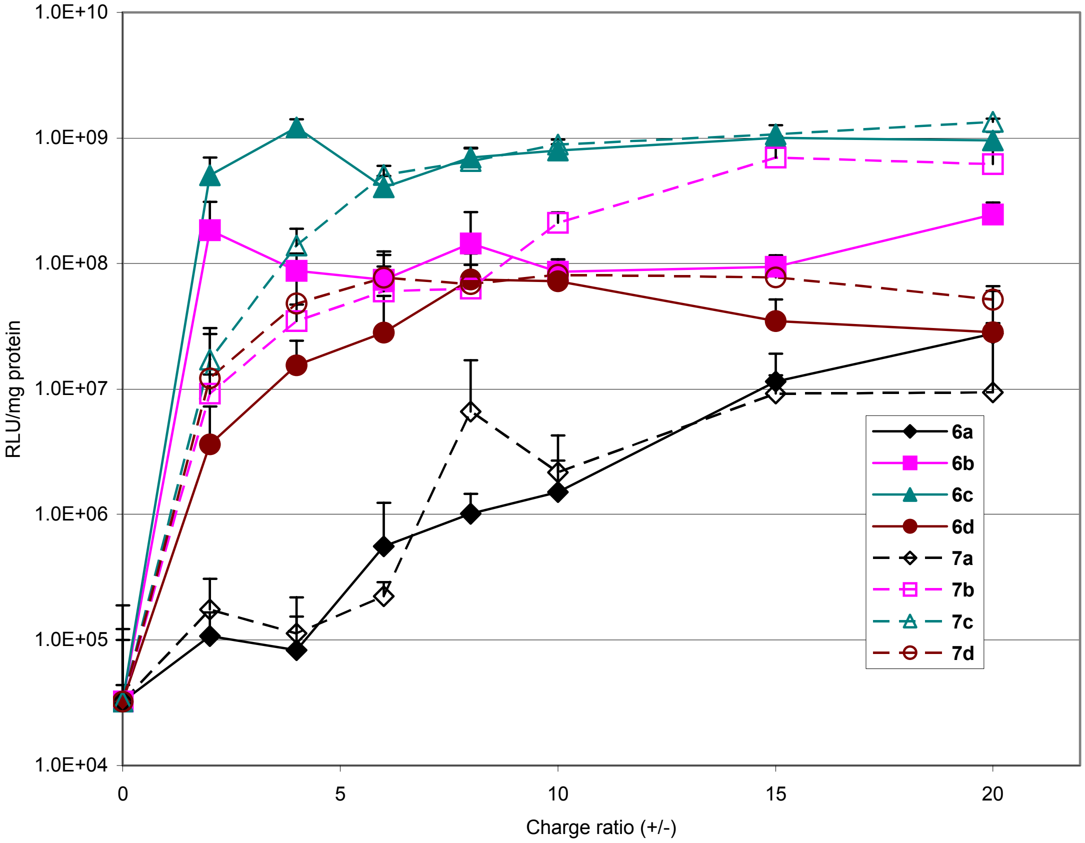

Figure 2.3. Relative light units (RLU)/mg protein as a function of charge ratio for cyclodextin-polycation/pDNA complexes. Complexes were formulated at various charge ratios and exposed to BHK cells in serum-free medium for four hours. 48 hours after exposure, the cells were assayed for luciferase activity. Charge ratio of 0 indicates naked pDNA.

Among the diaminoalkyl-CD analogues, **6a-c** and **7a-c**, increased spacer length produced greater transfection efficiency, with more pronounced enhancements between the **a** and **b** variants in each series. The diaminoalkoxy-CD analogues, **6d** and **7d**, demonstrated intermediate levels of luciferase expression, below that achieved with the **b** analogues. Generally speaking, the β-CD and γ-CD polycations with identical spacers produced similar luciferase gene expression.

2.3.4 *In Vitro* Cellular Toxicity

The total protein content of cell lysates was used as a measure of polyplex and/or polycation toxicity (Figures 2.4 and 2.5).

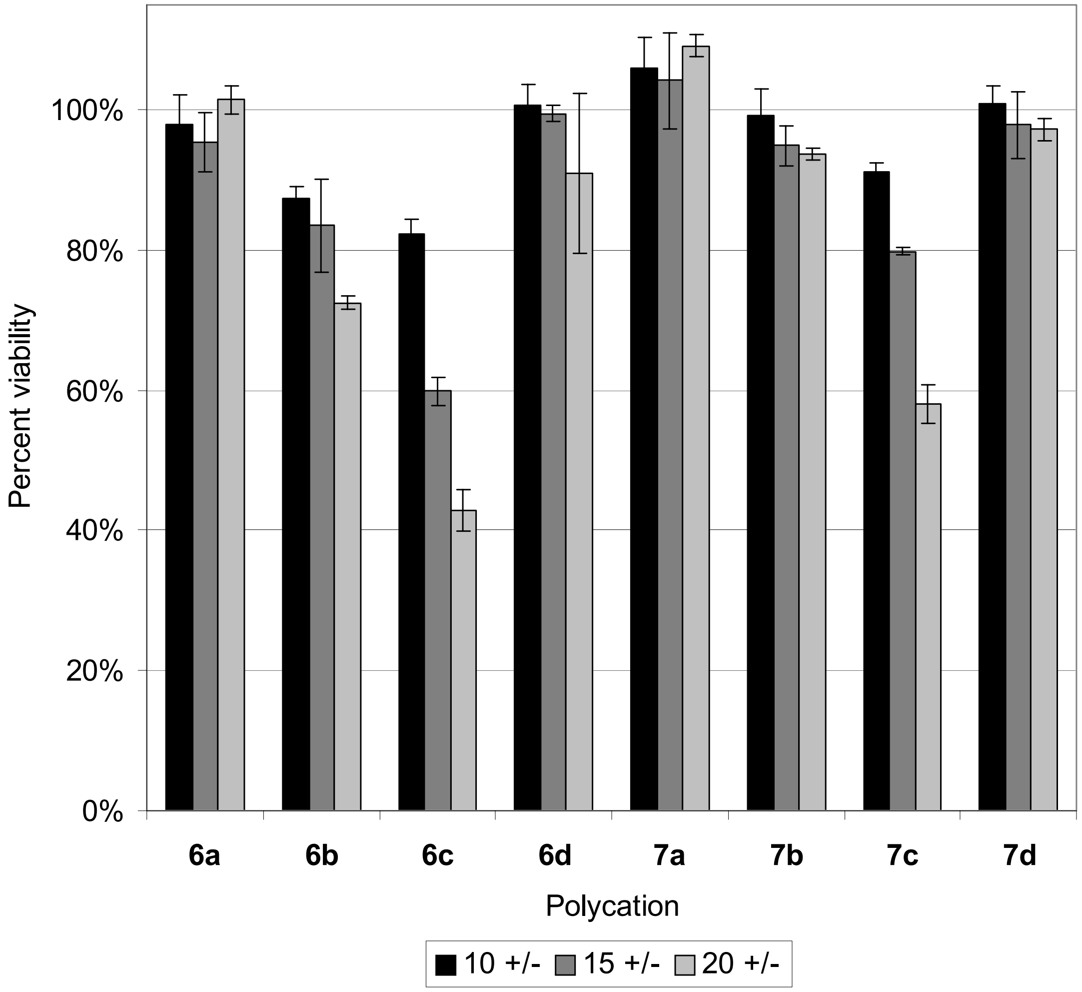

Figure 2.4. Cell viability to exposure of polycation/pDNA complexes at various charge ratios. Cells were assayed for viability 48 hours after exposure to complexes; data were normalized with respect to untreated cells.

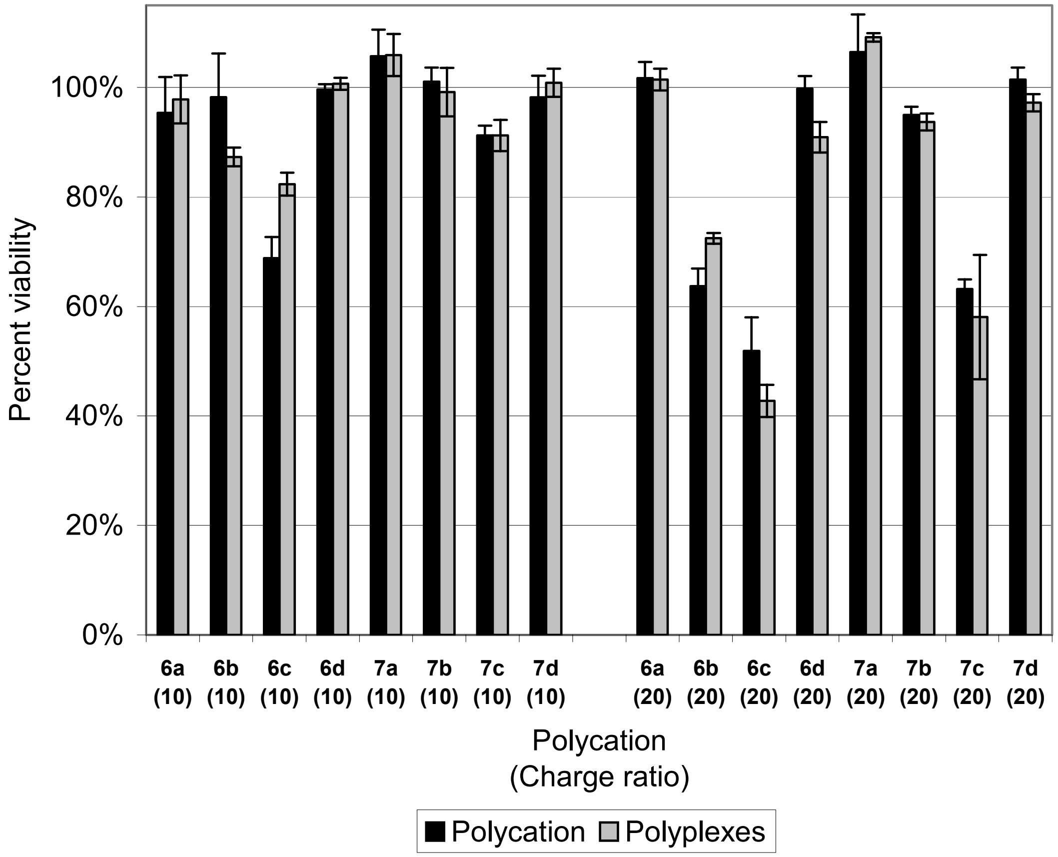

Figure 2.5. Comparison of the toxicity of polycation alone to polycation/pDNA complexes. Cells were exposed to polycation alone or to an equal amount of polycation complexed with pDNA; "charge ratio" for polycation alone merely represents amount of polycation. Total protein concentrations in cell lysates were used as a measure of viability; data were normalized using values for untreated cells.

The fractional cell survival of transfected cells was assessed by comparison to untransfected cells. Amongst the charge ratios investigated, polycations **6a-c** and **7a-c** demonstrated a marked decrease in cell viability with increased spacer length; **6d** and **7d** were essentially non-toxic at the concentrations employed. For the **b** and **c** analogues, cell viability decreased with increasing charge ratio and was worse for the β-CD polycations than for the γ-CD polycations. The toxicity of each polycation was independent of the presence of pDNA, as determined by comparison of polyplex-transfected cells with those exposed to an equal amount of polycation alone (Figure 2.5).

2.4 Discussion

Previous studies of β-cyclodextrin-containing polycations (βCDPs) have demonstrated the importance of polycation structure to cellular toxicity and *in vitro* transfection efficiency. The effect of inter-amidine distance (14) has been elucidated, as has the importance of using a bulky cyclodextrin instead of a smaller carbohydrate such as trehalose (15). Here, we investigated the relevance of cyclodextrin ring size by studying otherwise identical series of β- and γ-cyclodextrin polycations. Within each series, the length and character of the spacer between the cyclodextrin ring and the amidine charge center were varied to understand the importance of these additional variables in our system. Such an approach allows the direct evaluation of the effect of cyclodextrin-type on *in vitro* transfection efficiency and cellular toxicity as well as providing further insights into the role of charge spacing along the polycationic backbone. For *in vivo* application of the polycations described in this report, modifications are required to impart salt and serum stability. Methodologies for modifying similar cyclodextrin-based polycations for *in vivo* use are available in our earlier publication (20).

The β- and γ-CD-based series of polycations follow remarkably similar trends in DOP. DOP is found to increase with distance between the reactive primary amines of the CD-monomers and the cyclodextrins themselves. As the number of methylenes between the cyclodextrin and primary amine increases, an increase in DOP is observed with an accompanying increase in polydispersity. All polycations shown here have an average DOP between 5 and 8, corresponding to an average of 10 – 16 amidine charge centers per polycation chain. Assuming these differences in DOP do not significantly affect polycation performance, a direct correlation may be made between polycation structure and the observed performance.

Previous work demonstrated that the transfection efficiency and toxicity achieved with CD-containing polycations are affected by the presence of cyclodextrins and by the alkyl chain length between charge centers (14, 15). Here, it is demonstrated that the transfection efficiency and toxicity of a related set of polycations are affected by the structure of the spacer separating the CD ring from the charge centers and, to a lesser degree, the type of CD used.

Diaminoalkyl-CD polycations **6a-c** and **7a-c** exhibit a marked increase in transfection efficiency as the spacer length increases, particularly with the increase from 2 to 4 methylene units. Dramatic differences between the **a** and **b** analogues are observed despite only a small change in polycation structure (a 2Å increase in distance between the cyclodextrin and the amidine charge center). A smaller but significant increase in transfection efficiency is observed between the **b** and **c** analogues. Polycations **6a** and **7a** gave low levels of luciferase expression that gradually increased with increasing charge ratio. Optimum expression levels observed with these two polycations were of the same order as transfection efficiencies seen with polycations **6b**, **6c**, **7b** and **7c** at the lowest charge ratios. Having reached relatively high transfection efficiencies at the lowest investigated charge ratios, polycations **6b**, **6c**, **7b** and **7c** did not display the steady and marked increase with charge ratio seen with **6a** and **7a**. Beyond a charge ratio of 6+/-, only **7b** demonstrated a significant increase in luciferase expression.

The least effective polycations, **6a** and **7a**, are also observed to require the highest charge ratio to completely retard pDNA in the electrophoresis assay. Previous work with CD-containing polycations has shown a correlation between relative binding efficiency and transfection efficiency (15). The reduced binding efficiency associated with decreased spacer length may result from the bulky cyclodextrins impeding the access of polycation amidines to pDNA phosphates.

The presence of CDs in the polycation backbone has been shown to produce a dramatic reduction in toxicity of β-CD-containing polycations (13-16). In part 1 of our study (15), $6^A,6^D$-dideoxy-$6^A,6^D$-diamino-β-CDs were studied, while $3^A,3^B$-dideoxy-$3^A,3^B$-diamino-β- and γ-CDs are investigated here. The transfection and toxicity assays employed in this series of papers do not indicate any advantages of functionalization of the CD at the C(3)-position over functionalization at the C(6)-position. In part 1 it was shown that longer spacer lengths between the CD and the charge center result in increased toxicity; that is in agreement with the result that polycations **6a-c** and **7a-c** demonstrate an increase in toxicity as the CD-amidine distance is increased. These results suggest that there is a toxicity-mediating influence of the CD on the cationic center, regardless of the site of CD-derivatization. The CD may be affecting the interaction of the amidine charge centers with intracellular entities through its steric bulk and/or large sphere of hydration and thus lowering the toxicity of amidine-containing polycations. The bulkiness of the CD also hinders access of polycation amidines to pDNA phosphates. Since CD bulkiness and/or sphere of hydration correlate with the trends in both toxicity and transfection efficiency, the observation that decreases in toxicity are associated with decreases in transfection efficiency and effective pDNA binding strength is self-consistent.

The diaminoalkoxy-CD polycations **6d** and **7d** demonstrate an intermediate level of transfection efficiency and insignificant toxicity. Although this polycation pair provides the largest spacing between the CD and amidine residues among polycations in this study, the hydrophilic nature of the alkoxy spacer likely enlarges the effective hydration sphere around the cyclodextrin ring. In addition, the alkoxy spacer has more flexibility than alkyl spacers. These factors somehow mitigate the toxicity of polycations **6d** and **7d**. The change in transfection efficiency as a function of charge ratio is also intermediate relative to the diaminoalkyl-CD polycations; RLU/mg protein readings with polycations **6d** and **7d** rose gradually up to a charge ratio of 6+/-, above which no increase is observed.

Each polycation produced measurable luciferase expression above background levels; the luciferase activities of untreated cells and cells treated with polycation alone are roughly $5*10^3$ RLU/mg protein (data not shown) while the luciferase activity of cells treated with pDNA alone is roughly $5*10^4$ RLU/mg protein. For comparison, BHK-21 cells were transfected with complexes of pDNA formulated with 25 kDa branched polyethylenimine or with βCDP6 (14). Polyethylenimine complexes at an N/P of 5 were found to give luciferase activity of $5*10^9$ RLU/mg protein (data not shown). βCDP6 complexes produced $2*10^8$ RLU/mg protein at a charge ratio of 10+/- (data not shown).

Here, analogous β- and γ-CD-containing polycations produced similar levels of gene expression, with the exception that polycations **6b** and **6c** outperform their γ-CD-containing analogues **7b** and **7c** at charge ratios of two and four; however, these differences do not persist as the charge ratio is increased. At higher charge ratios, toxicity differences between the β-CD-containing polycations **6b** and **6c** and the γ-CD-containing analogues become apparent, with the γ-CD-containing polycations being less toxic. It is again interesting to note the correlation between enhanced transfection efficiency and increased toxicity.

The peripheral diameter of γ-CD is about 17.5 Å while that of β-CD is about 15.4 Å (19), highlighting the importance of even small variations in the CD-containing polycation system to *in vitro* performance. Since the polycation backbone goes through adjacent sugar residues of the cyclodextrin ring in the case of the β- and γ-CD polycations discussed in this report, the linear backbone structure varies minimally between the two. However, the remainder of the cyclodextrin-ring, which can be considered pendant to the backbone, is certainly larger in the case of γ- over β-CD.

In part 1, Reineke and Davis showed that trehalose-based polyamidines are more toxic than those based on β-CD. Here, CD-containing polycations demonstrate an increase in toxicity with an increase in distance between the CD and the amidine charge center and with a decrease in the size of the CD-ring. Together, these results are consistent with the hypothesis that the size of the carbohydrate moiety and its associated sphere of hydration (overall increase in hydrophilicity) mitigate the toxicity of the amidine-based polycations.

We have described the synthesis and characterization of a family of cyclodextrin-containing polycations and demonstrated significant and clear effects of polycation structure on *in vitro* gene expression efficiency and cellular toxicity against BHK-21 cells. The structure of diaminated cyclodextrins was found to influence both the molecular weight and polydispersity of polycations resulting from reaction of these compounds with dimethyl suberimidate. Longer alkyl regions in the polycation backbone increased transfection efficiency and toxicity, while increasing hydrophilicity was toxicity-reducing. Further, γ-CD polycations were shown to be less toxic than otherwise identical β-CD polycations.

2.5 Acknowledgements

S.R.P. thanks the Department of Defense for an NDSEG fellowship. We would also like to thank Insert Therapeutics, Inc. for partial support of this project. M.E.D. is a consultant to and has financial interest in Insert Therapeutics, Inc.

2.6 References

1. Jeong, J. H., Song, S. H., Lim, D. W., Lee, H. and Park, T. G. (2001) DNA transfection using linear poly(ethylenimine) prepared by controlled acid hydrolysis of poly(2-ethyl-2-oxazoline). *J. Controlled Release 73*, 391-399.
2. Godbey, W. T., Wu, K. K. and Mikos, A. G. (1999) Size matters: Molecular weight affects the efficiency of poly(ethylenimine) as a gene delivery vehicle. *J. Biomed. Mater. Res. 45,* 268-275.
3. Remy, J.-S., Abdallah, P., Zanta, M. A., Boussif, O., Behr, J.-P. and Demeneix, B. (1998) Gene transfer with lipospermines and polyethylenimines. *Adv. Drug Deliv. Rev. 30*, 85-95.

4. Fischer, D., von Harpe, A., Kunath, K., Petersen, H., Li, Y. and Kissel, T. (2002) Copolymers of ethylene imine and N-(2-hydroxyethyl)-ethylene imine as tools to study effects of polymer structure on physicochemical and biological properties of DNA complexes. *Bioconjugate Chem. 13*, 1124-1133.
5. Petersen, H., Fechner, P. M., Martin, A. L., Kunath, K., Stolnik, S., Roberts, C. J., Fischer, D., Davies, M. C. and Kissel, T. (2002) Polyethylenimine-graft-poly(ethylene glycol) copolymers: Influence of copolymer block structure on DNA complexation and biological activities as gene delivery system. *Bioconjugate Chem. 13*, 845-854.
6. Kircheis, R., Wightman, L. and Wagner E. (2001) Design and gene delivery activity of modified polyethylenimines. *Adv. Drug Deliv. Rev. 53*, 341-358.
7. Zelikin, A. N. and Izumrudov, V. A. (2002) Polyelectrolyte complexes formed by calf thymus DNA and aliphatic ionenes: Unexpected change in stability upon variation of chain length of ionenes of different charge density. *Macromol. Biosci. 2*, 78-81.
8. Zelikin, A. N., Putnam, D., Shastri, P., Langer, R. and Izumrudov, V.A. (2002) Aliphatic ionenes as gene delivery agents: Elucidation of structure-function relationship through modification of charge density and polymer length. *Bioconjugate Chem. 13*, 548-553.
9. Köping-Höggård, M., Tubulekas, I., Guan, H., Edwards, K., Nilsson, M., Vårum, K. M. and Artursson, P. (2001) Chitosan as a nonviral gene delivery system. Structure-property relationships and characteristics compared with polyethylenimine *in vitro* and after lung administration *in vivo*. *Gene Therapy 8*, 1108-1121.

10. Ohsaki, M., Okuda, T., Wada, A., Hirayama, T., Niidome, T. and Aoyagi, H. (2002) In vitro gene transfection using dendritic poly(L-lysine). *Bioconjugate Chem. 13*, 510-517.
11. Jones, N. A., Hill, I. R. C., Stolnik, S., Bignotti, F., Davis, S. S. and Garnett, M. C. (2000) Polymer chemical structure is a key determinant of physicochemical and colloidal properties of polymer-DNA complexes for gene delivery. *BBA – Gene Struct. Expr. 1517*, 1-18.
12. Azzam, T., Eliyahu, H., Shapira, L., Linial, M., Barenholz, Y. and Domb, A. J. (2002) Polysaccharide-oligoamine based conjugates for gene delivery. *J. Med. Chem. 45*, 1817-1824.
13. Gonzalez, H., Hwang, S. J. and Davis, M.E. (1999) New class of polymers for the delivery of macromolecular therapeutics. *Bioconjugate Chem. 10*, 1068-1074.
14. Hwang, S. J., Bellocq, N. C. and Davis, M. E. (2001) Effects of structure of β-cyclodextrin-containing polymers on gene delivery. *Bioconjugate Chem. 12*, 280-290.
15. Reineke, T. M. and Davis, M. E. (2003) Structural effects of carbohydrate-containing polycations on gene delivery. 1. Carbohydrate size and its distance from charge centers. *Bioconjugate Chem. 14*, 247-254.
16. Reineke, T. M. and Davis, M. E. (2003) Structural effects of carbohydrate-containing polycations on gene delivery. 2. Charge center type. *Bioconjugate Chem. 14,* 255-261.
17. Teranishi, K. (2000) Practicable regiospecific bifunctionalization on the secondary face of α- and β-cyclodextrins. *Chem. Commun. 14,* 1255-1256.

18. Teranishi, K., Hisamatsu, M. and Yamada, T. (2000) Regiospecific synthesis of $2^A,2^B$-disulfonated γ-cyclodextrin. *Tetrahedron Lett. 41*, 933-936.
19. Szejtli, J., Ed. (1988) *Cyclodextrin Technology*, Kluwer Academic Publishers, Dordrecht.
20. Pun, S. H. and Davis, M. E. (2002) Development of a nonviral gene delivery vehicle for systemic application. *Bioconjugate Chem. 13*, 630-639.

CHAPTER THREE

INTRODUCTION TO PART TWO

3.1 Introduction

Gene therapy promises to revolutionize the clinical treatment of countless genetic disorders,[1] including many diseases of the liver.[2] Though human gene therapy of liver diseases is still in its infancy, preclinical studies in animal models of disease have demonstrated proof of concept results in nearly all varieties of liver diseases that are conceptually amenable to gene therapy treatment.

3.2 Liver Structure and Physiology

The liver can be thought of as the guardian that resides between the digestive tract and spleen and the rest of the body. In treating blood from the digestive system, the liver is handling large amounts of nutrient amino acids, lipids, vitamins and pollutant xenobiotics that enter the body in food and water. In this capacity, the liver is responsible for metabolically regulating the excess of amino acids and ammonia derived from the intestine and its bacterial flora, glycogen production and storage, and processing of greasy compounds into water-soluble forms for excretion in bile.

In addition to processing ingested materials, the liver has many other responsibilities including synthesizing the majority of the body's total secretory protein, forming bilirubin and bile acids in relation to bile secretion, and removing bacteria, dying platelets and other particulate matter from circulation.

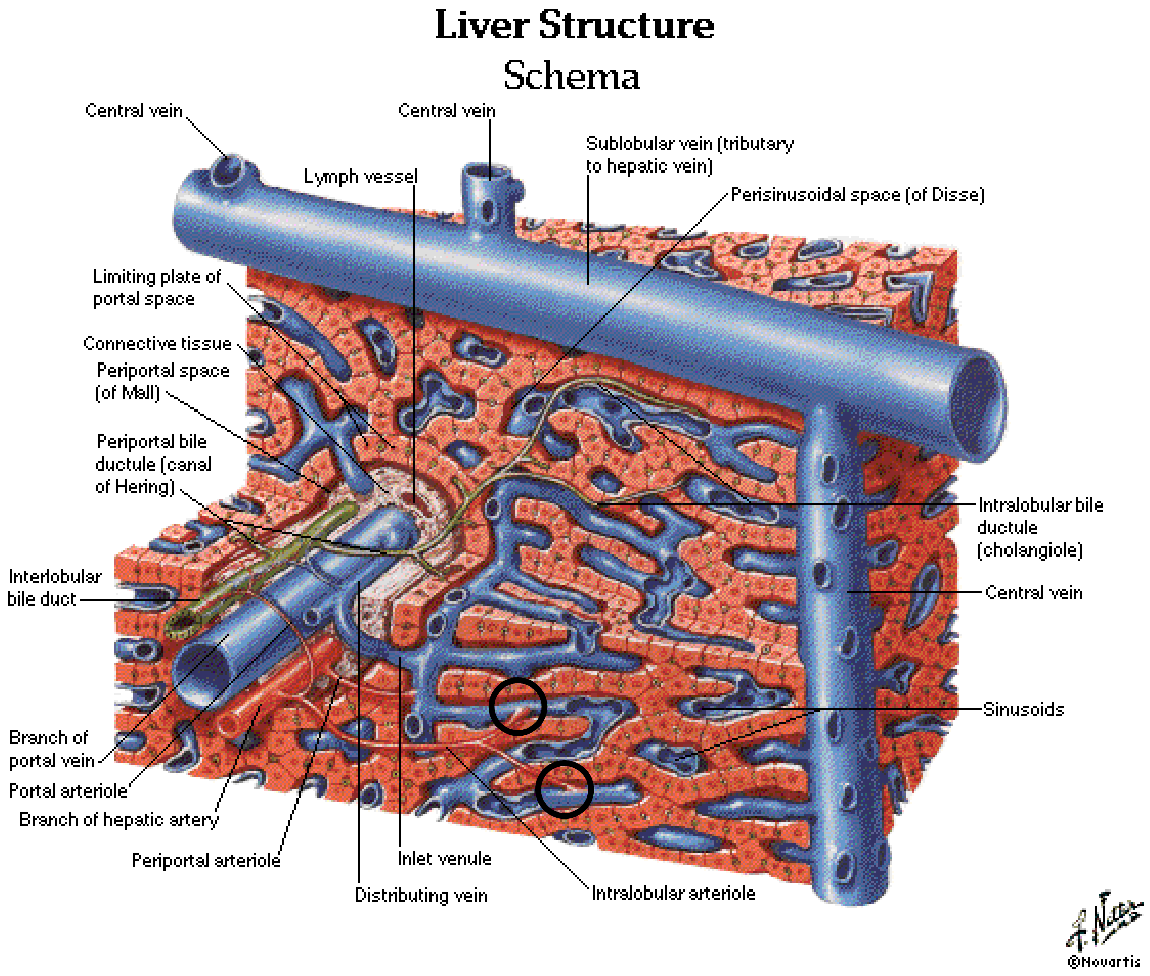

Figure 3.1. Illustration of liver structure. Reproduced with permission from Novartis Pharmaceuticals Corporation. Circles point out mixing of blood flow from the hepatic artery with blood flow from the portal vein.

The portal vein collects all the blood that leaves the spleen, stomach, small and large intestine, gallbladder and pancreas and carries it to the liver. Approximately 75% of the blood flowing into the liver arrives through the portal vein,[3] while the remaining 25% of blood flow arrives via the hepatic artery and provides necessary oxygen for hepatic function. Blood flowing through the portal vein and hepatic artery undergoes about 5 or 6 branches as it snakes through the liver, until finally blood from these two sources is mixed in the sinusoidal bed of the microvasculatory unit (black circles in

Figure 3.1 highlight mixing of blood flow from the two sources). Sinusoids of the liver are specialized capillaries lined with Kupffer cells and endothelial cells that generally drain into central veins that ultimately empty into the inferior vena cava. Single-cell thick sheets and beams of hepatocytes, which are the liver parenchymal cells, are surrounded on each side by sinusoidal channels and are protected by flattened endothelial cells that line the sinusoid and perform barrier functions.

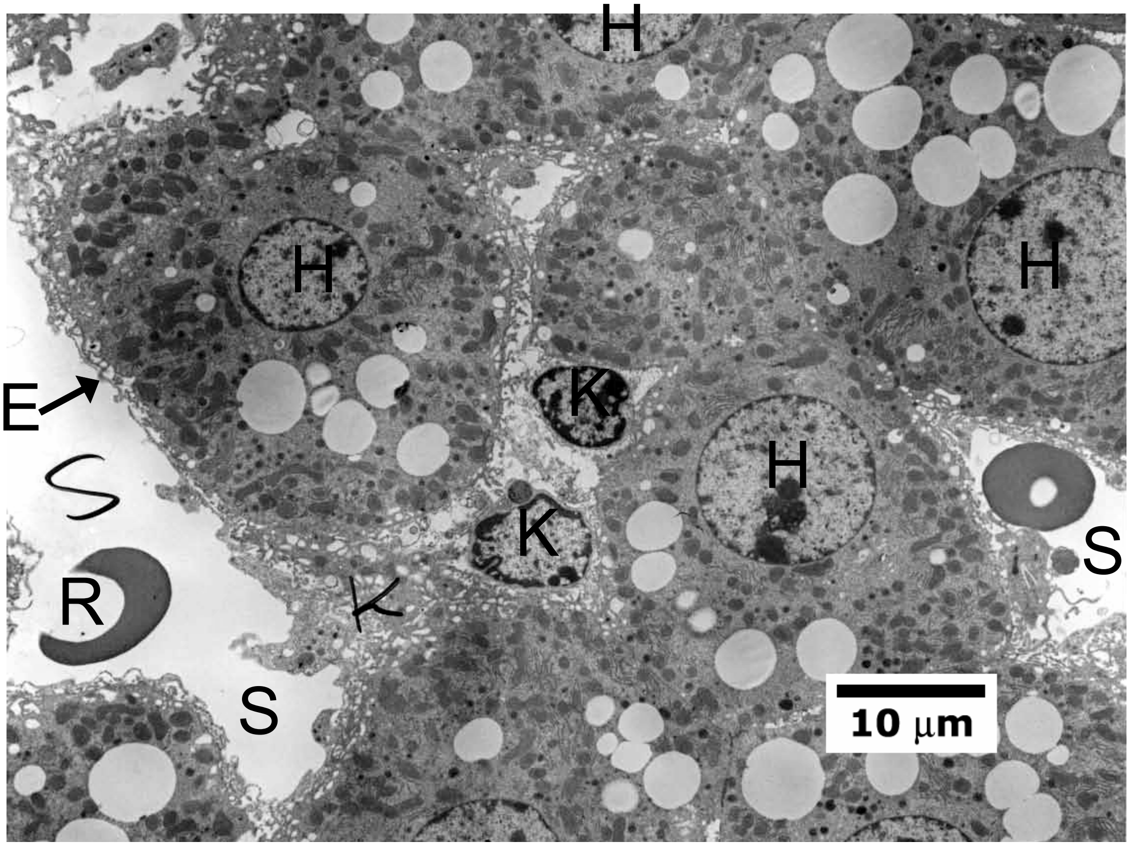

Figure 3.2. TEM image of 20 nm thick section of normal mouse liver. 'H' indicates a hepatocyte nucleus, 'K' indicates a Kupffer cell nucleus, 'R' labels a red blood cell, 'S' labels a sinusoid and 'E' points to an endothelial cell lining the sinusoid.

Kupffer cells ('K' in Figure 3.2) are highly phagocytic members of the reticuloendothelial system that extend directly into sinusoids and monitor blood entering the sinusoid for material that can be phagocytosed or endocytosed. Kupffer cells have receptors for galactose, mannose, insulin and many other ligands.[4] The functions of Kupffer cells include phagocytosis of particulate matter, detoxification of endotoxin, secretion of mediators, mediation of various immune reactions, uptake and catabolism of lipids and glycoproteins including many enzymes, and prolongation of the life of hepatocytes.[5]

Hepatocytes ('H' in Figure 3.2) are polyhedral multifaced cells with eight or more surfaces. In addition to their distinctive shape, hepatocytes are characterized by large regular nuclei, a large number of cytoplamic organelles and a high degree of internal organization. Hepatocytes possess a rich network of endoplasmic reticulum (ER) that is related to the well-developed secretory function of the liver[6] since secretory proteins are synthesized selectively in the rough endoplasmic reticulum.[7, 8] The most intensive synthesis of proteins in the liver occurs in the ER of hepatocytes,[9] since the majority of all blood proteins originate from hepatocytes. In addition to many other metabolic and catabolic functions, hepatocytes are uniquely responsible for regulating the excess of amino acids and ammonia from the intestine with the urea cycle, regulating lipid metabolism related to massive intestinal absorption of lipids and formation of bilirubin and bile acids in relation to bile secretion.

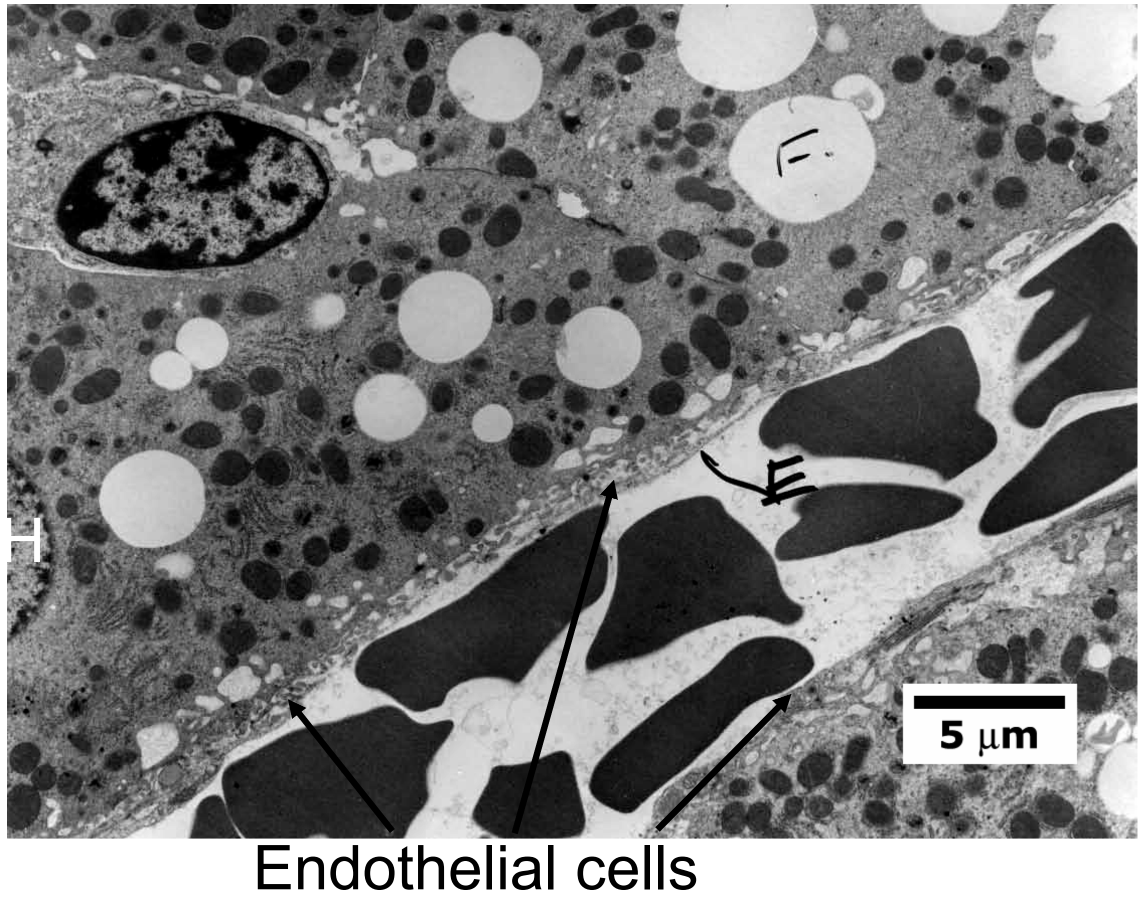

Figure 3.3. TEM image of 20 nm thick section of normal mouse liver, showing liver sinusoidal endothelial cells separating hepatocytes from the blood vessel.

Given the critical regulatory, metabolic and catabolic roles played by hepatocytes, it is not surprising that access to the hepatocyte cell membrane is restricted (Figure 3.3). The barrier between sinusoidal blood flow and access to hepatocytes is largely governed by capillary endothelial cells, including Kupffer cells and liver sinusoidal endothelial cells (LSEC). Though LSEC are active in the uptake of macromolecular plasma solutes through fluid-phase endocytosis,[10] the primary function of LSEC is to act as a selective barrier between blood and hepatocytes by restricting access to materials that can pass through pores in the endothelial cell lining of sinusoids. These pores, known as fenestrae, measure approximately 175 nm near the portal venule, while those near the hepatic venules measure approximately 147 nm.[11] However, with the decreasing average diameter of the fenestrae, a 50% increase in their frequency is observed. Due to this physical constraint, 150 nm is a generally accepted maximum size cutoff for accessing hepatocytes *in vivo*. Turbulent flow and mechanical agitation result in minimal resistance to passage of appropriately sized particles through the fenestrae.[12] Taken together, Kupffer cells and LSEC form a coordinated defense system that protects hepatocytes against injury from viruses, bacteria and toxins.

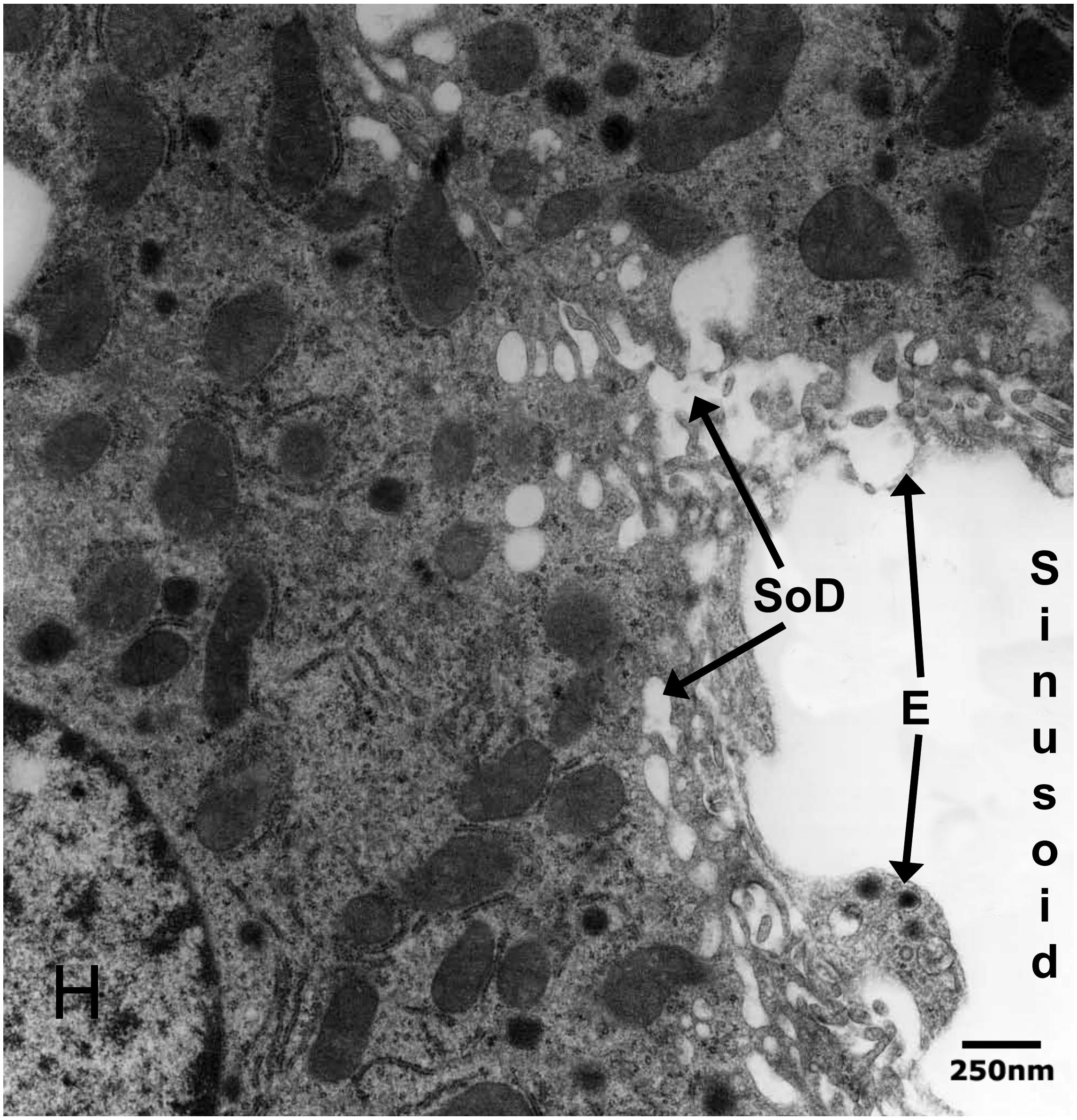

Figure 3.4. TEM image of 20 nm thick section of normal mouse liver, showing liver sinusoid, liver sinusoidal endothelial cells ('E') and space of Disse ('SoD').

Upon passing through the fenestrae in LSEC lining the sinusoids, material enters the space of Disse. This is functional extracellular space in the liver that facilitates contact between the many hepatocyte microvilli that extend into this region and material from the blood that passed through the LSEC fenestrae. Hepatocyte plasma membranes are specialized to maximize their surface area in the space of Disse with many microvilli to increase the potential for contact between the hepatocyte and blood components. Hepatocytes are only in contact with plasma components in the space of Disse.

3.3 Diseases of the Liver

The liver is a highly desirable target for gene delivery since it is involved in many diseases, including both inherited and acquired genetic disorders, and it is the largest protein factory in the body. Primary liver cancer is the sixth most frequent cancer worldwide,[13] and liver transplantation is currently the best available treatment. However, the stagnant levels of donor tissue, combined with increasing demand and a high risk of relapse, stress the need for alternative treatments. Gene therapy can impact hepatocellular carcinoma directly by transducing tumor cells with apoptosis-inducing transgenes. In addition to hepatocarcinoma, liver transplantation is currently the best approach for treating a variety of genetic diseases such as familial amyloidosis, type I and IV glycogen storage diseases, C protein deficiency and hemophilias A and B.[14] In many such cases, a genetic defect exists that does not affect the liver architecture, making gene therapy an attractive prospect. Hemophilia, for example, can be temporarily remedied by intravenous infusion of purified and recombinant factor protein, an expensive course of action that has potentially serious side-effects.[15] Gene therapy treatment of hemophilia would involve delivery of the corrective gene to the parenchymal cells of the liver and use of their protein synthesis machinery to synthesize and secrete the defective protein, thus permanently restoring the ability to clot blood. Recent promising results make genetic correction of hemophilic patients seem a reasonable goal, but significant improvements in the vectors will be required before gene therapy becomes the commonly prescribed treatment of hemophilia.

Hepatocytes, the parenchymal cells of the liver, are ideal candidates for expression of gene products that are desired in systemic circulation, such as hormones and immunomodulatory factors. This is because of hepatocytes' inherent ability to produce large amounts of protein, combined with the high volume of venous outflow from the liver to ensure efficient biodistribution. In this capacity, gene therapy to the liver may be used to create an internal protein synthesis factory to treat diseases that may or may not directly impact the liver. For example, IFN-α may confer a state of resistance to viral infectivity at one or more stages of virus entry or replication. However, fewer than 40% of patients with chronic hepatitis B or C can be treated successfully by administration of interferon α (IFN-α).[16] Even PEGylated IFN-α, which generates more sustained levels of IFN-α in the blood, is only slightly more effective. Side effects from this treatment cause the withdrawal of 20% of patients from therapy, and while it is not conclusively understood why only a minority of patients respond to treatment, it is suspected that patients infected with certain viral species may require a higher amount of IFN-α to induce a stronger antiviral response.[17] However, the high cost of this approach, combined with additional side-effects, has prompted research for new approaches. Gene transfer of IFN-α to hepatocytes in the liver has the potential to create ongoing IFN-α production, a result that has been demonstrated with an adenoviral vector in a mouse model of viral hepatitis. The activity of hepatitis B and C viruses, which are the main pathogens causing chronic liver disease, can also be inhibited by delivery of small interfering RNA.[18]

Other liver diseases, such as Gaucher's disease, are diseases of lysosomal storage that primarily affect mononuclear phagocytes. Gaucher's disease is an inherited disease leading to an error of glycoshpingolipid metabolism that leads to accumulation of non-degraded insoluble glycolipids. Such diseases are currently treated by enzyme replacement therapy, but they are also good candidates for treatment by gene therapy targeted to specialized hepatic macrophages called Kupffer cells,[19] or by enzyme production in hepatocytes followed by incorporation into macrophages.[2]

3.4 Gene Delivery to the Liver

To treat the abovementioned diseases with gene therapy, specific targeting to individual cell types in the liver will be required. Many diseases call for the targeted delivery of nucleic acid cargo to hepatocytes in the liver; however, these cells are a particularly difficult target for non-viral gene therapy. Though galactose receptors are almost exclusively found in the liver, the liver contains two types of galactose receptors. Hepatocytes abundantly express an asialoglycoprotein receptor (ASGPr) that selectively recognizes galactose and N-acetylgalactosamine (GalNAc) residues on small molecules, proteins and particles. Experiments on rat hepatocytes revealed an estimated 1.5×10^6 binding sites per cell.[20] Kupffer cells abundantly express a galactose-particle receptor (GPr) that primarily recognizes galactose residues bound to solid surfaces without recognizing small galactosylated molecules.[21]

Much work has gone towards the pursuit of hepatocyte-specific targeting of gene delivery particles and nanoparticles.[22-24] However, seemingly contradictory results frequently arise due to complexities in the system, such as excess cationic charge or instability *in vivo*. Efficient gene transfection generally requires excess polycation in the formulation to counter the anionic charge of nucleic acid and permit the condensation of nucleic acids into compact spheres. However, since cationic particles are nonspecifically adsorbed on negatively charged cell surfaces or internalized through cell-surface proteoglycans, it is generally difficult to separate the effect of charge-mediated uptake from other physicochemical properties of the system. Generalization is also complicated by the broad size distribution of most gene delivery particles, allowing only rough correlations to be made. There is an additional complication that is due to the noncovalent nature of gene delivery particles. The meta-stable particles, held together by equilibrated components, are prone to instability *in vivo* resulting from substitution of formulated components with biological molecules in serum, salt-induced destabilization or aggregation, fusion with cellular membranes or degradation of the particle.

The effect of particle size on cationic gene delivery has been studied in many systems (ref. 25 and references therein), but generalization of these results is frequently not straightforward for the reasons outlined above, and a variety of size limits have been proposed for specifically targeting the hepatic ASGPr. While 10 nm galactosylated particles were found to almost exclusively target hepatocytes in the liver,[26] a gene delivery particle that contains only a single plasmid DNA chain is expected to have a diameter of about 25 nm. Therefore, 25 nm is the minimum reasonable size for gene delivery applications. The relative uptake of 23 nm nanoparticles by hepatocytes and Kupffer cells was found to be primarily related to the density of lactose on the nanoparticle surface.[27] 23 nm nanoparticles with 60 lactose moieties on the surface primarily targeted hepatocytes while those with over 300 lactose moieties on the surface primarily targeted Kupffer cells. There have also been reports of 200-400 nm liposomes accumulating in hepatocytes following intravenous injection,[28] though Kanai *et al*.[29] observed uptake of 240 nm lecithin-coated polystyrene beads to be primarily in Kupffer and sinusoidal endothelial cells. Using neutral, targeted liposomes, Rensen *et al*.[30] identified an upper size limit for binding and internalization by the hepatic ASGPr as about 70 nm. Targeted liposomes below this limit were effectively bound and internalized via ASGPr while larger liposomes were not.

Most of the liposomes and nanoparticles discussed above were injected directly into the liver, via portal vein or inferior vena cava. Though this route of administration is possible in humans, it is certainly not ideal. Therefore, in my work presented here, liver distribution of nanoparticles will be ascertained following tail-vein injection in mice.

In our group, we have developed linear, cyclodextrin-based gene delivery systems.[31] By varying the conditions under which polyplexes are formulated, we can control various physicochemical properties of the final polyplexes, including size, surface charge, and density and type of ligand presented. However, this flexibility cannot be maximally utilized without a set of physicochemical design constraints that have been optimized for the intended gene-delivery application. We therefore set out to develop a model system that closely mimics the surface properties of our cyclodextrin-based gene-delivery particles and to define design constraints that should be applied to next generations of that system. We present here the development of a slightly anionic, stable nanoparticle-based system to guide the rational design of gene delivery to hepatocytes in the liver.

In this work, we will use galactose as a targeting ligand that is covalently bonded to well-defined nanoparticles to correlate their physicochemical properties with hepatic distribution. Since we are delivering galactosylated particles to the liver, both Kupffer cells and hepatocytes must be considered primary contributors to nanoparticle uptake, and differentiating between uptake into hepatocytes and Kupffer cells will be critical to understanding the effects of ligand targeting and particle size.

Four PEGylated polystyrene nanoparticles are synthesized, characterized and investigated in this work. Chapter Four presents a discussion of the synthesis and characterization of the nanoparticles. Chapter Five discusses nanoparticle uptake both *in vitro* and *in vivo*. *In vitro* uptake is quantified in freshly isolated hepatocytes, while differences in *in vivo* uptake of the various nanoparticles following low-pressure tail-vein injection are visualized by TEM and immunohistochemistry.

3.5 References

1. Verma, I. M.; Somia, N., Gene therapy–promises, problems and prospects. *Nature* **1997,** 389, (6648), 239-242.

2. Prieto, J.; Qian, C.; Hernandez-Alcoceba, R.; Gonzalez-Aseguinolaza, G.; Mazzolini, G.; Sangro, B.; Kramer, M. G., Gene therapy of liver diseases. *Expert Opinion on Biological Therapy* **2004,** 4, (7), 1073-1091.

3. Schenk, W. G.; Drapanas, T.; McDonald, K.; McDonald, J. C., Direct measurement of hepatic blood flow in surgical patients–with related observations on hepatic flow dynamics in experimental animals. *Annals of Surgery* **1962,** 156, (3), 463.

4. Bradfield, J. W. B., Liver sinusoidal cells. *Journal of Pathology* **1984,** 142, (1), 5-6.

5. Nolan, J. P., Endotoxin, reticuloendothelial function, and liver-injury. *Hepatology* **1981,** 1, (5), 458-465.

6. Siekevitz, P.; Palade, G. E., A Cytochemical Study on the pancreas of the guinea pig. 5. *In vivo* incorporation of leucine-C-14 into the chymotrypsinogen of various cell fractions. *Journal of Biophysical And Biochemical Cytology* **1960,** 7, (4), 619-630.

7. Peters, T., Biosynthesis of rat serum albumin. 1. Properties of rat albumin and its occurrence in liver cell fractions. *Journal Of Biological Chemistry* **1962,** 237, (4), 1181.

8. Peters, T., Biosynthesis of rat serum albumin. 2. Intracellular phenomena in secretion of newly formed albumin. *Journal Of Biological Chemistry* **1962,** 237, (4), 1186.

9. Palade, G., Intracellular aspects of process of protein-synthesis. *Science* **1975,** 189, (4200), 347-358.

10. Praaningvandalen, D. P.; Brouwer, A.; Knook, D. L., Clearance capacity of rat-liver kupffer, endothelial, and parenchymal-cells. *Gastroenterology* **1981,** 81, (6), 1036-1044.

11. Wisse, E.; Dezanger, R. B.; Charels, K.; Vandersmissen, P.; McCuskey, R. S., The Liver sieve–considerations concerning the structure and function of endothelial fenestrae, the sinusoidal wall and the space of disse. *Hepatology* **1985,** 5, (4), 683-692.

12. Weiss, M., On the degree of solute mixing in liver models of drug elimination. *Journal Of Pharmacokinetics And Biopharmaceutics* **1997,** 25, (3), 363-375.

13. Gerolami, R.; Uch, R.; Brechot, C.; Mannoni, P.; Bagnis, C., Gene therapy of hepatocarcinoma: a long way from the concept to the therapeutical impact. *Cancer Gene Therapy* **2003,** 10, (9), 649-660.

14. Kren, B. T.; Chowdhury, N. R.; Chowdhury, J. R.; Steer, C. J., Gene therapy as an alternative to liver transplantation. *Liver Transplantation* **2002,** 8, (12), 1089-1108.

15. Walsh, C. E., Gene therapy Progress and Prospects: Gene therapy for the hemophilias. *Gene Therapy* **2003,** 10, (12), 999-1003.

16. Aurisicchio, L.; Delmastro, P.; Salucci, V.; Paz, O. G.; Rovere, P.; Ciliberto, G.; La Monica, N.; Palombo, F., Liver-specific alpha 2 interferon gene expression results in protection from induced hepatitis. *Journal Of Virology* **2000,** 74, (10), 4816-4823.

17. Taylor, D. R.; Shi, S. T.; Romano, P. R.; Barber, G. N.; Lai, M. M. C., Inhibition of the interferon-inducible protein kinase PKR by HCV E2 protein. *Science* **1999,** 285, (5424), 107-110.

18. Shlomai, A.; Shaul, Y., RNA interference–small RNAs effectively fight viral hepatitis. *Liver International* **2004,** 24, (6), 526-531.

19. Germain, D. P., Gaucher's disease: a paradigm for interventional genetics. *Clinical Genetics* **2004,** 65, (2), 77-86.

20. Rice, K. G.; Weisz, O. A.; Barthel, T.; Lee, R. T.; Lee, Y. C., Defined geometry of binding between triantennary glycopeptide and the asialoglycoprotein receptor of rat heptocytes. *Journal of Biological Chemistry* **1990,** 265, (30), 18429-18434.

21. Kawasaki, T.; Ii, M.; Kozutsumi, Y.; Yamashina, I., Isolation and characterization of a receptor lectin specific for galactose/n-acetylgalactosamine from macrophages. *Carbohydrate Research* **1986,** 151, 197-206.

22. Richardson, P.; Kren, B. T.; Steer, C. J., In vivo application of non-viral vectors to the liver. *Journal Of Drug Targeting* **2002,** 10, (2), 123-131.

23. Wu, J.; Nantz, M. H.; Zern, M. A., Targeting hepatocytes for drug and gene delivery: Emerging novel approaches and applications. *Frontiers In Bioscience* **2002,** 7, D717-D725.

24. Hashida, M.; Nishikawa, M.; Yamashita, F.; Takakura, Y., Cell-specific delivery of genes with glycosylated carriers. *Advanced Drug Delivery Reviews* **2001,** 52, (3), 187-196.

25. Nakai, T.; Kanamori, T.; Sando, S.; Aoyama, Y., Remarkably size-regulated cell invasion by artificial viruses. saccharide-dependent self-aggregation of glycoviruses and its consequences in glycoviral gene delivery. *Journal Of The American Chemical Society* **2003,** 125, (28), 8465-8475.

26. Bijsterbosch, M. K.; Vanberkel, T. J. C., Lactosylated High-density-lipoprotein–a potential carrier for the site-specific delivery of drugs to parenchymal liver-cells. *Molecular Pharmacology* **1992,** 41, (2), 404-411.

27. Bijsterbosch, M. K.; Vanberkel, T. J. C., Uptake of lactosylated low-density-lipoprotein by galactose-specific receptors in rat-liver. *Biochemical Journal* **1990,** 270, (1), 233-239.

28. Scherphof, G. L.; Daemen, T.; Romero, E. D.; Kamps, J., Liposome elimination by non-phagocytic cells of the liver. *Journal Of Liposome Research* **2000,** 10, (4), 431-442.

29. Kanai, M.; Murata, Y.; Mabuchi, Y.; Kawahashi, N.; Tanaka, M.; Ogawa, T.; Doi, M.; Soji, T.; Herbert, D. C., *In vivo* uptake of lecithin-coated polystyrene beads by

rat hepatocytes and sinusoidal endothelial cells. *Anatomical Record* **1996,** 244, (2), 175-181.

30. Rensen, P. C. N.; Sliedregt, L.; Ferns, A.; Kieviet, E.; van Rossenberg, S. M. W.; van Leeuwen, S. H.; van Berkel, T. J. C.; Biessen, E. A. L., Determination of the upper size limit for uptake and processing of ligands by the asialoglycoprotein receptor on hepatocytes *in vitro* and *in vivo*. *Journal of Biological Chemistry* **2001,** 276, (40), 37577-37584.

31. Davis, M. E.; Pun, S. H.; Bellocq, N. C.; Reineke, T. M.; Popielarski, S. R.; Mishra, S.; Heidel, J. D., Self-assembling nucleic acid delivery vehicles via linear, water-soluble, cyclodextrin-containing polymers. *Current Medicinal Chemistry* **2004,** 11, (2), 179-197.

CHAPTER FOUR

SYNTHESIS AND CHARACTERIZATION OF A MODEL DELIVERY SYSTEM TO GUIDE THE RATIONAL DESIGN OF GENE DELIVERY TO THE LIVER

Reproduced with permission from Bioconjugate Chemistry, submitted for publication.

4.1 Introduction

Numerous investigators have identified the importance of carefully designing and controlling the properties of gene delivery systems for selectively targeting the liver. A prerequisite to selective targeting is particle stability *in vivo* and the minimization of nonspecific uptake. We and others have previously demonstrated the importance of PEGylation to stabilize polyplexes and to reduce their nonspecific uptake.[1] Nonspecific uptake of particles is commonly due to rapid clearance by cells of the mononuclear phagocytic system[2] and adhesion to the endothelial lining of the vascular system.[3] Such undesirable uptake is minimized by surfaces with little or no protein adsorption. In particular, certain proteins called opsonins interact with phagocyte receptors and promote recognition by scavenger cells of the reticuloendothelial organs. Phagocytosis is frequently initiated by adsorption of opsonins onto the surface of particles followed by complement activation or other recognition, leading to internalization by macrophages and intracellular processing. Dunn *et al.*[4] have demonstrated that interaction of PEGylated polystyrene nanoparticles with non-parenchymal liver cells *in vitro* decreased with higher surface densities of PEG, and also resulted in longer circulation times following intravenous injection into rats.

By formulating PEGylated cyclodextrin-based gene-delivery particles under different conditions, the size, surface charge and ligand density of the final gene delivery particle can all be adjusted.[5] However, the power of this flexibility cannot be maximized without a set of physicochemical design constraints that have been optimized for the intended gene-delivery application. In particular, we are interested in generating a set of design requirements to guide gene delivery to the liver. In this pursuit, we describe herein the development of a nanoparticle-based model system that will facilitate the systematic identification of relevant physicochemical properties that alter the hepatic distribution of nanoparticles. Further, this nanoparticle-based model is intended to mimic the surface properties achievable with the linear, cyclodextrin-based gene delivery systems developed in our laboratory.[6-9] As such, the model system will be PEGylated and must facilitate variation of parameters such as particle size, surface charge and ligand type and density.

This chapter details the synthesis and characterization of PEGylated nanoparticles with tunable physicochemical properties, while the following chapter discusses the results of hepatic uptake experiments. The nanoparticles described in this chapter are slightly anionic to minimize nonspecific uptake *in vivo*, and galactose will be used as a targeting ligand since galactose receptors *in vivo* are almost exclusively found in the liver. In particular, four nanoparticles will be described that are appropriate for uptake experiments: Gal-50 and Gal-140 are galactosylated nanoparticles with diameters of 50 nm and 140 nm, while MeO-50 and MeO-140 are methoxy-terminated 50 nm and 140 nm nanoparticles. Through the use of these nanoparticles, the effects of nanoparticle size and surface presentation of galactose on hepatic distribution in mice can be explored, and the results are presented in Chapter Five.

4.2 Materials and Methods

Fmoc-PEG$_{5000}$-NHS was purchased from Nektar (San Carlos, CA) and used as received. All other reagents and solvents were obtained from commercial suppliers and were used as received, unless specifically noted. Matrix-assisted, laser desorption/ionization time-of-flight mass spectroscopy (MALDI-TOF) was performed on a PerSeptive Biosystems Voyager DE PRO BioSpectrometry Workstation (PerSeptive Biosystems; Framingham, MA) in the positive ion mode using a 2,5-dihydroxy benzoic acid matrix. HPLC was performed on an Agilent 1100 Series HPLC (Agilent Technologies; Palo Alto, CA) with a Prevail C18 5μm column (Alltech; Deerfield, IL) and a SEDEX Model 75 Evaporative Light Scattering (ELS) detector (Richard Scientific; Novato, CA).

4.2.1 Synthesis of Galactose-PEG$_{5000}$-amine (1, Scheme 4.1)

4-aminophenyl β-D-galactopyranoside (1.79 g, 6.38 mmol) and Fmoc-PEG$_{5000}$-NHS (2.17 g, 0.43 mmol) were dissolved in about 16 mL of 1X PBS. Sulfo-NHS (97 mg, 0.44 mmol) was added, the pH was adjusted to pH 7.8 and the reaction was stirred at ambient temperature. After 6 hours, EDC was added (435 mg, 2.27 mmol), and the reaction was stirred for an additional 48 hours. The crude reaction mixture was dialyzed in 500 molecular-weight cutoff (MWCO) Float-A-Lyzers (Pierce; Rockford, IL) against water for two days with twice daily dialysate changes. The solution was dried on a rotary evaporator at temperatures not exceeding 35^{O}C. Deprotection of the amine was accomplished by stirring the off-white product in 50 mL of 25% piperidine in DMF for 4 hours at room temperature. The solution was then concentrated under reduced pressure at temperatures not exceeding 40^{O}C. The viscous liquid was transferred to polypropylene centrifuge tubes and water was added. Centrifugation and filtration through a 0.2 μm HT Tuffryn Membrane filter (VWR; West Chester, PA) resulted in complete Fmoc removal from the crude reaction mixture. The solution was subjected to extensive dialysis in 500 MWCO Float-A-Lyzers before being lyophilized to dryness. Purity was confirmed by HPLC-ELS and MALDI-TOF mass spectroscopy. Final yield: 1.25 g, 59%.

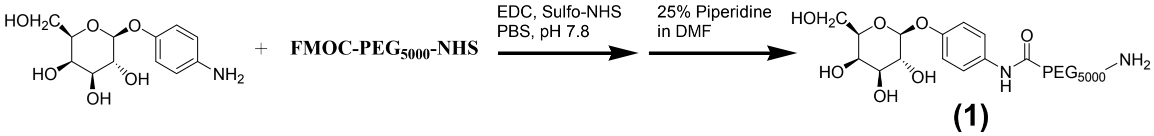

Scheme 4.1. Synthesis of Galactose-PEG$_{5000}$-NH$_2$ (**1**).

4.2.2 Synthesis of PEGylated-polystyrene Nanoparticles (2, Scheme 4.2)

FITC-embedded PEGylated-polystyrene nanoparticles were synthesized by reaction of Fluospheres (Molecular Probes; Eugene, OR) with MeO-PEG$_{5000}$-NH$_2$ or Galactose-PEG$_{5000}$-NH$_2$ (**1**). Two sizes of Fluospheres were used as starting materials in this work. 28 nm Fluospheres were used to synthesisze PEGylated nanoparticles with final diameters up to 60 nm, while nanoparticles up to 160 nm were synthesized by PEGylation of 105 nm Fluospheres. 28 nm Fluospheres were sonicated then centrifuged at 14,000*g* for 20 minutes prior to use. All Fluospheres were sonicated immediately before being added to reaction vials. Typically, 500 μL of a 2% Fluosphere suspension (3.21 μmol –COOH for 105 nm Fluospheres) is added to 32 mg MeO-PEG$_{5000}$-NH$_2$ (6.42 μmol) in a 1.5 mL Eppendorf tube and mixed to dissolve the PEG. 6.3 mg Sulfo-NHS (Pierce) is added to each tube, and 200 mM borate buffer, pH 8.2, is added up to 1 mL total volume per tube. The pH of each reaction tube is adjusted to pH 7.80 then 1.0 mg EDC (5.13mmol) is added to each tube and vortex mixed for 6 hours. Purification of 50 nm nanoparticles was accomplished by dialysis in 100k MWCO DispoDialyzers (Pierce) against a variety of salt solutions starting with 3 M NaCl and ending with 1X PBS. A minimum of 7 dialysate changes were performed until no free PEG was detected by HPLC-ELS. Workup of 140 nm nanoparticles was accomplished by cold centrifugation and repeated washes in salt solutions ranging from 4 M NaCl to final resuspension in 1X PBS. Bead concentrations were determined by comparison to fluorescence of known concentrations of as-received Fluospheres on a SpectraFluor Plus fluorescence plate reader (Tecan; Research Triangle Park, NC) with FITC filters (ex: 485 nm; em: 530 nm). Yields: 50 nm nanoparticles, typically 40%; 140 nm nanoparticles, typically 70%.

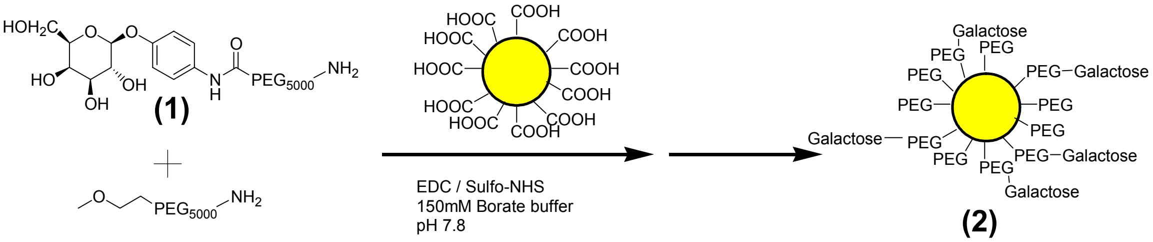

Scheme 4.2. Synthesis of PEGylated nanoparticles (**2**).

4.2.3 Particle Size and ζ-potential Measurements

Colloidal particle size was determined by photon correlation spectroscopy in 150 mM NaCl at a wavelength of 532 nm, scattering angle of 90^{O} and refractive index of 1.59 using a ZetaPALS instrument (Brookhaven Instruments; Holtsville, NY). Ten measurements on each diluted nanoparticle sample were taken, and the mean hydrodynamic diameter is reported. 50 nm nanoparticles were typically measured at $1*10^{13}$ particles/mL while 140 nm nanoparticles were typically measured at $1.5*10^{10}$ particles/mL. ζ-potential measurements were calculated from electrophoretic mobilities using the Smoluchowski equation. Nanoparticle electrophoretic mobilities were measured in 150 mM NaCl using a ZetaPALS instrument with the following conditions: fluid refractive index 1.334, electric field 5.41 V/cm and adjusted to a conductance of 15.0 mS. Three samples were each measured seven times, and the mean +/- standard deviation of each is reported.

4.2.4 Determination of Galactose Surface Density

Concentration of galactose on the surface of nanoparticles was determined with the Amplex Red Galactose/Galactose Oxidase Assay Kit (Molecular Probes; Eugene, OR) by comparison to standard curves of galactose in solution with unmodified polystyrene beads. The reaction was allowed to proceed for a minimum of 120 minutes before final absorbance readings were taken due to the different rates of reaction of galactose oxidase with galactose in solution versus with surface-immobilized galactose. Details of this reaction are provided in Appendix A.

4.2.5 RCA_{120} Lectin Agglutination

A suspension of $5.4*10^{12}$ nanoparticles in 500 µL 1X PBS is added to $4.7*10^{14}$ molecules of RCA_{120} lectin (Sigma-Aldrich; St. Louis, MO) in 500µL 1X PBS. Each lectin has two identical binding sites, for a total of $9.5*10^{14}$ galactose binding sites per experiment. Agglutination is monitored by measurement of absorbance at 560 nm. After 30 minutes, $8*10^{18}$ molecules of galactose were added in 100 µL 1X PBS to disaggregate the system.

4.2.6 TEM of Nanoparticles

Nanoparticles in water were applied to 400-mesh, freshly glow-discharged, carbon-coated copper grids for 45 seconds. After this time, excess water was removed by blotting with filter paper, and the sample was negatively stained with 2% uranyl acetate for 45 seconds before blotting. A Philips 201 electron microscope, operated at 80 kV, was used to record images.

4.2.7 Serum-Induced Nanoparticle Aggregation

Mouse serum (Sigma) was incubated in 96-well plates at $37^{O}C$ and 5% CO_2 for a minimum of 2 hours before use. $5*10^{10}$ nanoparticles were added to each 90 μL of equilibrated sera, and aggregation was monitored by measurement of absorbance at 560 nm at $37^{O}C$.

4.3 Results and Discussion

4.3.1 Gal-PEG$_{5000}$-NH$_2$ Synthesis and Characterization

Fmoc-PEG$_{5000}$-NHS was converted to high-purity Gal-PEG$_{5000}$-NH$_2$. Reaction was driven to completion by a large excess of 4-aminophenyl β-D-galactopyranoside and an additional dosing of carbodiimide coupling agent, EDC. Optimum reaction pH in NHS-mediated peptide coupling reactions is a tradeoff between the amide formation rate and the rate of deactivation of the activated NHS-ester. PEG$_{5000}$-NH$_2$ has a pKa of about

9.2,[10] and NHS-esters on the PEG chains deactivate quickly, especially above a pH of about 8. An optimal pH of about 7.8 was determined for this reaction. While the concentration of Fmoc-PEG$_{5000}$-NHS did not significantly influence reaction yield, supplementation with additional Sulfo-NHS and EDC was necessary to reactivate any carboxylic esters on the PEG that had hydrolyzed.

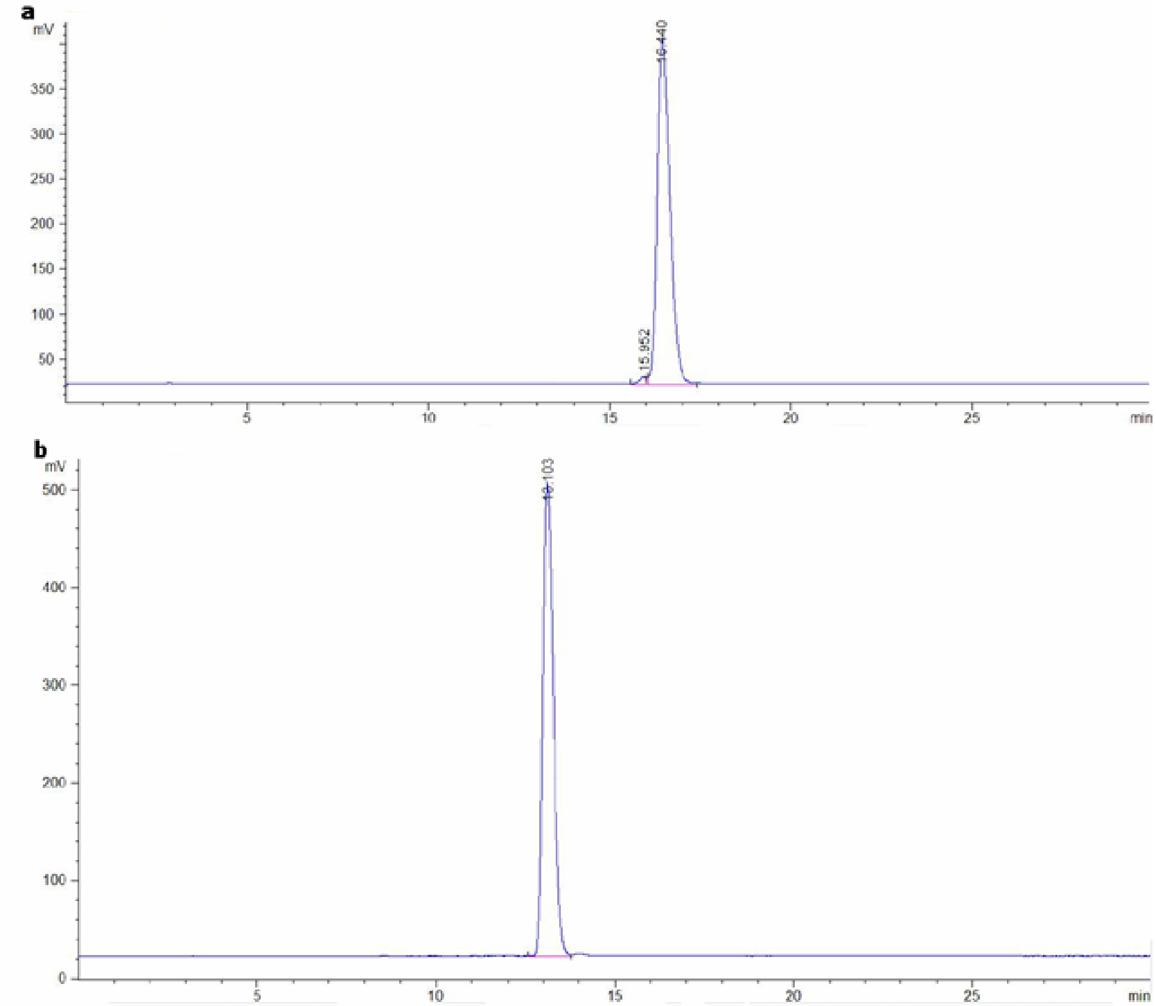

Figure 4.1. HPLC spectra of a) Fmoc-PEG$_{5000}$-COOH and b) Gal-PEG$_{5000}$-NH$_2$.

The purity of the final purified compound was determined by HPLC-ELS, as shown in Figure 4.1. Peaks representing starting materials (Figure 4.1a) and intermediates were resolved relative to the Gal-PEG$_{5000}$-NH$_2$ peak (Figure 4.1b). Purity was typically greater than 98%, as determined by HPLC.

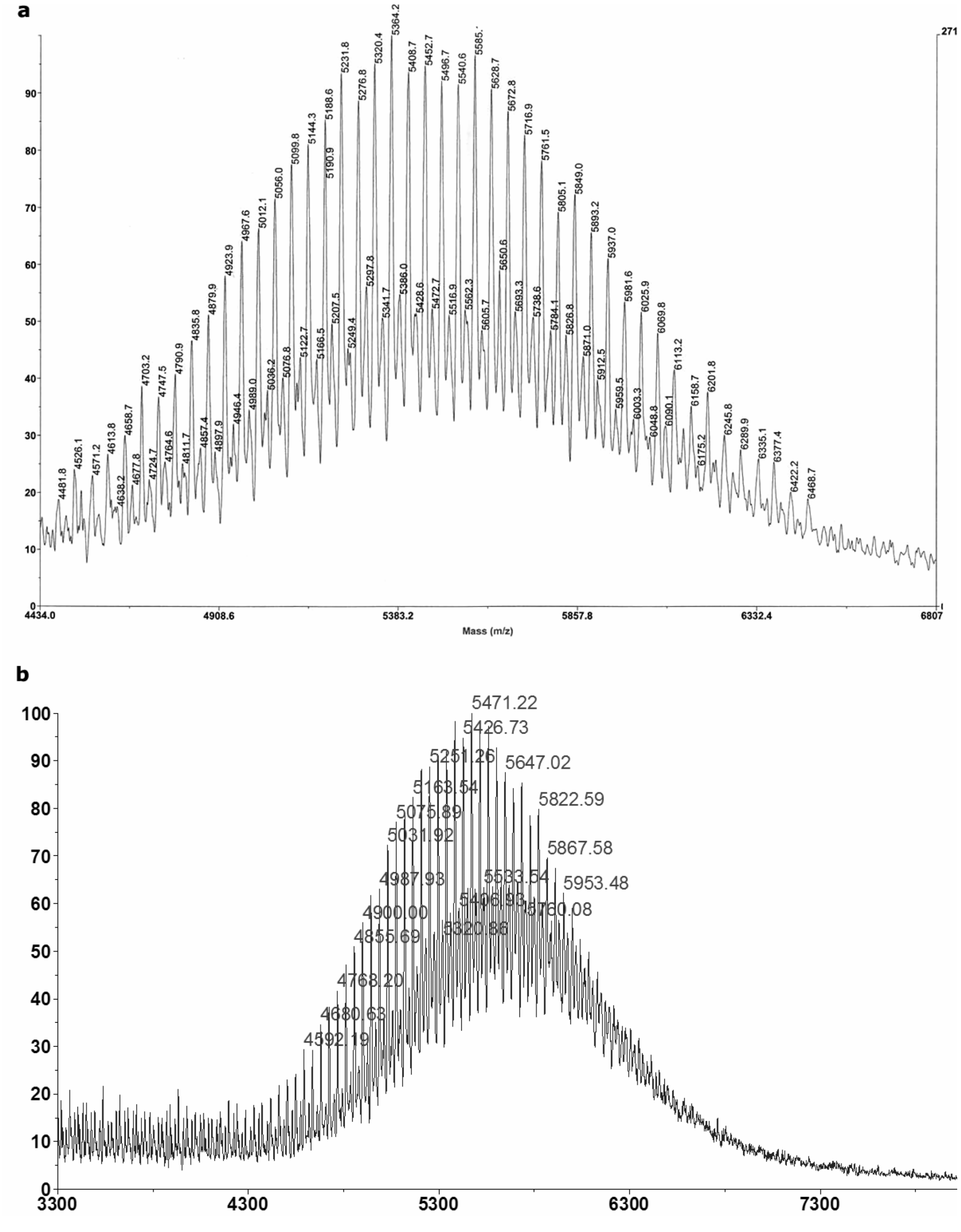

Figure 4.2. MALDI-TOF mass spectra of a) Fmoc-PEG$_{5000}$-NHS and b) Gal-PEG$_{5000}$-NH$_2$.

n	Predicted $MW_{\text{Fmoc-PEG-NHS}} + Na^+$	Observed $MW_{\text{Fmoc-PEG-NHS}} + Na^+$	Predicted $MW_{\text{Gal-PEG-NH2}} + Na^+$	Observed $MW_{\text{Gal-PEG-NH2}} + Na^+$
111	5318.1	5320.4	5251.3	5250.8
112	5362.0	5364.2	5296.3	5294.3
113	5406.1	5408.7	5340.3	5337.9
114	5450.1	5452.7	5384.3	5382.2
115	5494.1	5496.7	5428.4	5426.6
116	5538.1	5540.6	5472.4	5470.7
117	5582.2	5585.1	5516.4	5514.7
118	5626.2	5628.7	5560.4	5558.4
119	5670.2	5672.8	5604.5	5602.1
120	5714.2	5716.9	5648.5	5646.0
121	5758.3	5761.5	5692.5	5691.0
122	5802.3	5805.1	5736.5	5733.1

Table 4.1. Molecular weights of Fmoc-PEG$_{5000}$-NHS and Gal-PEG$_{5000}$-NH$_2$ for incremental numbers of ethylene oxide repeat units, with sodium counterion for comparison to peaks of MALDI-TOF spectra.

MALDI-TOF mass spectroscopy also confirmed that the reaction went to completion. Primary peaks in the MALDI-TOF spectra (Figure 4.2) line up well with predicted molecular weights (Table 4.1) of Fmoc-PEG$_{5000}$-NHS (Figure 4.2a) and Gal-PEG$_{5000}$-NH$_2$ (Figure 4.2b), according to the following formulas:

$$MW_{\text{Fmoc-PEG-NHS}} = \underset{\text{[EO repeat]}}{44.026n} + \underset{[\text{-}(CH_2)_2\text{-C(O)-NHS}]}{170.042} + \underset{\text{[-NH-Fmoc]}}{238.082}$$

$$MW_{\text{Gal-PEG-NH2}} = \underset{\text{[EO repeat]}}{44.026n} + \underset{[\text{-}(CH_2)_2\text{-C(O)-Gal}]}{326.354} + \underset{[\text{-}NH_2]}{16.023}$$

The primary population of peaks in Figure 4.2 represents $[M+Na]^+$, while the subpopulation represents $[M+H]^+$. In addition to MALDI-TOF, the average molecular weight per galactose of the final product was determined to be about 5500 with the Amplex Red Galactose Assay Kit, as expected for nearly complete galactosylation of the

PEG. Thus, the molecular weight determined from this technique compares well with the results of MALDI-TOF analysis.

4.3.2 PEGylated Nanoparticle Synthesis and Characterization

Most previous reports of PEGylating carboxy-polystyrene nanoparticles used 1 μm beads or larger.[10-12] These large particles are relatively insensitive to reaction conditions, and broadening of particle size distribution was not reported. Ploehn and Goodwin[13] PEGylated smaller carboxy-polystyrene beads (115 and 347 nm diameter), but no indication was given that polydispersity was monitored during that reaction. For my purpose of determining physicochemical design parameters for next generation gene delivery vectors, polydispersity of the final PEGylated nanoparticles should be low, monomodal and well-defined. We are interested in working with nanoparticles with hydrodynamic diameters in the range of about 45-150 nm. These relatively small polystyrene beads were found to be much more sensitive to reaction conditions than larger 200 nm beads, thus requiring careful study to identify reaction and purification conditions that resulted in pure nanoparticles with desired mean diameter, particle size distribution and extents of surface PEGylation.

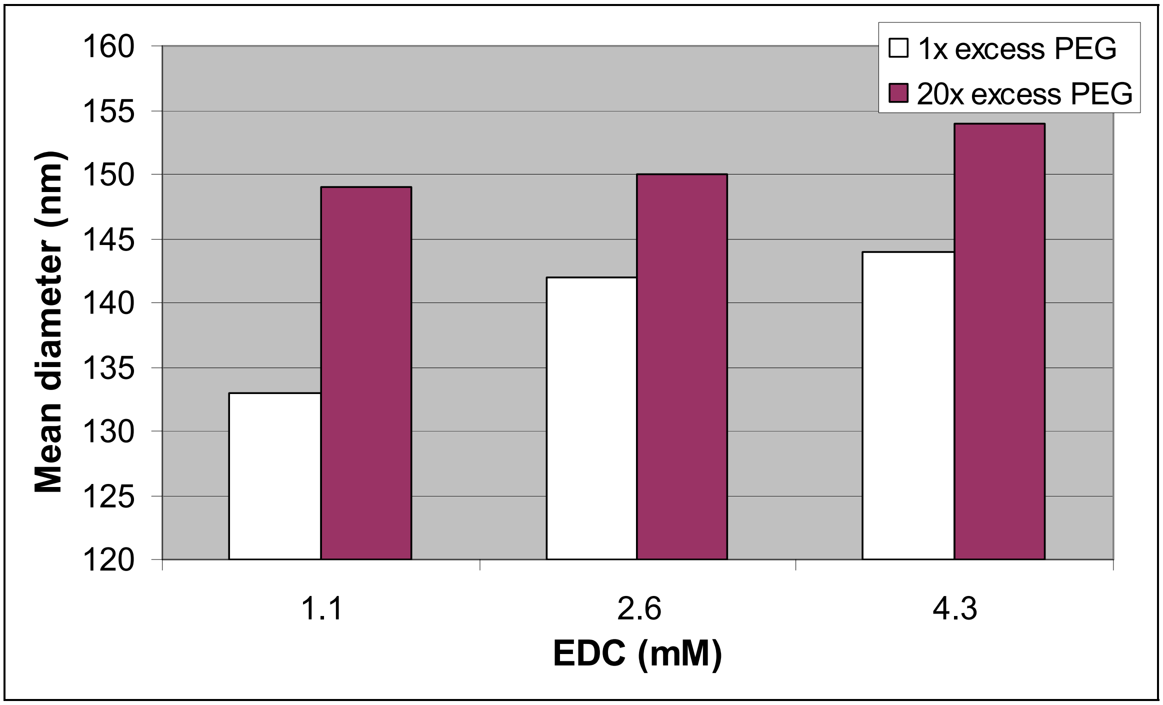

Figure 4.3. Mean hydrodynamic diameters following PEGylation of 105 nm Fluospheres with different reagent concentrations.

The extent of PEGylation, and hence the final nanoparticle hydrodynamic diameter, could be controlled by varying the concentrations of PEG and EDC during nanoparticle synthesis, as shown by the results given in Figure 4.3. While varying the concentration of PEG in the reaction simply shifted the final mean particle size without affecting the distribution, EDC concentrations above about 15 mM resulted in significant broadening of the particle size distribution.

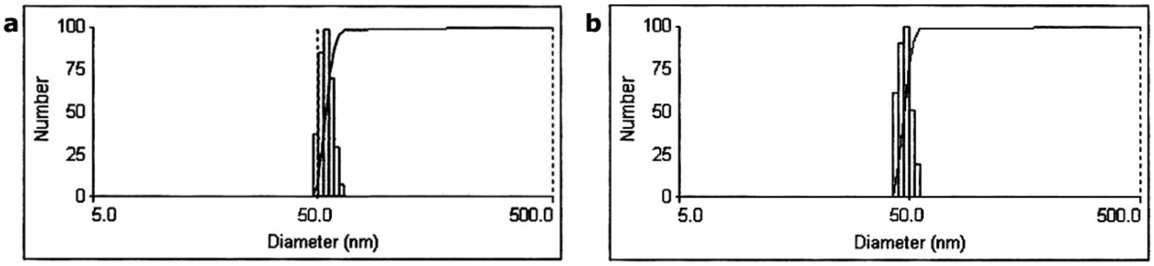

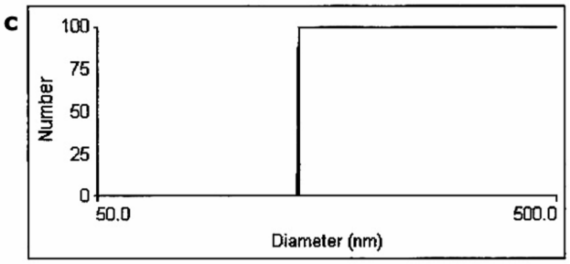

Figure 4.4. Histograms of nanoparticle hydrodynamic diameter distributions, as measured by PCS in 150mM NaCl, for a) 50 nm PEGylated polyplexes, b) 50 nm PEGylated nanoparticles, and c) 140 nm PEGylated nanoparticles.

By carefully controlling reaction conditions, nanoparticles could be synthesized with size distributions (Figure 4.4b) that closely match those of the cyclodextrin-based gene delivery particles (Figure 4.4a) they intend to mimic. PEGylated nanoparticles larger than 105 nm can be synthesized with very tight monodisperse distributions under appropriate reaction conditions (Figure 4.4c). The polydispersity of the 50 nm nanoparticles and polyplexes is about 0.06, while that of the 140 nm nanoparticles is about 0.005. Low polydispersities such as these will allow the effect of nanoparticle size on biodistribution to be clearly determined.

TEM imaging of unmodified nanoparticles validated the particle sizes measured by photon correlation spectroscopy (PCS). Particle size of unmodified polystyrene nanoparticles was found to be in good agreement between TEM and PCS measurements. This was expected, given the spherical shape of the particles and hence the appropriateness of the Stokes-Einstein expression to relate the diffusion coefficient, which is measured by PCS, to the particle size. Further, PCS measurements of particle size were performed at various concentrations to ensure the accuracy of the reported result,[14] and insignificant difference was found between these measurements.

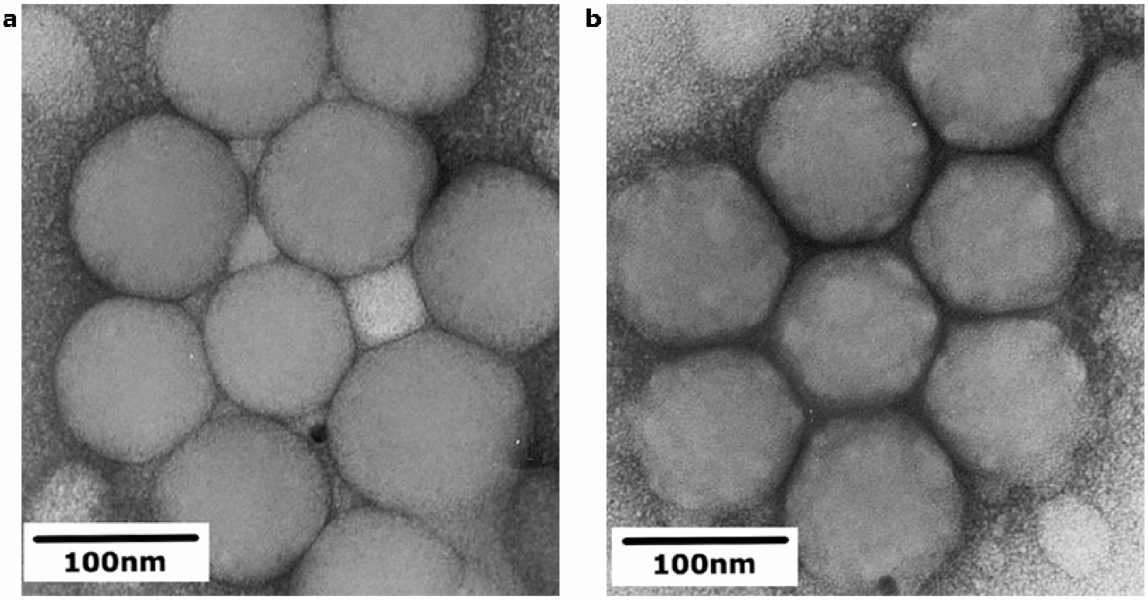

Figure 4.5. TEM images of a) unmodified 105 nm Fluosphere nanoparticles and b) PEGylated 105 nm polystyrene nanoparticles.

As seen in the TEM images in Figure 4.5a, unmodified polystyrene Fluospheres adopt a close-packed arrangement with direct polystyrene-polystyrene contact between beads, while PEGylated nanoparticles (Figure 4.5b) are separated by darkly stained PEG coronas and avoid polystyrene-polystyrene contact. Further evidence of consistent surface PEGylation was provided by our inability to separate PEGylated polystyrene nanoparticles into multiple populations by hydrophobic interaction chromatography, as described by Moghimi.[15] Moghimi also demonstrated[16] that it is critical for the entire nanoparticle surface to be PEGylated to minimize nonspecific uptake of nanoparticles by the reticuloendothelial system. It is also important that the PEGylated nanospheres be well shielded to avoid aggregation in serum. Additionally, the tight monodispersity of the 105 nm Fluospheres is evident from this image.

The stability of aqueous suspensions of 220 nm PEGylated polystyrene nanoparticles has been shown to increase dramatically for particles with hydrodynamic layer thicknesses of between 10 and 15 nm.[17] The impact of PEGylated surfaces is even more critical in salt solution, where the Debye screening length will be much shorter than the hydrodynamic layer thickness. In 150 mM NaCl, for example, the Debye screening length is about 0.8 nm. As such, any charge-charge repulsion that originated from the particle surface in pure water will no longer be influential, and the PEG layer is entirely responsible for sterically shielding the particles. In the present work, 140 nm PEGylated nanoparticles were synthesized by grafting PEG onto 105 nm polystyrene nanoparticles, resulting in hydrodynamic layer thickness of slightly more than 15 nm. As such, this PEG corona is expected to provide near maximum protection against nanoparticle flocculation. Similarly, 50 nm PEGylated nanoparticles synthesized from 28 nm polystyrene have approximate hydrodynamic layer thicknesses of 11 nm. The decreased hydrodynamic thickness of PEG with the same molar mass on the smaller beads can be explained by the increased available angular segment volume with increased surface curvature.[18]

4.3.3 Availability of Galactose for Receptor Binding

As discussed earlier, galactose is to be used as a targeting ligand on some of the PEGylated nanoparticles. The surface density of galactose on the nanoparticles can be controlled by varying the ratio of Gal-PEG_{5000}-NH_2 to MeO-PEG_{5000}-NH_2 in the reaction.

Further, the overall ratio of PEG-NH_2 to carboxyls enabled nanoparticles with different surface densities of PEG to be synthesized.

# beads per experiment	# galactose per bead	*p*mol galactose per cm^2	Total # galactose per experiment	Total # RCA_{120} binding sites per experiment
5.4E+12	1142	81.3	6.2E+15	9.5E+14
5.4E+12	556	39.6	3.0E+15	9.5E+14
5.4E+12	357	25.4	1.9E+15	9.5E+14
5.4E+12	183	13.0	9.9E+14	9.5E+14
5.4E+12	0	0	0.0E+00	9.5E+14

Table 4.2. 50 nm PEGylated nanoparticles with different surface densities of galactose for use in RCA120 agglutination assay.

Galactose moieties are presented on the surface of nanoparticles through attachment to a 5000 Da PEG chain. This experiment aims to confirm that there are galactose moieties accessible to binding large proteins such as RCA_{120}. RCA_{120} is a 120,000 Da lectin with two identical and independent galactose binding sites per molecule.[19] Five 50 nm PEGylated nanoparticles were synthesized for this study with different surface densities of galactose, as shown in Table 4.2.

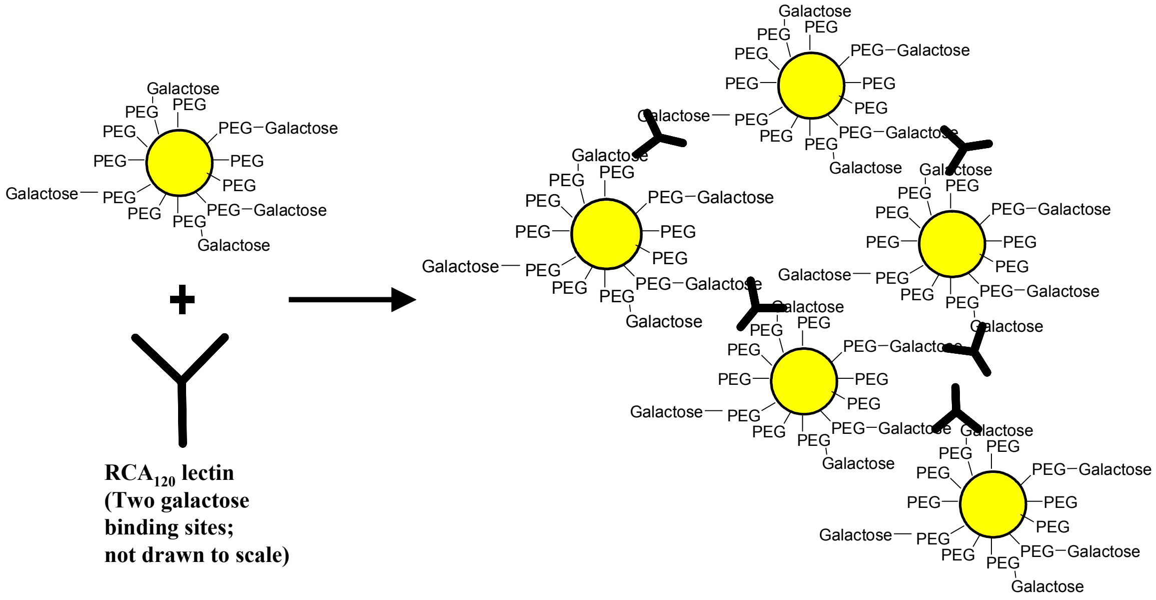

Figure 4.6. Illustration of nanoparticle agglutination as a result of RCA$_{120}$ lectin binding galactosylated nanoparticles.

When RCA$_{120}$ lectin is mixed with an appropriate number of galactosylated nanoparticles, agglutination is expected to occur. This effect is illustrated in Figure 4.6, where lectins can be seen crosslinking galactosylated nanoparticles. This crosslinked network scatters light, and progress of agglutination can be monitored by measuring absorbance at 560 nm. Agglutination should be rapidly reversible by the addition of free galactose.

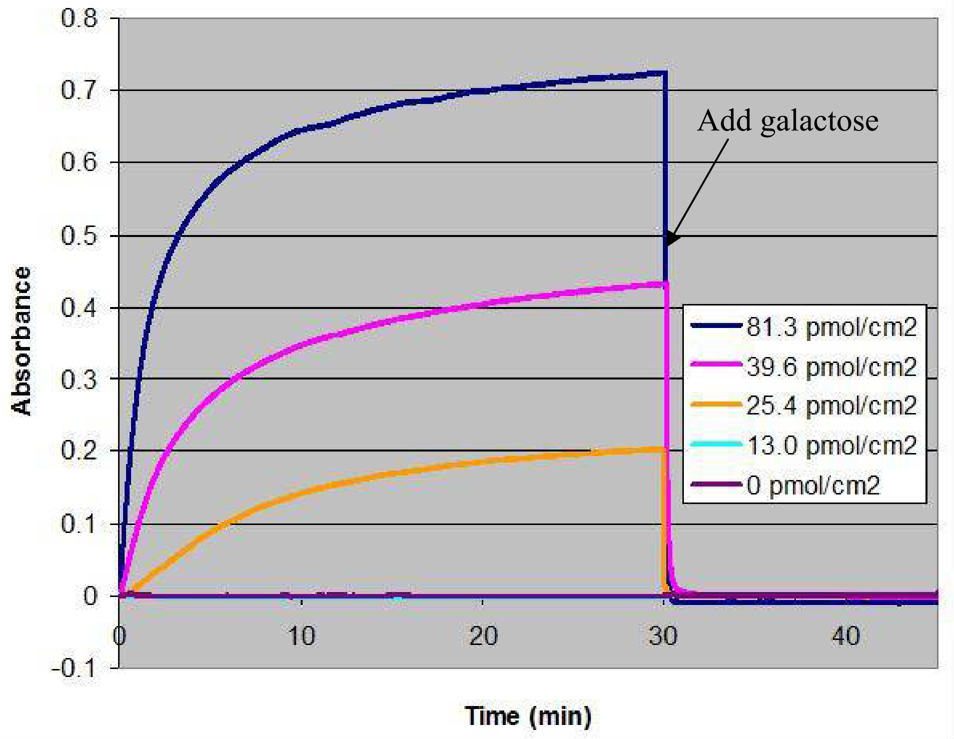

Figure 4.7. Turbidity increase due to agglutination of galactosylated 50 nm nanoparticles with RCA_{120} lectin. 100 µL of 140 mM galactose in PBS is added at 30 minutes.

By fixing the numbers of lectin molecules and nanoparticles in all experiments, the effect of galactose surface density on agglutination can be seen (Figure 4.7). Turbidity, expressed as absorbance at 560 nm, is found to increase more quickly and to a greater extent for nanoparticles with a higher surface density of galactose than for comparable nanoparticles with lower surface densities of galactose. For nanoparticles with less than about 13 *p*mol galactose/cm^2, there are comparable numbers of galactose binding sites available on the RCA_{120} lectin and galactose available on the surface of nanoparticles, and no agglutination is observed. While this result may indicate that all galactose molecules are not accessible to binding, the general availability of nanoparticle-bound galactose for protein binding is confirmed.

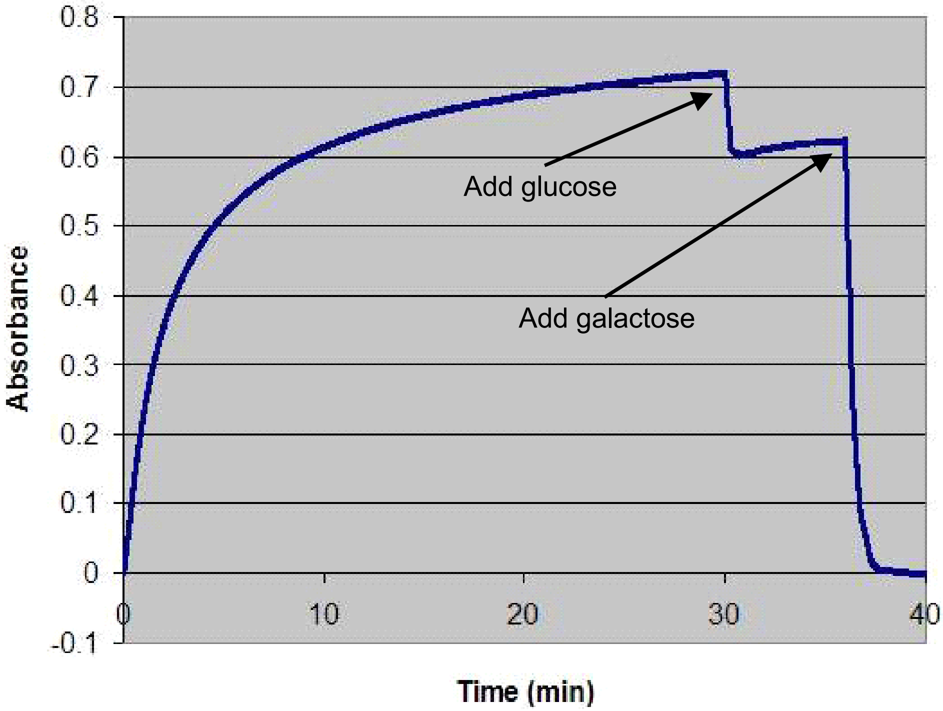

Figure 4.8. Turbidity increase of 50 nm nanoparticle with 81.3 *p*mol/cm^2 surface galactose density due to agglutination with RCA$_{120}$ lectin. 100 μL of 140 mM glucose in PBS is added at 30 minutes then 100 μL of 140 mM galactose in PBS is added at 35 minutes.

As compared to the rapid network disruption associated with galactose addition to the agglutinated solution (Figure 4.7), addition of an equal volume and concentration of glucose does not disrupt the crosslinked network (Figure 4.8). The only effect caused by addition of 100 μL of a glucose solution to the cuvette is related to dilution and is identical to the effect of adding 100 μL of water. It is thus confirmed that agglutination is due to interaction between nanoparticle-bound galactose and RCA$_{120}$ lectin molecules.

4.3.4 Description of Nanoparticles for Uptake Studies

I have thus far demonstrated that nanoparticles can be synthesized with a wide range of physicochemical properties. However, a select few must be chosen for *in vitro* and *in vivo* uptake experiments. Four nanoparticles were selected for this role, and their properties are detailed in Table 4.3.

Bead name	Mean diameter (nm)	ζ-potential (mV)	Galactose surface density (*p*mol/cm^2)
Gal-50	51.5	-2.7 +/- 1.8	25.4
MeO-50	53.5	-2.7 +/- 2.8	0
Gal-140	138.1	-2.6 +/- 2.1	30.6
MeO-140	138.7	-3.2 +/- 2.3	0

Table 4.3. Summary of physicochemical properties of the four nanoparticles to be used in uptake experiments.

Nanoparticles with mean diameters of 50 nm and 140 nm were selected for use because 1) cyclodextrin-based gene delivery particles can be conveniently synthesized in the range of about 45 nm to about 150 nm, so the nanoparticles selected for use in the present study approximate the bounds of that range, 2) access to hepatocytes through the hepatic sinusoidal wall requires passage through endothelial-cell pores that are estimated at 150-200 nm,[20] and 3) 50 nm is below the 70 nm cutoff that has been proposed for neutral liposome uptake via ASGPr.[21] The effect of galactose presentation on the surface of the nanoparticles will be investigated for 50 nm and 140 nm nanoparticles with galactose surface densities of 25-30 *p*mol/cm^2. Galactosylated 50 nm and 140 nm nanoparticles are heretofore referred to as Gal-50 and Gal-140. The equivalent nontargeted nanoparticles have methoxy terminated PEG chains and will be referred to as MeO-50 and MeO-140.

All nanoparticles in Table 4.3 have slightly anionic surface potentials (at the plane of hydrodynamic shear) to minimize nonspecific uptake. Cationic particles are internalized nonspecifically through proteoglycan receptors and may stick to anionic cell surface membranes, while highly anionic polystyrene nanoparticles have increased nonspecific uptake by scavenger receptors following complement activation.[22, 23] Unmodified, carboxylated, polystyrene beads (as-received starting material) had ζ-potentials of approximately -45 mV. The PEGylated nanoparticles have mean ζ-potentials of about -3 mV. These surfaces are nearly neutral due to the combined effect of carboxyl conversion to amides on the nanoparticle surfaces and PEG shielding of the surface charge.

4.3.5 Serum Aggregation of PEGylated Nanoparticles

In order to investigate the effect of particle size on specific uptake phenomena, the nanoparticles must remain dispersed in the presence of serum. They also must not bind serum opsonins with great affinity, as such binding has been shown to increase the hepatic uptake of 50 nm and 500 nm polystyrene nanoparticles.[24]

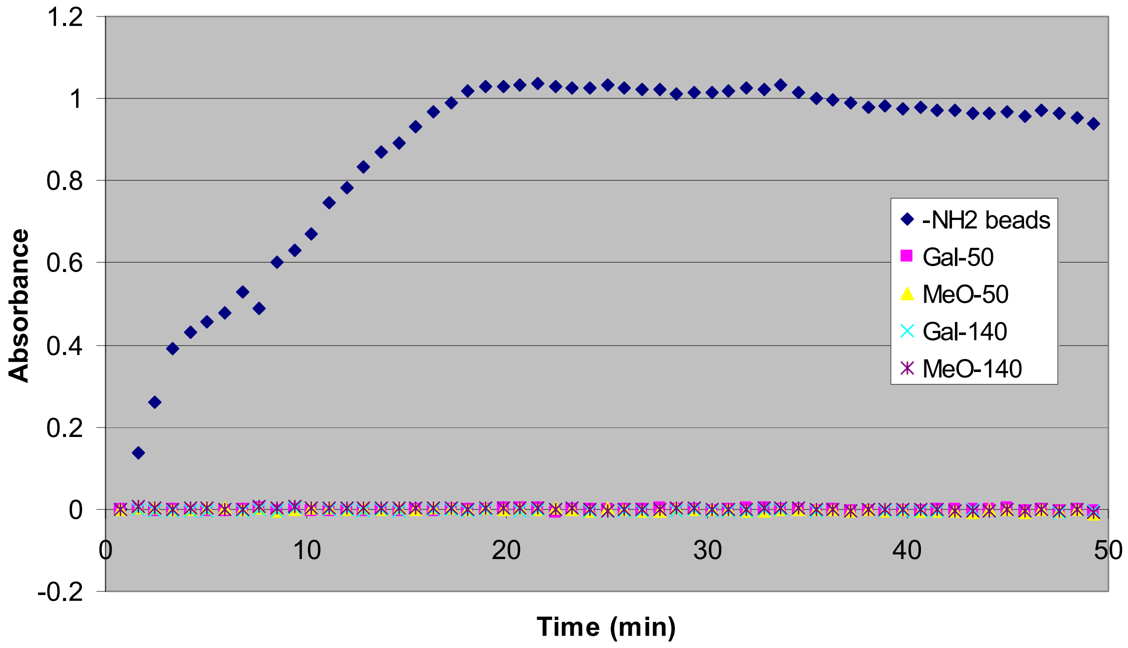

Figure 4.9. Nanoparticle aggregation in the presence of active mouse serum.

If serum proteins bind the surface of nanoparticles, crosslinking between nanoparticles would be expected to occur. Since many serum proteins are anionic, crosslinking should be more significant for cationic nanoparticles. For this reason, amino-modified polystyrene nanoparticles were used as a positive control in serum stability studies. As shown by the data in Figure 4.9, amine-functionalized nanoparticles crosslinked quickly and extensively in active mouse serum, while the PEGylated nanoparticles did not. The role of serum proteins in inducing aggregation of the amine-functionalized nanoparticles is supported by the lack of aggregation of any of the nanoparticles in 1X PBS. Despite considerable effort, aggregation of the PEGylated nanoparticles could not be induced under any conditions.

4.4 Conclusions

The synthesis and characterization of PEGylated polystyrene nanoparticles is described in this chapter. These nanoparticles have slightly anionic surface potentials to minimize nonspecific interaction with cells and tissue *in vivo*. The synthetic scheme allows for the variation of mean particle size and particle size distribution through variation in reaction conditions. The nanoparticle synthesis is also amenable to incorporation of various ligand types at tunable densities. The synthesized nanoparticles were further shown to have PEGylated surfaces that resist aggregation in serum. Finally, the availability of galactose to receptor binding was demonstrated by agglutination with RCA_{120}.

Having developed a flexible and versatile model system, four nanoparticles were synthesized specifically for the purpose of identifying design constraints to guide next generation gene delivery to the liver. In preparation for *in vitro* and *in vivo* uptake experiments, four nanoparticles were described: Gal-50 and Gal-140 are galactosylated 50 nm and 140 nm nanoparticles, while MeO-50 and MeO-140 are methoxy-terminated 50 nm and 140 nm nanoparticles. Through the use of these nanoparticles, the effects of nanoparticle size and presence of galactose on the nanoparticle surface will be explored in Chapter Five.

4.5 References

1. Mishra, S.; Webster, P.; Davis, M. E., PEGylation significantly affects cellular uptake and intracellular trafficking of non-viral gene delivery particles. *European Journal Of Cell Biology* **2004,** 83, (3), 97-111.

2. Moghimi, S. M.; Patel, H. M., Serum-mediated recognition of liposomes by phagocytic cells of the reticuloendothelial system–The concept of tissue specificity. *Advanced Drug Delivery Reviews* **1998,** 32, (1-2), 45-60.

3. Dan, C.; Wake, K., Modes Of endocytosis of latex-particles in Sinusoidal Endothelial and Kupffer cells of normal and perfused rat-liver. *Experimental Cell Research* **1985,** 158, (1), 75-85.

4. Dunn, S. E.; Brindley, A.; Davis, S. S.; Davies, M. C.; Illum, L., Polystyrene-poly(ethylene glycol) (ps-peg2000) particles as model systems for site-specific drug-delivery. 2. The effect of peg surface-density on the *in vitro* cell-interaction and *in vivo* biodistribution. *Pharmaceutical Research* **1994,** 11, (7), 1016-1022.

5. Davis, M. E.; Pun, S. H.; Bellocq, N. C.; Reineke, T. M.; Popielarski, S. R.; Mishra, S.; Heidel, J. D., Self-assembling nucleic acid delivery vehicles via linear, water-soluble, cyclodextrin-containing polymers. *Current Medicinal Chemistry* **2004,** 11, (2), 179-197.

6. Pun, S. H.; Davis, M. E., Development of a nonviral gene delivery vehicle for systemic application. *Bioconjugate Chemistry* **2002,** 13, (3), 630-639.

7. Reineke, T. M.; Davis, M. E., Structural effects of carbohydrate-containing polycations on gene delivery. 1. Carbohydrate size and its distance from charge centers. *Bioconjugate Chemistry* **2003,** 14, (1), 247-254.

8. Reineke, T. M.; Davis, M. E., Structural effects of carbohydrate-containing polycations on gene delivery. 2. Charge center type. *Bioconjugate Chemistry* **2003,** 14, (1), 255-261.

9. Popielarski, S. R.; Mishra, S.; Davis, M. E., Structural effects of carbohydrate-containing polycations on gene delivery. 3. Cyclodextrin type and functionalization. *Bioconjugate Chemistry* **2003,** 14, (3), 672-678.

10. VanDelden, C. J.; Bezemer, J. M.; Engbers, G. H. M.; Feijen, J., Poly(ethylene oxide)-modified carboxylated polystyrene latices – Immobilization chemistry and protein adsorption. *Journal of Biomaterials Science-Polymer Edition* **1996,** 8, (4), 251-268.

11. Meng, F. H.; Engbers, G. H. M.; Feijen, J., Polyethylene glycol-grafted polystyrene particles. *Journal of Biomedical Materials Research Part A* **2004,** 70A, (1), 49-58.

12. Meng, F. H.; Engbers, G. H. M.; Gessner, A.; Muller, R. H.; Feijen, J., PEGylated polystyrene particles as a model system for artificial cells. *Journal of Biomedical Materials Research Part A* **2004,** 70A, (1), 97-106.

13. Ploehn, H. J.; Goodwin, J. W., Rheology of aqueous suspensions of polystyrene latex stabilized by grafted poly(ethylene oxide). *Faraday Discussions* **1990**, (90), 77-90.

14. Dejaeger, N.; Demeyere, H.; Finsy, R.; Sneyers, R.; Vanderdeelen, J.; Vandermeeren, P.; Vanlaethem, M., Particle sizing by photon-correlation spectroscopy. 1. monodisperse lattices – Influence of scattering angle and concentration of dispersed material. *Particle and Particle Systems Characterization* **1991,** 8, (3), 179-186.

15. Gbadamosi, J. K.; Hunter, A. C.; Moghimi, S. M., PEGylation of microspheres generates a heterogeneous population of particles with differential surface characteristics and biological performance. *Febs Letters* **2002,** 532, (3), 338-344.

16. Moghimi, S. M., Chemical camouflage of nanospheres with a poorly reactive surface: towards development of stealth and target-specific nanocarriers. *Biochimica et Biophysica Acta-Molecular Cell Research* **2002,** 1590, (1-3), 131-139.

17. Wind, B.; Killmann, E., Adsorption of polyethylene oxide on surface modified silica stability of bare and covered particles in suspension. *Colloid and Polymer Science* **1998,** 276, (10), 903-912.

18. Killmann, E.; Sapuntzjis, P., Dynamic light-scattering of polystyrene latex and silica with adsorbed poly(ethylene oxide) layers – Influence of ionic-strength and coverage. *Colloids and Surfaces A-Physicochemical and Engineering Aspects* **1994,** 86, 229-238.

19. Vanwauwe, J. P.; Loontien, F.G.; Debruyne, C. K., Interaction of ricinus-communis hemagglutinin with polysaccharides and low-molecular weight carbohydrates. *Biochimica et Biophysica Acta* **1973,** 313, (1), 99-105.

20. Wisse, E.; Dezanger, R. B.; Charels, K.; Vandersmissen, P.; McCuskey, R. S., The liver sieve – Considerations concerning the structure and function of endothelial fenestrae, the sinusoidal wall and the space of Disse. *Hepatology* **1985,** 5, (4), 683-692.

21. Rensen, P. C. N.; Sliedregt, L.; Ferns, A.; Kieviet, E.; van Rossenberg, S. M. W.; van Leeuwen, S. H.; van Berkel, T. J. C.; Biessen, E. A. L., Determination of the upper size limit for uptake and processing of ligands by the asialoglycoprotein receptor on hepatocytes *in vitro* and *in vivo*. *Journal of Biological Chemistry* **2001,** 276, (40), 37577-37584.

22. Gref, R.; Miralles, G.; Dellacherie, E., Polyoxyethylene-coated nanospheres: effect of coating on zeta potential and phagocytosis. *Polymer International* **1999,** 48, (4), 251-256.

23. Ogawara, K.; Yoshida, M.; Higaki, K.; Kimura, T.; Shiraishi, K.; Nishikawa, M.; Takakura, Y.; Hashida, M., Hepatic uptake of polystyrene microspheres in rats: Effect of particle size on intrahepatic distribution. *Journal of Controlled Release* **1999,** 59, (1), 15-22.

24. Ogawara, K.; Yoshida, M.; Takakura, Y.; Hashida, M.; Higaki, K.; Kimura, T., Interaction of polystyrene microspheres with liver cells: Roles of membrane receptors and serum proteins. *Biochimica et Biophysica Acta-General Subjects* **1999,** 1472, (1-2), 165-172.

CHAPTER FIVE

RELATIONSHIP BETWEEN PHYSICOCHEMICAL PROPERTIES AND HEPATIC DISTRIBUTION AND UPTAKE OF PEGYLATED NANOPARTICLES

Reproduced with permission from Bioconjugate Chemistry, submitted for publication.

5.1 Introduction

In Chapter 4, I described the synthesis and characterization of slightly anionic PEGylated polystyrene nanoparticles that are appropriate for *in vitro* and *in vivo* biodistribution experiments. In particular, four nanoparticles were selected for *in vivo* experiments, and their properties are shown in Table 5.1.

Bead name	Mean diameter (nm)	ζ-potential (mV)	Galactose surface density (*p*mol/cm^2)
Gal-50	51.5	-2.7 +/- 1.8	25.4
MeO-50	53.5	-2.7 +/- 2.8	0
Gal-140	138.1	-2.6 +/- 2.1	30.6
MeO-140	138.7	-3.2 +/- 2.3	0

Table 5.1. Summary of physicochemical properties of the four nanoparticles to be used in uptake experiments.

In this chapter, I will discuss the *in vitro* hepatocyte uptake and *in vivo* hepatic distribution of the four nanoparticles described in Table 5.1. Comparable 50 nm nanoparticles and 140 nm nanoparticles that differ only in the presence of galactose on their surfaces will allow the impact of galactose to be identified. Galactose receptors are almost exclusively found in the liver, though both hepatocytes and Kupffer cells display galactose receptors. Hepatocytes abundantly express an asialoglycoprotein receptor (ASGPr) that selectively recognizes galactose and N-acetylgalactosamine (GalNAc) residues on small molecules, proteins and particles. Kupffer cells abundantly express a galactose-particle receptor (GPr) that primarily recognizes galactose residues bound to solid surfaces without recognizing small galactosylated molecules.[1] While both ASGPr and GPr recognize galactosylated particles, uptake via these receptors is differentially affected by particle size. While an upper size limit of about 70 nm has been proposed for

ASGPr-mediated uptake of particles,[2] Kupffer cells preferentially internalize 500 nm particles over 80 nm particles.[3] Gal-50 is below the proposed cutoff for ASGPr-mediated uptake, while Gal-140 is above that cutoff and may also be recognized more readily by the Kupffer cell GPr. Nanoparticles were synthesized with slightly anionic surface potentials to minimize nonspecific interaction with cells and tissue.

In vitro uptake experiments will make use of freshly isolated hepatocytes as compared to hepatocellular carcinoma cell lines to provide results that more closely represent hepatocyte uptake *in vivo*. By their nature, carcinoma cells divide much more rapidly than non-oncogenic hepatocytes, and their uptake mechanisms are altered accordingly. Since we are interested in studying nanoparticle uptake and distribution in hepatic tissue, use of primary hepatocytes will more closely approximate the uptake response of hepatocytes *in vivo* than would immortalized cell lines. Furthermore, many cultured cell lines have been cultured for extended periods of time, resulting in heterogeneous populations of cells. Microarray comparison of mRNA expression levels of whole rat liver, several rat liver cell lines and primary cultured hepatocytes indicated that the cell lines were most dissimilar from whole liver, and that they also differed significantly from primary hepatocytes. In addition, the duration of culture had a profound effect on mRNA levels. Significant differences in ethanol toxicity,[4] transferrin internalization rate[5] and ASGPr receptor levels have also been reported between hepatocellular carcinoma cell lines and normal hepatocytes. For example, HepG2 cells, a human malignant hepatic cell line, have only about 225,000 ASGPr per cell. Rat hepatocytes have approximately 550,000 ASGPr total per cell. But while HepG2 cells present 87% of the total cellular ASGPr on the cell surface,[6] only about 250,000[7] of the hepatocyte ASGPr are expressed on the cell surface while the additional 300,000 constitute an intracellular pool. This intracellular pool of ASGPr has been implicated in intracellular trafficking and processing of receptor and ligand, including a role in transport in the secretory pathway following ligand internalization.[8] Therefore, immortalized cell lines such as HepG2 do not provide an ideal *in vitro* system to guide *in vivo* hepatic biodistribution studies, and freshly isolated hepatocytes will be used in this work.

In vitro uptake into hepatocytes will be assayed both with plated cells, to compare the dose fraction internalized by the cells, and with suspended cells to study the kinetics of nanoparticle association with hepatocytes. *In vivo* hepatic distribution will be determined by TEM and immunohistochemistry, which allow for the visualization of liver sections from mice that received tail-vein injections of the different nanoparticles described in Table 5.1.

5.2 Materials and Methods

5.2.1 Animals

Female Balb/c mice were obtained from Charles River Laboratories (Wilmington, MA) and were approximately 10–15 weeks old at the time of the study. The animals were fed autoclaved LabDiet 5010 (Purina Mills; St. Louis, MO) and drank reverse osmosis, 1ppm chlorine, autoclaved water from bottles. The mice were housed on ventilated racks with autoclaved nestlets and Aspen Chip bedding (Nepco; Warrensburg, NY) on a 13-hour light cycle at 72–76^{O}F and 30–70% humidity. Caltech specifically complies with the recommendations of the *Guide for Care and Use of Laboratory Animals* with respect to restraint, husbandry, surgical procedures, feed and fluid regulation, and veterinary care. The animal program at Caltech is AAALAC accredited.

5.2.2 Hepatocyte Isolation

Mouse hepatocytes were isolated from female Balb/c mice (18–25 g, 10–15 weeks old) by the standard two-step perfusion with collagenase by the Cell Culture Core of the USC Research Center for Liver Diseases, as previously described.[9] Briefly, mice were anesthetized with pentobarbital sodium (60 mg/kg), and the liver was perfused via the portal vein at 3 mL/min first with Ca^{2+} and Mg^{2+}-free perfusion buffer (10 mM *N*-2-hydroxyethylpiperazine-*N*'-2-ethanesulfonic acid (HEPES), 137 mM NaCl, 5 mM KCl, 0.5 mM NaH_2PO_4, and 0.4 mM Na_2HPO_4, pH 7.2) for 3 minutes and then with perfusion buffer supplemented with 5 mM $CaCl_2$ and 0.05% (w/v) collagenase (type IV; pH 7.5) for 3 minutes. The liver was then carefully removed, and its capsular membrane was gently peeled off. The dispersed cells, in cold Hank's-HEPES buffer containing 0.1% BSA, were filtered through cotton mesh and allowed to settle. Dead parenchymal hepatocytes were removed by density gradient centrifugation on Percoll (Amersham Biosciences; Piscataway, NJ) to give parenchymal cells of > 90% purity and >90% viability, as determined by trypan blue exclusion. Appropriate numbers of hepatocytes, as described in the following sections, were transferred to collagen-coated dishes that were maintained at $37^{O}C$ with 95% humidity and 5% CO_2. After one hour, the unattached cells were removed by aspiration, and culture medium changes were performed daily thereafter. Complete hepatocyte media consisted of Dulbecco's

Modified Eagle's Medium/F12 without phenol red (Invitrogen; Carlsbad, CA), supplemented with L-methionine, 100 U/mL penicillin, 0.1 mg/mL streptomycin, 0.25 mg/mL amphotericin B (Invitrogen) and 9% fetal bovine serum.

5.2.3 Nanoparticle Uptake by Adherent Hepatocytes

Following hepatocyte isolation, 100,000 hepatocytes were transferred to each well of collagen-coated 24-well plates. After a minimum of 24 hours of incubation in complete medium, hepatocytes were incubated in OptiMem (Invitrogen) that does not contain any Cu^{2+} or Zn^{2+} ions for two hours prior to experimentation, to allow the hepatic asialoglycoprotein receptor (ASGPr) to adopt an accessible conformation and to achieve maximum uptake potential.[10] The medium in each well was then replaced with the appropriate nanoparticle-containing medium, or PBS-containing medium for wells to be used in the preparation of standard curves. Hepatocytes were incubated in 200 μl of Optimem containing $7.5*10^9$ nanoparticles/mL for 40 minutes. After this time, the medium was removed, cells were washed with cold HEPES buffer then lysed with 1X Cell Culture Lysis Reagent (Promega; Madison, WI). Fluorescence of the soluble portion of the cell lysates was measured and compared to standard curves prepared by adding known numbers of beads to hepatocyte cell lysates.

5.2.4 Preparation of Suspended Hepatocytes

Following hepatocyte isolation, about $7*10^6$ hepatocytes were transferred to a collagen-coated 10 cm^2 dish and incubated for a minimum of 24 hours in complete medium. Hepatocytes were detached with Trypsin-EDTA (Invitrogen), spun down at 400*g* for 5 minutes and resuspended at $2*10^6$ cells/mL in complete hepatocyte media in 50 mL polypropylene tubes, 10mL total per tube, with 40μm polypropylene Falcon Cell Strainers (Fisher; Hampton, NH) to minimize contamination while permitting gas exchange. After incubating at 37^OC and 5% CO_2 overnight, hepatocytes were spun down, washed with HEPES buffer and resuspended in Optimem with 3% fetal bovine serum in polypropylene tubes. Following 2 hours incubation in media lacking Cu^{2+} or Zn^{2+} ions, hepatocytes were spun down, resuspended in Optimem and aliquoted for experimentation. Experimental details concerning data collection are described in the following section.

5.2.5 Flow Cytometry Analysis of Nanoparticle Uptake Kinetics

Single cell suspensions of $2*10^6$ hepatocytes per mL were prepared as described above and kept on ice prior to analysis. Immediately before use, cell suspensions were warmed to 37^OC, nanoparticles were added to the FACS tube and analysis was started within 10 seconds. Flow cytometry analyses were performed using a BD Bioscience FACSCalibur (San Jose, CA) equipped with a 488 nm argon laser and a 635 diode laser and Cellquest software. Dead cells, aggregates and Kupffer cells were removed from the analyses by live gating on forward and side scatter. Green fluorescence emitted by the beads was measured with a 530/30 nm bandpass filter. Autofluorescent cells were removed by using a red channel measured by a 585/42 nm bandpass filter to gate out bright cells. Flow rates were kept constant at 35 μL per minute. Per cell mean fluorescence from gated cells was analyzed by downloading the Cellquest list mode data file to FlowJo (Tree Star Inc.; Ashland, OR), gating the cells and then exporting the gated data to Microsoft Excel. Mean fluorescence signals were averaged over all cells analyzed in five-second intervals. The percentage of FITC-positive cells was calculated based on the ratio of the number of FITC-positive cells in each five-second interval to the total number of cells counted in that interval. FITC mean values are normalized by the number of fluorescein equivalents per bead.

5.2.6 Bulk Liver Uptake of Nanoparticles

Twenty minutes after tail-vein injection of 100 μL saline containing $8*10^{11}$ nanoparticles per 20 g mouse, mice were sacrificed and their livers were immediately excised, weighed and split into two comparable pieces. Each piece was then transferred to individual Lysing Matrix D tubes (Qbiogene; Irvine, CA) and subjected to three cycles of mechanical agitation in a FastPrep FP120 instrument (Qbiogene). Cellular membranes were disrupted by three freeze-thaw cycles, and an additional cycle of mechanical agitation resulted in homogeneous liver samples that were lyophilized to dryness. FITC was subsequently extracted into chloroform for comparison to a standard curve. Standard curves were created by adding a known number of nanoparticles to liver pieces from untreated mice, followed by identical homogenization and extraction processing to the samples described above. Data as shown represent tissue uptake of nanoparticles, which has been determined by subtracting the approximate fluorescence due to nanoparticles in liver blood vessels from the fluorescence of the wet liver tissue. All experiments were repeated in triplicate.

5.2.7 TEM Imaging of Liver Tissue

For electron microscopy, excised liver tissue was cut into 1 mm^3 cubes and fixed in 2% glutaraldehyde in100 mM sodium cacodylate buffer (pH 7.4). After washing in a sodium cacodylate buffer, the tissue was postfixed in 1% osmium tetroxide in sodium cacodylate buffer for 1 hour. After rinsing, the tissue was embedded in Epon-Spurr resin. Thin sections of 20 nm were prepared, contrasted with uranyl acetate and lead citrate, and observed on a Hitachi 600 electron microscope (Hitachi Ltd.; Tokyo, Japan).

5.2.8 Overlay of Fluorescence and TEM Images

Mouse parenchymal liver cells were isolated as described above. Cells were seeded at a density of $3*10^5$ cells per collagen-coated glass cover slip in 6-well culture plates. After a minimum of 24 hours incubation in complete medium, hepatocytes were incubated in OptiMem (Invitrogen) for two hours prior to experimentation. Medium in each well was then replaced with 200 µl Optimem containing $7.5*10^9$ nanoparticles/mL and incubated for 40 minutes. Cells were then washed with HEPES buffer and fixed in 2.5% glutaraldehyde for 2 hours at room temperature. Glass cover slips were mounted with Vectashield mounting media (Vector Laboratories; Burlingame, CA). To identify the same cell for light microscopy and TEM, spots were made with an ultra-fine tipped pen on the cell-containing cover slip.

5.2.9 Immunohistochemical Staining

Mice received a 100 μL tail-vein injection containing $8*10^{11}$ nanoparticles per 20 g mouse weight. The injection was performed over less than five seconds using a 26-gauge needle in all cases. Twenty minutes after the injection of nanoparticles, mice were sacrificed and their livers were immediately excised, embedded in Tissue-Tek OCT embedding compound (Sakura Finetek USA; Torrance, CA) and stored in 2-methylbutanol on dry ice. Frozen liver sections were cut 12 μm thick, and two sections were placed on each slide for imaging. Remaining blocks were stored at $-80^{O}C$. The slides were washed with PBS to remove OCT, and a perimeter was drawn around each pair of sections with an ImmEdge pen (Vector Laboratories). Each section was then fixed with 4% paraformaldehyde and rinsed with TBS (100 mM Tris and 150 mM NaCl, adjusted to pH 7.4). Slides were incubated with blocking buffer, then any biotin or streptavidin in the sections was blocked with the Streptavidin/Biotin Blocking Kit (Vector Laboratories) and rinsed with TBS. Continuing with TBS washes between each step, slides were sequentially incubated with donkey blocking buffer, goat anti-ASPGR1 antibody (Santa Cruz Biotechnology; Santa Cruz, CA), donkey anti-goat IgG-biotin (Santa Cruz Biotechnology) and finally QDot655 Streptavidin conjugate (Quantum Dot Corp.; Hayward, CA). Following a final set of TBS washes, slides were mounted with Vectashield Mounting Medium with DAPI (Santa Cruz Biotechnology) nuclear stain.

5.2.10 Immunohistochemistry Imaging

Images were acquired at the CHLARI Congressman Julian Dixon Cellular Image Core with a Leica DM RXA microscope using a HC Plan 20x/0.70NA Ph2 DIC C objective lens, 1.25x optovar and Koehler illumination (Leica Microsystems Inc.; Bannockburn, IL). A SKY/CD-300/VDS-1300 spectral imager with EasyFISH software (Applied Spectral Imaging, Inc.; Carlsbad, CA) was used. The 640 x 480 pixel images were acquired with 2 x 2 binning (1.039 um/pixel). All images acquired during a single session for each size nanoparticle were captured with identical exposure times and saved as 16-bit/channel EasyFISH files. Images were also saved as 24-bit RGB color images using constant slope contrast settings for each channel. Phase contrast and GFP images were acquired using a Chroma 41004 filter set (HQ480/40x, Q505LP dichroic, HQ535/50m), DAPI images were acquired using a Chroma 41001 filter set (HQ480/40x, Q505LP, HQ535/50m) (Chroma Technology Corp.; Brattleboro, VT) and QD655 images were acquired with a Leica N2.1 filter set 513832 (BP515-560, 580, LP590).

5.3 Results and Discussion

5.3.1 *In Vitro* Uptake Results

Hepatocytes have access to high concentrations of amino acids and other nutrients from the digestive tract and endogenous protein catabolism, as well as a rich network of endoplasmic reticulum that enables their efficient secretory processes.[11] As such, hepatocytes are the primary site of secretory protein synthesis in the body and are accordingly involved in many disease states. Hepatocytes are therefore a highly desirable target for gene therapy.

Nanoparticle uptake into cultured hepatocytes can provide an initial indication of the effect of size and galactose targeting on hepatic uptake. Besides the complex microenvironment in the liver surrounding each hepatocyte, as compared to the loosely packed monolayer of hepatocytes in culture, freshly isolated hepatocytes were found to have only 17% of their ASGPr on the cell surface[12] as compared to between 40% and 60% ASGPr presentation for hepatocytes in the liver. After incubation at 37^{O}C, the receptor distribution in isolated hepatocytes has been reported to approach 50% on the cell surface with the remainder associated with intracellular Golgi, microsomal and lysosomal membranes.[13] To minimize the transient nature of these effects, hepatocytes were incubated in complete hepatocyte medium, as described in Materials and Methods, for a minimum of 24 hours prior to use.

Nanoparticle uptake by plated hepatocytes was assayed by measuring the fluorescence of whole cell lysates after incubating freshly isolated hepatocytes with nanoparticles and washing with chilled HEPES buffer. In all *in vitro* uptake experiments, hepatocytes were incubated for two hours in media that does not contain any Cu^{2+} or Zn^{2+} ions. McAbee and Jiang[10] have demonstrated that these ions result in the reversible accumulation of inactive ASGPr both intracellularly and on the cell surface, so hepatocytes were incubated at 37^{O}C and washed in the absence of Cu^{2+} or Zn^{2+} before experiments were initiated.

Nanoparticle type	% Dose in Hepatocyte Lysate
Gal-50	21.9%
MeO-50	9.0%
Gal-140	1.6%
MeO-140	1.5%

Table 5.2. *In vitro* uptake of nanoparticles by freshly isolated hepatocytes, as quantified by the overall fluorescence of cell lysates by comparison to a standard curve also using hepatocyte lysates.

The results of nanoparticle uptake into plated hepatocytes are shown in Table 5.2. It is apparent that nanoparticles with 50 nm diameters are taken up to a much greater extent than are those with 140 nm diameter. The presence of galactose on 140 nm beads has no apparent effect, with about 1.5% of each MeO-140 and Gal-140 dose being internalized by hepatocytes. Galactose presentation does, however, significantly affect the uptake of 50 nm beads. While about 9% of MeO-50 nanoparticles were internalized during the course of the experiment, greater than 20% of Gal-50 nanoparticles were internalized. These results presented in Table 5.2 are consistent with the findings of Rensen *et al.*[2] that hepatocytes preferentially internalize targeted liposomes with diameters less than about 70 nm. In place of glycolipid-containing liposomes, the present work makes use of slightly anionic PEGylated nanoparticles that closely mimic the surface properties of stabilized gene delivery polyplexes. Since PEGylation is commonly required to achieve long circulation times of nanoparticles *in vivo*, the results obtained with this system are expected to directly translate to a wide variety of gene and drug delivery systems.

When formation of endocytic vesicles is accompanied by uptake of extracellular fluid along with any macromolecules or particles present, uptake is said to occur by fluid-phase endocytosis, or pinocytosis. Vesicles resulting from pinocytosis are generally less than 100 nm in diameter, so it can be speculated that the fairly high uptake of nontargeted 50 nm nanoparticles by hepatocytes *in vitro* may at least partially be due to pinocytosis.

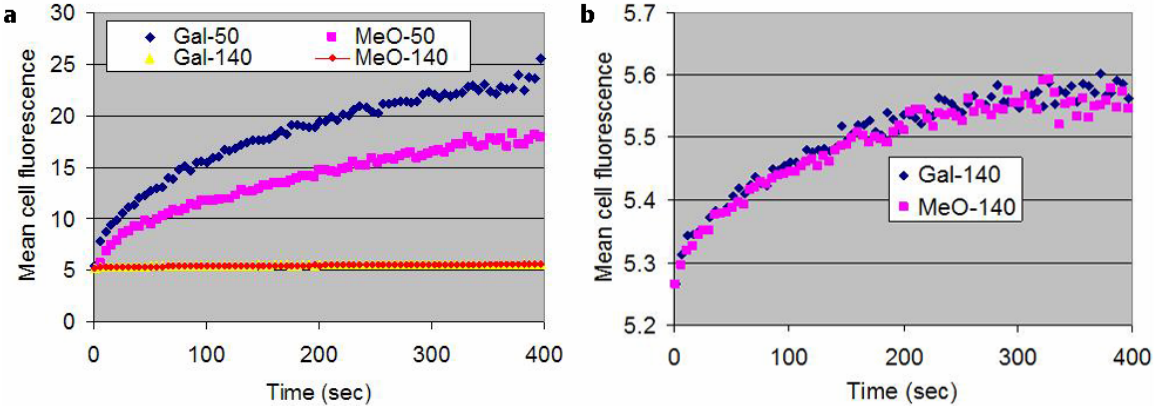

Figure 5.1. Kinetics of nanoparticle uptake by suspended hepatocytes, as analyzed by flow cytometry. a) Uptake of 50 nm and 140 nm nanoparticles are shown on the same scale. b) Uptake of 140 nm nanoparticles are shown on an expanded scale.

To help guide *in vivo* experiments and to better understand *in vitro* uptake, nanoparticle uptake kinetics were monitored with suspended, freshly-isolated hepatocytes, and the results are shown in Figure 5.1. This experiment confirms the results obtained with plated hepatocytes. Gal-140 and MeO-140 are taken up only minimally compared to the 50 nm nanoparticles (Figure 5.1a), and no difference in uptake was seen in 140 nm beads (Figure 5.1b) displaying galactose or methoxy on their surfaces. Once again, uptake of the nontargeted MeO-50 nanoparticles does occur, but Gal-50 are taken up to a greater extent. At least 10 nanoparticles were associated with each hepatocyte within 30 seconds of their addition to the hepatocyte suspension (data not shown). This result is not unreasonable considering that ASGPr clustering has been observed within 15 seconds of ligand introduction,[14] approximately 50% of ASGPr-ligand complexes are internalized within 3 minutes[12,15] and that at saturation, each hepatocyte can take up $5*10^6$ ligands by ASGPr per hour.[7]

Following pinocytic uptake by hepatocytes *in vivo*, vesicles follow one of three distinct paths.[16] About 80% of pinocytosis material is rapidly exchanged with extracellular fluid, about 18% is processed deeper into the cell and about 2% is secreted into bile. The fraction of internalized fluid that is regurgitated back into plasma does so with $t_{1/2}$ about 1-2 minutes in hepatocytes. This $t_{1/2}$ is considerably shorter than is seen in macrophages, fibroblasts or adipocytes. Based on these uptake results, it is estimated that hepatocytes pinocytose the equivalent of 20% or more of their volume and at least 5 times their plasma membrane surface area each hour.[16] This high recycle rate of pinocytosed materials has also been confirmed with suspended rate hepatocytes,[17] and the shape of the MeO-50 uptake curve in Figure 5.1a can be explained by this mechanism.[18] For the first 30-60 seconds of hepatocyte exposure to MeO-50 nanoparticles, uptake is proceeding quickly without significant nanoparticle release back into the extracellular fluid. However, an average pinosome recycling time of about 1-2 minutes means that increasing amounts of pinocytosed material will be released after about 60 seconds until steady-state conditions are reached after about 200 seconds. Under steady-state conditions, 80% of all pinocytosed material will be rapidly recycled while 20% will be retained within the cell and contribute to ongoing increases in cell fluorescence. As such, an initial region of linearly increasing uptake is expected until about 30-60 seconds, at which time a transition will occur until another linear uptake region with a shallower slope is observed after about 200 seconds. The MeO-50 kinetic uptake curve shown in Figure 5.1a matches this description.

The shape of the Gal-50 uptake curve is similar to that of MeO-50 (Figure 5.1a). This can be understood if the primary mechanism of uptake of Gal-50 *in vitro* is also pinocytosis, but with additional ASGPr-mediated uptake as well. Suspended rat hepatocytes have been shown[17] to uptake transferrin primarily by pinocytosis, despite the presence of a transferrin receptor on their cell surface. Nearly 80% of transferrin uptake was attributed to pinocytosis, with the remainder coming through receptor-mediated endocytosis. The half-time for internalization via the ASGPr is about 180 seconds,[19] with an average time to recycle to the cell surface of about 4 minutes.[6] Because of the similarity of these two uptake processes and the suggested dominant role of pinocytosis on uptake, it can be expected that Gal-50 will be internalized to a greater extent than MeO-50, but that the shape of the two kinetic uptake curves will be similar. In the presence of Cu^{2+} and Zn^{2+} ions, uptake of Gal-50 and MeO-50 are indistinguishable (see Appendix D), suggesting that the difference in uptake between the two nanoparticles is ASGPr-mediated.

5.3.2 Optimization of Experimental Conditions for *In Vivo* Experiments

To allow direct comparison between all *in vivo* experiments, a set of experimental conditions was identified that maximizes hepatic uptake following injection of nanoparticles. For this purpose, Gal-50 nanoparticles were utilized. The percentage of the injected dose in the liver was determined by homogenizing the livers of two mice per set of experimental conditions and extracting the fluorescent dye in chloroform.

Nanoparticles can be administered in a variety of ways to mice. Since hepatic uptake is desired, direct injection into the liver can be accomplished via portal vein or inferior vena cava. While portal vein injections are possible in humans, unnecessary surgical procedures are preferentially avoided. Therefore, the nanoparticles will be introduced into systemic circulation and will pass through the liver with the general blood flow. Tail-vein injection in mice is the most convenient method of introducing materials into the mouse circulation and will be used in all *in vivo* experiments. Injection of large volumes relative to the circulating blood volume of the mouse have been found to result in transiently increased cell membrane permeability[20] that could obscure the effects of nanoparticle-size galactose presence. Therefore, low-pressure tail-vein injections of nanoparticles (100 μL per 20 g mouse) will be employed in all *in vivo* experiments.

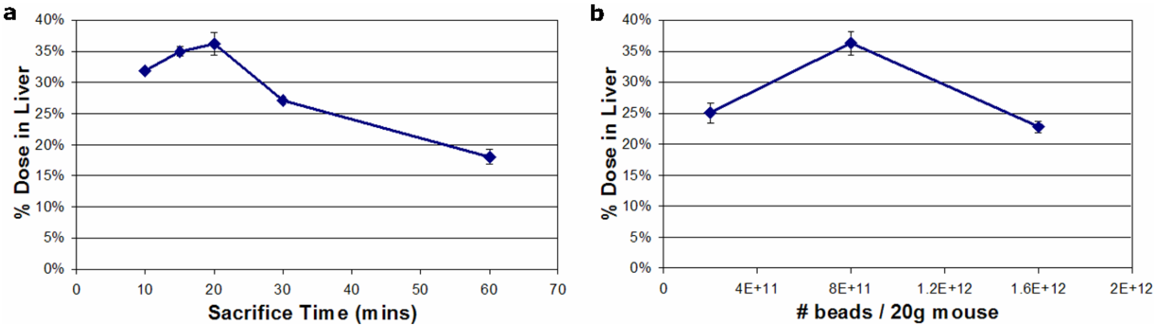

Figure 5.2. Optimization of experimental conditions for *in vivo* experiments by assaying total fluorescence of mouse liver following homogenization of liver and extraction of fluorophore. a) Determination of optimal time between tail-vein injection of nanoparticles and liver removal. $8*10^{11}$ Gal-50 nanoparticles were injected via tail-vein per 20 g mouse, two mice per group, and sacrificed at the time shown. b) Determination of optimal bead dose. Mice received tail-vein injections of Gal-50 nanoparticles and were sacrificed 20 minutes post-injection.

As shown in Figure 5.2, Gal-50 accumulates in the liver up to about 20 minutes, after which time its concentration decreases. The effect of the Gal-50 dose on liver uptake was also investigated, over a dose range that is reasonable for nonviral gene delivery particles. Based on the results of these liver uptake experiments, it was determined that $8*10^{11}$ beads in 100 μL saline per 20 g mouse would be administered via tail-vein injection, with liver removal 20 minutes post-injection.

5.3.3 Bulk Liver Uptake of Nanoparticles

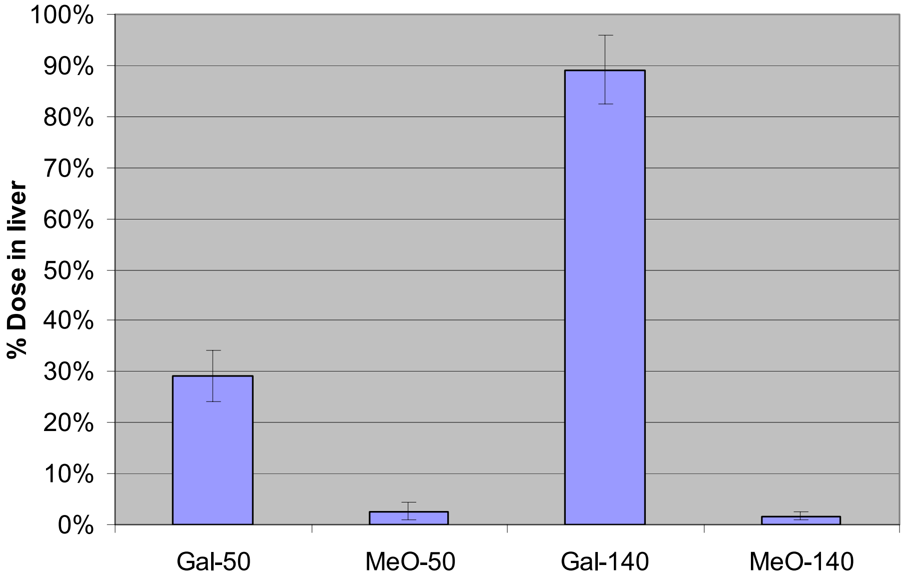

Figure 5.3. Overall uptake of nanoparticles into hepatic tissue. Results are shown as mean ± standard deviation of three mice per group.

As in the previous experiment, the uptake of nanoparticles into liver tissue can be determined by homogenizing the liver and extracting the fluorescent dye. The comparison of bulk liver uptake of each nanoparticle is shown in Figure 5.3. It is apparent that galactosylated nanoparticles are taken up to a much greater extent than are non-galactosylated nanoparticles, which is as expected given the unique presence of galactose receptors in the liver on hepatocytes and Kupffer cells. In particular, nearly the entire dose of Gal-140 is found in the liver, as compared to about one-third of the Gal-50 dose. Concentrations of both MeO-50 and MeO-140 in the liver are quite low. *In vitro*, neither of the two types of 140 nm beads were internalized to a significant extent by hepatocytes, but it is clear that Gal-140 nanoparticles are taken up by the liver *in vivo*. As shown in the following sections, Kupffer cells are primarily responsible for Gal-140 uptake *in vivo*.

5.3.4 TEM Imaging Following Tail-Vein Injection of Nanoparticles

Bulk liver uptake experiments indicated significant differences in the uptake of targeted and nontargeted nanoparticles, but gave no indication of the hepatic distributions. TEM analysis of liver cross-sections following tail-vein injection of nanoparticles provided information on hepatic distribution and intracellular trafficking of the nanoparticles. All images are representative of the overall hepatic distribution for each type of nanoparticle.

5.3.4.1 Hepatic Distribution of 140 nm Nanoparticles

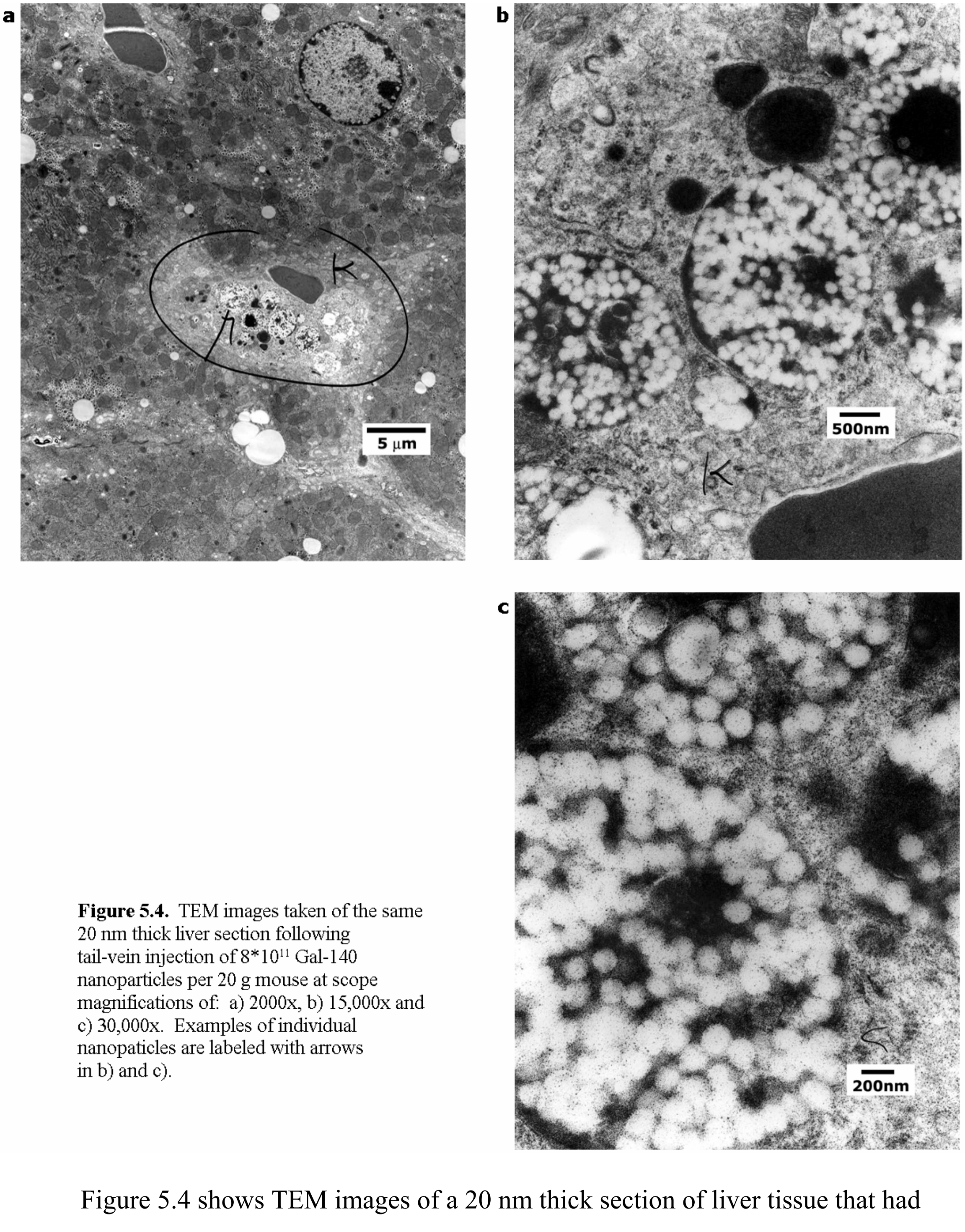

Figure 5.4. TEM images taken of the same 20 nm thick liver section following tail-vein injection of 8*10^{11} Gal-140 nanoparticles per 20 g mouse at scope magnifications of: a) 2000x, b) 15,000x and c) 30,000x. Examples of individual nanopaticles are labeled with arrows in b) and c).

Figure 5.4 shows TEM images of a 20 nm thick section of liver tissue that had been exposed to Gal-140 by tail-vein injection of these nanoparticles. The image in Figure 5.4a shows six hepatocytes surrounding a single Kupffer cell (marked ‘K’).

Hepatocytes are polyhedral cells with 8 or more surfaces and regular, round nuclei that represent about 60% of the cells in the liver but almost 80% of hepatic volume since they are the largest of the cells. Kupffer cells are hepatic macrophages that have irregular nuclei and generally are located in the lumen of hepatic sinusoids adjacent to hepatocytes. Kupffer cells are in direct contact with the bloodstream and represent about 10% of the cells in the liver.

Though isolated examples of Gal-140 in hepatocytes could be found (images not shown), only a few beads are found per cell in those cases, while nearly all Kupffer cells contain a large number of internalized beads as shown in Figure 5.4b. This image clearly demonstrates Kupffer cell uptake of Gal-140, with hundreds of nanoparticles in each of the large phagocytic compartments (Figure 5.4c). At $8*10^{11}$ nanoparticles injected per 20 g mouse, approximately 50,000 nanoparticles are being injected per Kupffer cell in the liver. Since the Kupffer cell galactose-particle receptor has been documented to endocytose as many as 4200 galactosylated particles per cell per minute,[21] the large number of nanoparticles observed per cell is reasonable.

Nanoparticle aggregation is not observed in Figure 5.4c, despite extremely concentrated conditions in the confines of phagocytic compartments. This provides additional evidence that the nanoparticles are stable and do not aggregate or fall apart either in serum or intracellularly, confirming the results of *in vitro* stability assays. The size stability *in vivo* allows the direct correlation of nanoparticle size with uptake results.

Unlike Gal-140, MeO-140 nanoparticles are not taken up to a great extent by any hepatic cells. In fact, most cells did not contain any MeO-140 beads, and few examples could be found of aggregates of MeO-140. However, of the cells that contained nanoparticles, MeO-140 were primarily internalized by Kupffer cells (images not shown).

5.3.4.2 Hepatic Distribution of 50 nm Nanoparticles

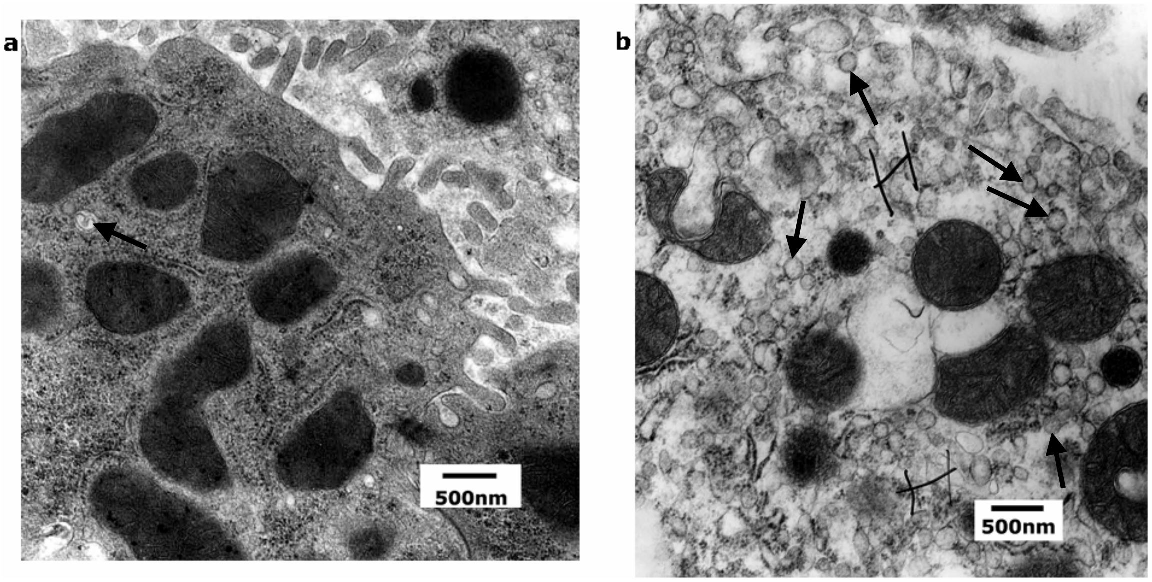

Figure 5.5. TEM images of hepatocytes following tail-vein injection of a) MeO-50 and b) Gal-50 nanoparticles, $8*10^{11}$ per 20 g mouse. Examples of individual vesicles are labeled with arrows.

TEM images of liver sections following exposure to 50 nm nanoaparticles were quite different than those exposed to Gal-140. Neither MeO-50 or Gal-50 were found concentrated in Kupffer cells, though liver that was exposed to Gal-50 had an unusually large number of 100-200 nm vesicles throughout the cytoplasm of most hepatocytes, as shown in Figure 5.5b. As compared to hepatocytes from mice that received tail-vein injection of MeO-50 (Figure 5.5a), which contain occasional vesicles in the cytosol, hepatocytes exposed to Gal-50 contain many hundreds of clearly defined vesicles.

The result that Gal-140 are much more concentrated in Kupffer cells than are Gal-50 is consistent with literature reports that Kupffer cells tend to uptake 80 nm particles much more slowly than they internalize 500 nm particles.[3] However, identification of individual nanoparticles in the hepatocyte vesicles is not as clear in the case of Gal-50 as it was for Gal-140. It is therefore critical to demonstrate that vesicles as shown in Figure 5.5b do in fact contain nanoparticles.

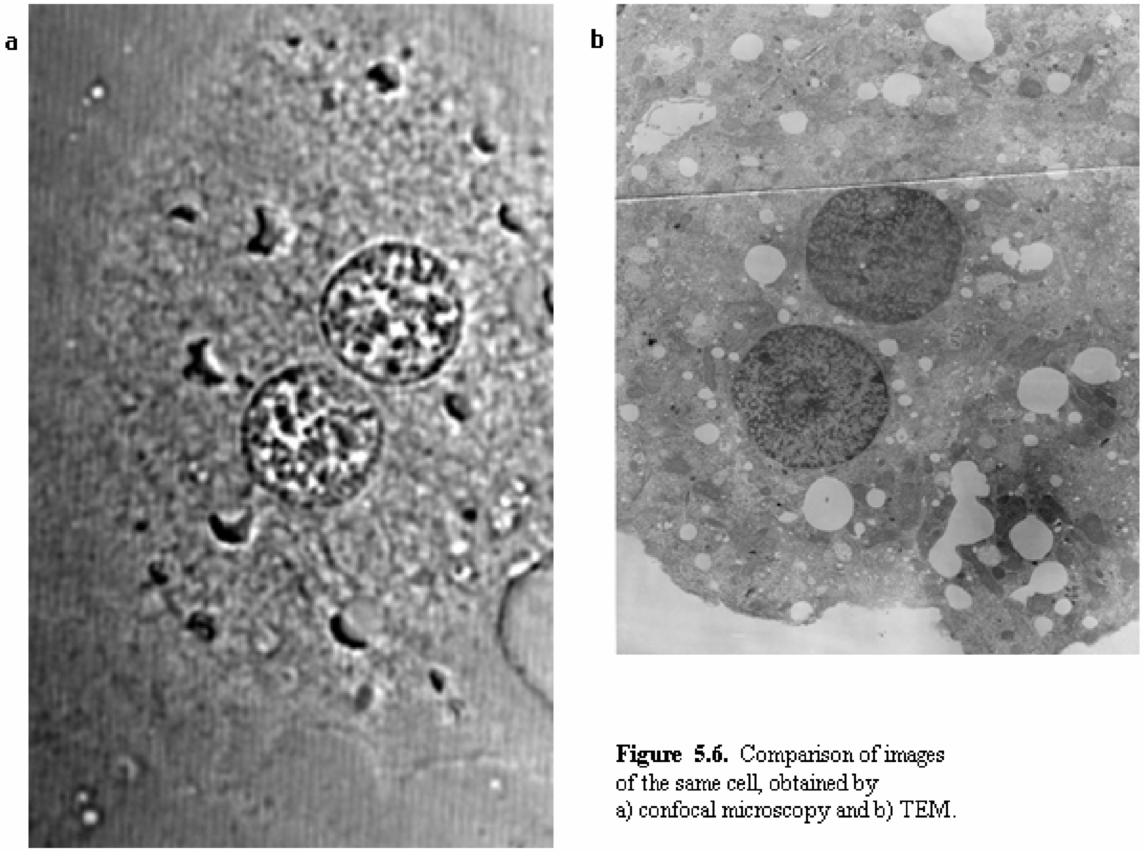

Figure 5.6. Comparison of images of the same cell, obtained by a) confocal microscopy and b) TEM.

To confirm that the vesicles shown in Figure 5.5b contain nanoparticles, we endeavored to image the same cell by both fluorescence and TEM. By carefully marking and photographically documenting the cell of interest, we were able to identify the same cell following workup for TEM. In Figure 5.6, the capability of the technique is demonstrated by imaging the same cell with light microscopy and TEM. The nuclei and overall cell membrane shape, as well as relation to adjacent cells (not visible in Figure 5.6), confirm that the same cell may be identified and imaged on separate microscopes on separate days. Any slight differences in cell morphology may be attributed to the fact that the entire thickness of the cell is photographed with the light microscope, while only a thin section of about 20 nm is imaged by TEM.

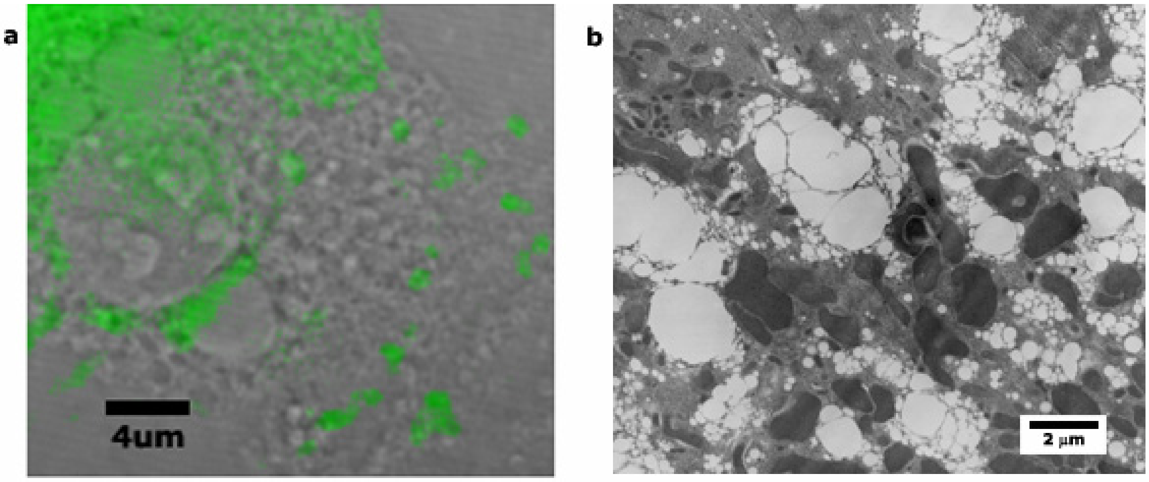

Figure 5.7. Imaging of a hepatocyte, 24-hours post isolation that had been exposed to Gal-50 nanoparticles. Comparison of a) light and fluorescence images and b) TEM image of the green perinuclear region on the top left side of (a).

By comparing green regions seen by fluorescence microscopy of a plated hepatocyte *in vitro* with vesicle-containing regions seen by TEM, it was confirmed that the vesicles in hepatocytes exposed to Gal-50 *in vivo* contain nanoparticles. In Figure 5.7a, the majority of a hepatocyte is seen by fluorescence and light microscopy. This plated hepatocyte was exposed to Gal-50 *in vitro* before being fixed with glutaraldehyde and imaged by confocal microscopy. Heavy-metal staining of the cell and embedding in Epon resin allowed TEM to be taken of the same cell. Since all nanoparticles used in these experiments have FITC embedded in their polystyrene core, they show up as green in the fluorescence image (Figure 5.7a). From this image it is apparent that the majority of Gal-50 beads are in the perinuclear region of the cell. When perinuclear regions of the cell are magnified by TEM (Figure 5.7b), an unnaturally large number of vesicles are seen. There are few vesicles in regions of the hepatocyte that do not show up green by fluorescence, so it is apparent that the green fluorescence originates from the large number of intracellular vesicles. Isolated clusters of vesicles on TEM show up as bright spots by fluorescence, while clusters in close proximity, as shown in Figure 5.7b, show up as diffuse green regions by fluorescence. Analogous to the situation seen *in vivo* following injection of Gal-50, individual nanoparticles cannot be easily identified inside vesicles, but green fluorescence is clearly originating from these vesicles. We therefore conclude that Gal-50 nanoparticles are trapped within the vesicles seen by TEM.

Hepatocytes and Kuppfer cells are not the only hepatic cells capable of internalizing nanoparticles. Under the appropriate conditions, both hepatic stellate cells (HSC) and liver sinusoidal endothelial cells (LSEC) display phagocytic behavior. Following hepatic injury, hepatic stellate cells (HSC) differentiate into an activated phenotype that is capable of taking up 1 μm carboxylate-modified latex particles.[22] Despite liver enzyme assays indicating no toxicity associated with the nanoparticles used in this study, and hence no reason for HSC activation, HSC uptake of nanoparticles was considered and excluded based on TEM and FACS results (FACS data discussed in Appendix C). We also must consider possible uptake by LSEC. LSEC have been shown to nonspecifically internalize a number nanoparticles, including lecithin-coated 240 nm polystyrene beads,[23] uncoated 240 nm and 330-800 nm polystyrene beads,[24] and 12 nm iron oxide nanoparticles.[25] Furthermore, LSEC are indicated in the efficient ingestion and rapid degradation of naked pDNA *in vivo* and *in vitro*.[26] Despite intense scrutiny, no evidence could be found of LSEC association or internalization of the PEGylated nanoparticles employed in this study.

By TEM, we have thus confirmed a significant difference in hepatic distribution and uptake of 50 nm and 140 nm nanoparticles that present either galactose or methoxy moieties on their surface. Although TEM provides a very detailed view of intracellular trafficking, it is limited by the small area that can be examined at a time and by lack of scalability, thus preventing conclusions to be drawn concerning distribution of the nanoparticles across the area of the liver.

5.3.5 Immunohistochemistry Following Tail-Vein Injection of Nanoparticles

To provide a more general view of the liver, an immunohistochemical staining (IHC) procedure was developed. This technique is scalable in that processing may be done to multiple slides simultaneously. Twenty minutes after nanoparticles were injected via tail-vein into mice, the liver was embedded in OCT blocks and stored in 2-methylbutanol on dry ice. 12 μm thick liver sections were cut from the OCT blocks, excess OCT was dissolved away and endogenous biotin activity was blocked. ASGPr was then stained red through a three-component antibody system. Goat anti-ASGPr1 was used as the primary antibody to provide a target for attachment of a donkey anti-goat IgG-biotin antibody. Since exogenous biotin was already blocked, incubation with QDot655-Streptavidin and subsequent washes permitted specific visualization of the

ASGPr receptor in the red fluorescence channel. Blocking of exogenous biotin was critical to minimize nonspecific binding of QDot655-Streptavidin to liver tissue. Finally, slides were stained with DAPI-containing VectaShield mounting media, providing blue staining to nucleic acids in cell nuclei.

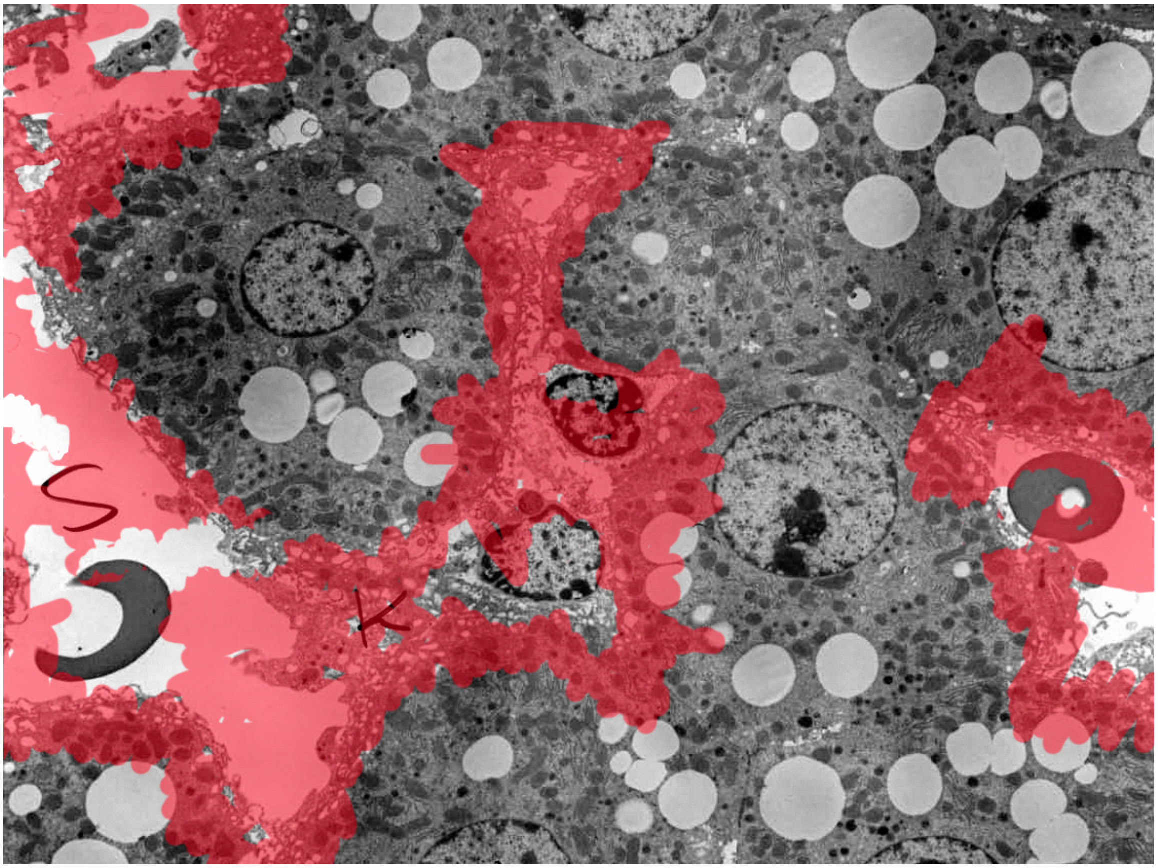

Figure 5.8. Illustration of the staining that results from the immunohistochemical staining of the hepatic asialoglycoprotein receptor (ASGPr).

In Figure 5.8, an example of the ASGPr staining pattern is drawn on a TEM image of normal mouse liver. ASGPr is expressed primarily on the hepatocytic basal and lateral membranes, which are directed toward the perisinusoidal and pericellular spaces and make up about 75% of the hepatocyte circumference. The density of ASGPr on these surfaces is 7- to 14-fold higher than on the apical surfaces.[27,28] We would therefore expect to see staining around the perimeter of sinusoids and around Kupffer cells, but hepatocyte-hepatocyte junctions should remain largely unstained. However, sections used for IHC are 12 μm thick, or about 300 times thicker than sections used for TEM, so the three-dimensionality of the sinusoids must also be considered. Liver sinusoids have an average diameter of about 7.3 μm,[29] so it is likely that hepatocyte membranes located just above or below sinusoids will be partially included in the 12 μm thick IHC section. We would therefore expect sinusoidal endothelial cells to be included in the red-stained regions. Similarly, since Kupffer cells tend to border sinusoids and sinusoid-facing perimeters of hepatocytes, it is to be expected that many Kupffer cells will also be stained red.

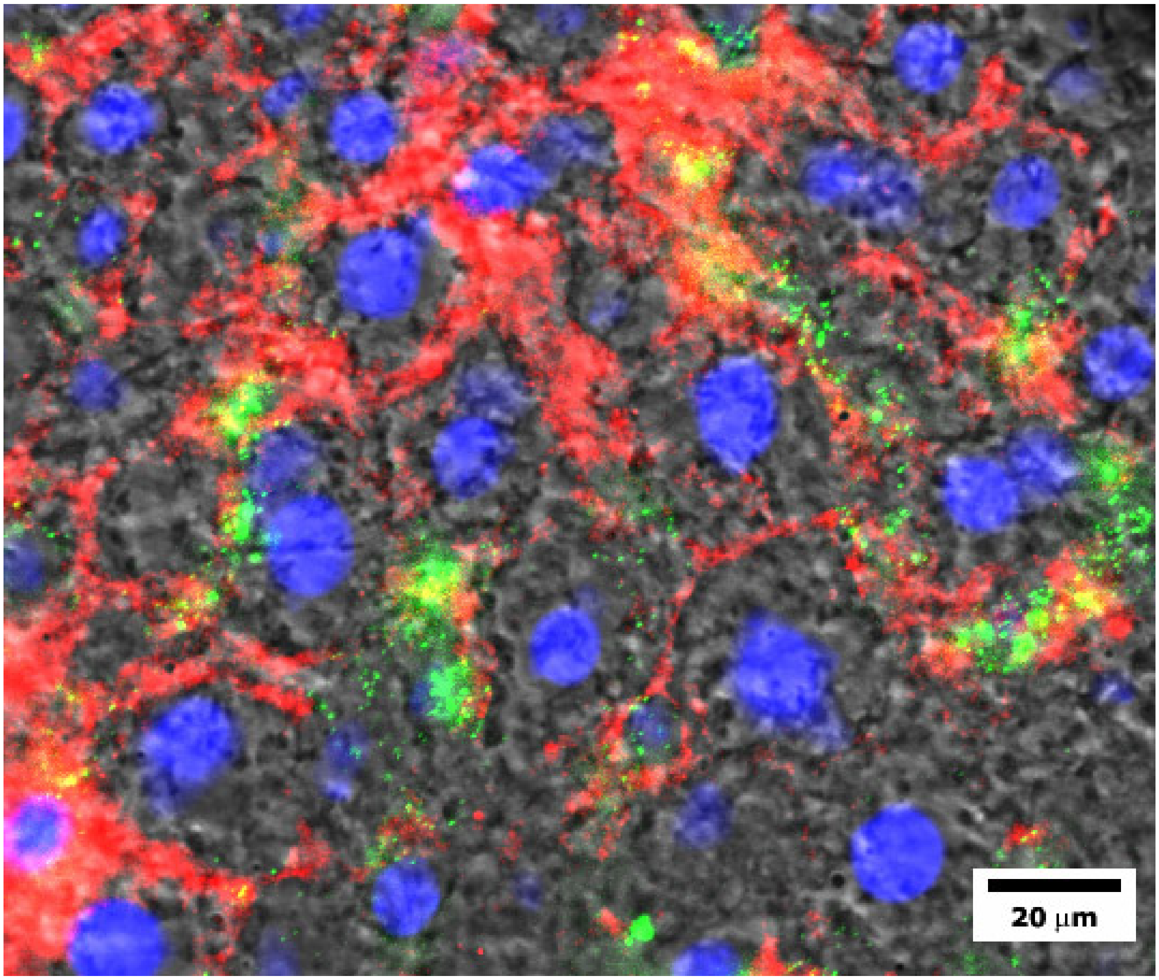

Figure 5.9. Immunohistochemistry image of 12 µm-thick section of mouse liver following tail-vein injection of $8*10^{11}$ MeO-140 nanoparticles. ASGPr is stained red, nuclei are blue and nanoparticles are green/yellow.

A representative immunohistochemistry image obtained after tail-vein injection of MeO-140 nanoparticles into mice is shown in Figure 5.9. In this image, a sinusoid is seen running from the top center of the image towards the bottom right corner before wrapping around a pair of hepatocyte nuclei and returning toward the top-center. Along the length of this sinusoid, a large number of individual MeO-140 beads can be seen. The situation just described is similar to that seen in sinusoids running vertically down the left side and center of the image, in which the nanoparticles do not appear to be aggregated. Few examples of MeO-140 aggregation could be found, indicating that these beads are largely present in hepatic sinusoids and are not internalized to any great extent in hepatic cells. This situation is similar to that observed for MeO-50 beads (not shown). No difference in nanoparticle distribution or density was observed between regions near the portal vein inlet to the liver and regions near the hepatic vein outlet.

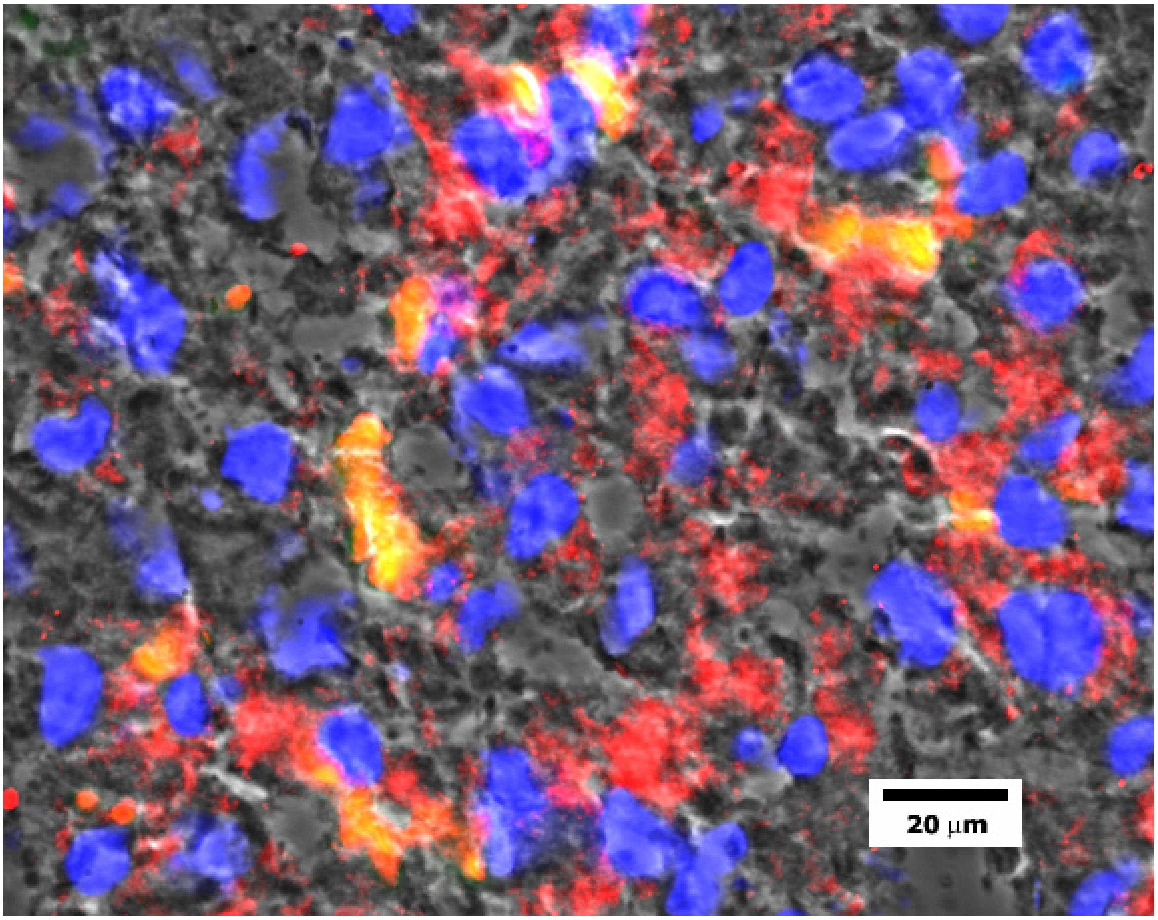

Figure 5.10. Immunohistochemistry image of 12 μm-thick section of mouse liver following tail-vein injection of $8*10^{11}$ Gal-140 nanoparticles. ASGPr is stained red, nuclei are blue and nanoparticles are green/yellow.

The immunohistochemistry image obtained following Gal-140 injection is much different. In the image shown in Figure 5.10, large aggregates of nanoparticles are observed. These aggregates show up as yellow due to bright green overlaying red. While both MeO-140 and Gal-140 are shown to primarily overlay sinusoidal or Kupffer cell regions of the liver, the massively aggregated state of Gal-140 point to uptake by either Kupffer or sinusoidal endothelial cells since no mechanism exists for particle aggregation in the sinusoids. By TEM, no evidence of nanoparticle uptake into endothelial cells could be found, so we are left to conclude that the massive aggregates of Gal-140 nanoparticles are resident in Kupffer cells. This result supports the conclusion drawn from TEM studies. Immunohistochemistry provides the ability to image a 1-2 cm cross-section of liver, permitting the distribution of beads to be seen across the liver from portal-vein inlet to hepatic-vein outlet. While both sized methoxy-beads are seen in sinusoids in similar concentrations across the liver, a somewhat higher concentration of Gal-140 beads are observed near the portal-vein inlet to the liver. This observation is consistent with the observation that Gal-140 are taken up into cells while MeO-50 and MeO-140 remain largely in the sinusoids.

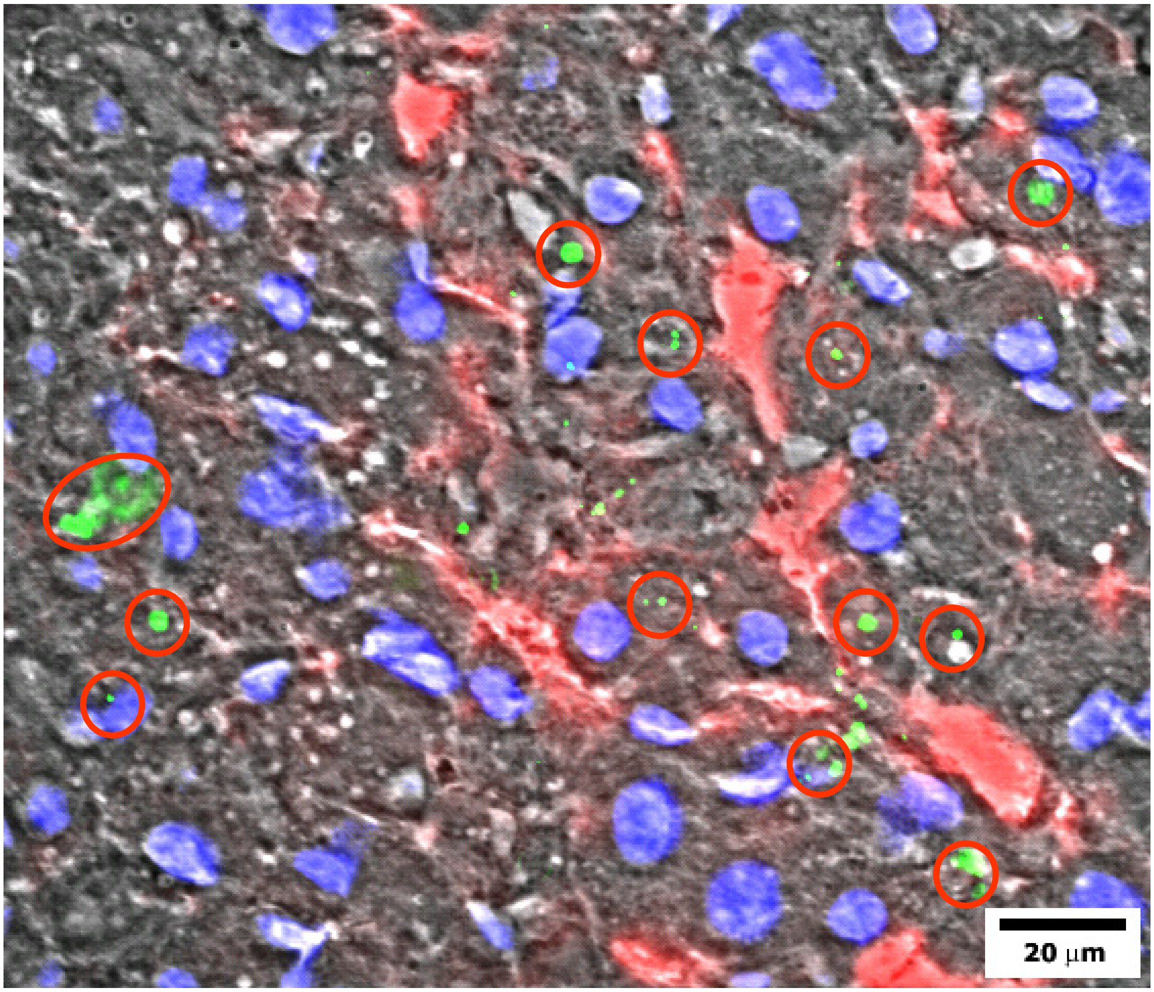

Figure 5.11. Immunohistochemistry image of 12 μm-thick section of mouse liver following tail-vein injection of $8*10^{11}$ Gal-50 nanoparticles. ASGPr is stained red, nuclei are blue and nanoparticles are green/yellow.

In agreement with the TEM observations presented, immunohistochemistry on liver tissue from mice that received tail-vein injections of Gal-50 nanoparticles shows that Gal-50 are primarily internalized by hepatocytes (Figure 5.11). In this image, a pair of sinusoids is seen running from the bottom right corner of the image diagonally towards the upper left corner. Unlike the images taken following injection of any of the other beads, few Gal-50 beads are seen to overlap red-stained regions of liver. The majority of nanoparticles in this image have been internalized by hepatocytes, including all nanoparticles surrounded by red circles. A few Gal-50 nanoparticles may be in sinusoidal spaces or in Kupffer cells, located near the center of the image and towards the bottom right, where the green fluorescence overlays the red ASPGr staining, but the majority of Gal-50 are internalized by hepatocytes.

5.4 Conclusions

In this work, I studied the hepatocyte uptake *in vitro* and hepatic distribution *in vivo* of four slightly anionic, PEGylated-polystyrene nanoparticles. Slightly anionic surface charges are utilized to minimize nonspecific proteoglycan-mediated uptake or interaction with anionic cell surface membranes. In freshly isolated hepatocytes, Gal-50 nanoparticles are taken up to a greater extent than are MeO-50, but both 50 nm beads are taken up to a much greater extent than are either 140 nm nanoparticles. However, about 90% of the *in vivo* dose of Gal-140 nanoparticles is found within the liver 20 minutes after tail-vein injection. TEM and immunohistochemistry images confirm that Gal-140 are primarily internalized by Kupffer cells, though isolated examples of a few Gal-140 in hepatocytes can also be found. On the other hand, Gal-50 nanoparticles are overwhelmingly found in vesicles throughout the cytoplasm of hepatocytes, with only isolated examples of Kupffer cell uptake. Despite similar surface charge and ligand density, 50 nm nanoparticles are primarily found in hepatocytes while 140 nm nanoparticles are primarily seen in Kupffer cells. It is therefore clear that slightly anionic, galactose-PEGylated nanoparticles should be about 50 nm in diameter to preferentially target hepatocytes while they should be about 140 nm in diameter to selectively target Kupffer cells.

5.5 Acknowledgements

I am grateful to a number of people for assisting with this work. Dr. Siwen Hu graciously donated her time and expertise, showing me the tricks and techniques of immunohistochemistry and excising livers from countless mice. Dr. Samuel French acquired the TEM images of liver sections shown in this chapter, and I would like to thank him for helpful discussions analyzing the images. Dr. Timothy Triche provided encouragement along the way as well as expert analysis of the immunohistochemistry images. Dr. Hide Tsukamoto generously offered the services of his lab to isolate non-parenchymal liver cells. Dr. Rochelle Diamond went out of her way to assist with my *in vitro* FACS experiments. And I thank George McNamara of the CHLARI Image Core for advice and assistance in acquiring images following immunhistochemical staining.

5.6 References

1. Kawasaki, T.; Ii, M.; Kozutsumi, Y.; Yamashina, I., Isolation and characterization of a receptor lectin specific for galactose/N-acetylgalactosamine from macrophages. *Carbohydrate Research* **1986,** 151, 197-206.

2. Rensen, P. C. N.; Sliedregt, L.; Ferns, A.; Kieviet, E.; van Rossenberg, S. M. W.; van Leeuwen, S. H.; van Berkel, T. J. C.; Biessen, E. A. L., Determination of the upper size limit for uptake and processing of ligands by the asialoglycoprotein receptor on hepatocytes *in vitro* and *in vivo*. *Journal of Biological Chemistry* **2001,** 276, (40), 37577-37584.

3. Rahman, Y. E.; Cerny, E. A.; Patel, K. R.; Lau, E. H.; Wright, B. J., Differential uptake of liposomes varying in size and lipid-composition by parenchymal and Kupffer cells of mouse-liver. *Life Sciences* **1982,** 31, (19), 2061-2071.

4. Castaneda, F.; Kinne, R. K. H., Cytotoxicity of millimolar concentrations of ethanol on HepG2 human tumor cell line compared to normal rat hepatocytes *in vitro*. *Journal of Cancer Research and Clinical Oncology* **2000,** 126, (9), 503-510.

5. Tanaka, T.; Fujishima, Y.; Kaneo, Y., Receptor mediated endocytosis and cytotoxicity of transferrin-mitomycin c conjugate in the HepG2 cell and primary cultured rat hepatocyte. *Biological and Pharmaceutical Bulletin* **2001,** 24, (3), 268-273.

6. Schwartz, A. L.; Fridovich, S. E.; Lodish, H. F., Kinetics of internalization and recycling of the asialoglycoprotein receptor in a hepatoma-cell line. *Journal of Biological Chemistry* **1982,** 257, (8), 4230-4237.

7. Warren, R.; Doyle, D., Turnover of the surface-proteins and the receptor for serum asialoglycoproteins in primary cultures of rat hepatocytes. *Journal of Biological Chemistry* **1981,** 256, (3), 1346-1355.

8. Stoorvogel, W.; Schwartz, A. L.; Strous, G. J.; Fallon, R. J., A pool of intracellular phosphorylated asialoglycoprotein receptors which is not involved in endocytosis. *Journal of Biological Chemistry* **1991,** 266, (9), 5438-5444.

9. Lu, S. C.; Ge, J. L.; Huang, H. Y.; Kuhlenkamp, J.; Kaplowitz, N., Thiol-disulfide effects on hepatic glutathione transport–studies in cultured rat hepatocytes and perfused livers. *Journal of Clinical Investigation* **1993,** 92, (3), 1188-1197.

10. McAbee, D. D.; Jiang, X., Copper and zinc ions differentially block asialoglycoprotein receptor-mediated endocytosis in isolated rat hepatocytes. *Journal of Biological Chemistry* **1999,** 274, (21), 14750-14758.

11. Siekevitz, P.; Palade, G. E., A cytochemical study on the pancreas of the guinea pig. 5. *In vivo* incorporation of leucine-C-14 into the chymotrypsinogen of various cell fractions. *Journal of Biophysical and Biochemical Cytology* **1960,** 7, (4), 619-630.

12. Weigel, P. H.; Oka, J. A., The large intracellular pool of asialoglycoprotein receptors functions during the endocytosis of asialoglycoproteins by isolated rat hepatocytes. *Journal of Biological Chemistry* **1983,** 258, (8), 5095-5102.

13. Pricer, W. E.; Ashwell, G., Subcellular-distribution of a mammalian hepatic binding-protein specific for asialoglycoproteins. *Journal of Biological Chemistry* **1976,** 251, (23), 7539-7544.

14. Wall, D. A.; Wilson, G.; Hubbard, A. L., The galactose-specific recognition system of mammalian liver–The route of ligand internalization in rat hepatocytes. *Cell* **1980,** 21, (1), 79-93.

15. Wolkoff, A. W.; Klausner, R. D.; Ashwell, G.; Harford, J., Intracellular segregation of asialoglycoproteins and their receptor–A prelysosomal event subsequent to dissociation of the ligand-receptor complex. *Journal of Cell Biology* **1984,** 98, (2), 375-381.

16. Scharschmidt, B. F.; Lake, J. R.; Renner, E. L.; Licko, V.; Vandyke, R. W., Fluid phase endocytosis by cultured rat hepatocytes and perfused-rat-liver–Implications for plasma-membrane turnover and vesicular trafficking of fluid phase markers. *Proceedings*

of the National Academy of Sciences of the United States of America **1986,** 83, (24), 9488-9492.

17. Rudolph, J. R.; Regoeczi, E., Relationship between pinocytic rate and uptake of transferrin by suspended rat hepatocytes. *Biology of Metals* **1991,** 4, (3), 166-172.

18. Kjeken, R.; Mousavi, S. A.; Brech, A.; Gjoen, T.; Berg, T., Fluid phase endocytosis of [I-125]iodixanol in rat liver parenchymal, endothelial and Kupffer cells. *Cell and Tissue Research* **2001,** 304, (2), 221-230.

19. Tolleshaug, H.; Berg, T.; Nilsson, M.; Norum, K. R., Uptake and degradation of I-125-labeled asialofetuin by isolated rat hepatocytes. *Biochimica et Biophysica Acta* **1977,** 499, (1), 73-84.

20. Kobayashi, N.; Nishikawa, M.; Hirata, K.; Takakura, Y., Hyrodynamics-based procedure involves transient hyperpermeability in the hepatic cellular membrane: implication of a nonspecific process in efficient intracellular gene delivery. *Journal of Gene Medicine* **2004,** 6, (5), 584-592.

21. Teradaira, R.; Kolbbachofen, V.; Schlepperschafer, J.; Kolb, H., Galactose-particle receptor on liver macrophages–Quantitation of particle uptake. *Biochimica et Biophysica Acta* **1983,** 759, (3), 306-310.

22. Vinas, O.; Bataller, R.; Sancho-Bru, P.; Gines, P.; Berenguer, C.; Enrich, C.; Nicolas, J. M.; Ercilla, G.; Gallart, T.; Vives, J.; Arroyo, V.; Rodes, J., Human hepatic stellate cells show features of antigen-presenting cells and stimulate lymphocyte proliferation. *Hepatology* **2003,** 38, (4), 919-929.

23. Kanai, M.; Murata, Y.; Mabuchi, Y.; Kawahashi, N.; Tanaka, M.; Ogawa, T.; Doi, M.; Soji, T.; Herbert, D. C., *In vivo* uptake of lecithin-coated polystyrene beads by

rat hepatocytes and sinusoidal endothelial cells. *Anatomical Record* **1996,** 244, (2), 175-181.

24. Dan, C.; Wake, K., Modes of endocytosis of latex-particles in sinusoidal endothelial and Kupffer cells of normal and perfused rat-liver. *Experimental Cell Research* **1985,** 158, (1), 75-85.

25. Briley-Saebo, K.; Bjornerud, A.; Grant, D.; Ahlstrom, H.; Berg, T.; Kindberg, G. M., Hepatic cellular distribution and degradation of iron oxide nanoparticles following single intravenous injection in rats: implications for magnetic resonance imaging. *Cell and Tissue Research* **2004,** 316, (3), 315-323.

26. Hisazumi, J.; Kobayashi, N.; Nishikawa, M.; Takakura, Y., Significant role of liver sinusoidal endothelial cells in hepatic uptake and degradation of naked plasmid DNA after intravenous injection. *Pharmaceutical Research* **2004,** 21, (7), 1223-1228.

27. Hubbard, A. L.; Wall, D. A.; Ma, A., Isolation of rat hepatocyte plasma-membranes. 1. Presence of the 3 major domains. *Journal of Cell Biology* **1983,** 96, (1), 217-229.

28. Matsuura, S.; Nakada, H.; Sawamura, T.; Tashiro, Y., Distribution of an asialoglycoprotein receptor on rat hepatocyte cell-surface. *Journal of Cell Biology* **1982,** 95, (3), 864-875.

29. Hess, F. A.; Weibel, E. R.; Preisig, R., Morphometry of dog liver–Normal base-line data. *Virchows Archiv Abteilung B Zellpathologie* **1973,** 12, (4), 303-317.

CHAPTER SIX

OVERALL CONCLUSIONS, RECOMMENDATIONS AND FUTURE CONSIDERATIONS

6.1 Overall Conclusions and Recomendations

Based on the results of work presented in this report, it is apparent that the chemical structure and physicochemical properties of gene delivery particles affect their *in vitro* and *in vivo* performance. The cyclodextrin-based gene delivery systems developed in our laboratory are amenable to tailoring of particle size, surface charge, and ligand type and density. Through use of a nanoparticle-based model delivery system, I have now identified a set of parameters that enables the hepatocyte-specific targeting of particles *in vivo*. Specifically, PEGylated 50 nm nanoparticles with 25 *p*mol/cm^2 galactose surface density and slightly anionic surface potentials are found to preferentially be internalized by hepatocytes following tail-vein injection in mice. Given the difficulty of non-viral gene delivery to hepatocytes, gene delivery particles should now be synthesized with these properties and their *in vivo* hepatocyte-targeting assayed. Mean particle diameters of about 50 nm are attainable by formulating the particles in the presence of adamantane-PEG.[1] Galactose surface density can be controlled by varying the ratio of lactose-adamantane-PEG to methoxy-adamantane-PEG during the formulation. The surface charge of the particles can be controlled by incorporation of adamantane-PEGs that contain short anionic segments near the adamantane end. In this manner, the optimized set of physicochemical properties identified with the nanoparticle-based model delivery system may be incorporated into next-generation gene delivery particles.

6.2 Future Consideration: Increased Ligand Specificity

In this work, a single galactose ligand was conjugated to the distal end of PEG chains on the surface of polystyrene beads. While this ligand significantly altered hepatic distribution and uptake of the beads, resulting in effective Kupffer cell targeting of 140 nm beads and increased hepatocyte uptake of 50 nm beads, further increases in hepatocyte-specificity may be desirable.

Galactose is known to bind the hepatic asialoglycoprotein receptor with the relatively low affinity of approximately 4×10^{-4} M.[2] Naturally occurring glycopeptides bind much stronger due to branched structure, and this 'cluster effect' can be mimicked by synthetic ligands. The inhibitory power of the ligand can be increased significantly by presenting multiple galactose moieties in close vicinity,[2, 3] with mono-, bi- and triantennary oligosaccharides capable of 50% inhibition at approximately 1 mM, 1 μM and 5 nM, respectively. Stockert provides an excellent review of the asialoglycoprotein receptor,[4] including a proposed distribution of surface receptor binding sites corresponding to the vertices of a triangle with sides of 15, 22 and 25 Å, in which only two terminal galactose residues are required for receptor recognition, with the third providing additional binding energy. Studying binding between a triantennary glycopeptide and the rat ASGPr, Rice *et al.*[5] reached a similar conclusion that the third galactose binds with less affinity than the first two. It has been demonstrated[6] that the spatial inter-galactose distances and the flexibility of the arm connecting galactose residues to the branch points significantly affects binding. More flexible linkers resulted in more potent inhibitors, while spatial distances between galactose residues were best between 15 and 25 Å.[5] A 2000-fold increase in binding affinity was found between a monovalent ligand and an optimized bivalent ligand, and a 50-fold increase from the best bivalent to the best trivalent ligand. Further increase to four or six galactose residues per molecule only increased binding slightly, likely due to an increased local concentration of galactose near the binding sites and interaction with an adjacent receptor. Biessen *et al.*[7] investigated the effect of spacer length between the branch point and terminal sugars and found an at least 2000-fold increase in affinity for the asialoglycoprotein receptor between a trivalent ligand with only a methylene spacer and a trivalent ligand with a 20 Å flexible spacer.

Galactose receptors have been found on the surface of other cells such as Kupffer cells, peritoneal macrophages and tumor cells. Kichler and Schuber[8] synthesized bi- and triantennary galactose ligands with varied distances between galactose residues and found that the triantennary ligand showed significantly higher affinity than the biantennary ligand for both the hepatocyte and peritoneal macrophage galactose receptors. The dissociation constant of hepatocytes was a factor of 4 higher than that of the macrophages, but ideally this difference would be much greater. Though not a primary concern, cluster effects are not observed in galectins,[9] which are typically involved in cell-cell/cell-matrix interactions and growth regulation, suggesting that bi- and trivalent ligands will avoid interfering with these effects.

While increased affinity for the hepatic ASGPr is desirable, a more precise goal may be increased specificity for hepatocytes. In addition to increasing the valency of the ligand, which as discussed above has limited impact on specificity, sugar modifications can affect binding to ASGPr. Terminal nonreducing D-GalNAc residues were found to bind hepatic ASGPr more strongly than galactose,[10, 11] with an estimated 50- to 60-fold enhancement in affinity.[12, 13] Importantly, the peritoneal macrophage asialoglycoprotein binding protein (M-ASGP-BP) was shown to clearly bind Gal stronger than GalNAc,[14] though Fadden *et al*.[15] recently observed that isolated Kupffer cell receptors for glycoproteins displays a slightly higher affinity for GalNAc compared to galactose. It is worth mentioning that many affinity results obtained with isolated receptors generally do not accurately describe binding with intact receptors on the cell surface.[3] In any case, the GalNAc ligand is significantly more selective for hepatocyte targeting than is galactose. Thus, an opportunity for selective targeting presents itself. It was further demonstrated that a comparable tri(*N*-acetyl-lactosamine) ligand showed an affinity increase of about 10^5 over a monovalent ligand for ASGPr, while the same ligand only enhanced binding by M-ASGP-BP by about 2000 times over the monovalent ligand. It might be expected that such a significant difference in enhanced binding could result in improved selectivity of uptake.

Due to the considerable difficulty associated with synthesizing triantennary ligands, it is worth considering the use of mono- or bivalent GalNAc ligands. En route to synthesizing polyantennary structures, an appropriately functionalized monovalent GalNAc must be made. A published scheme[16] allows for the synthesis of a GalNAc ligand appropriate for conjugation to the distal end of PEG for conjugation to nanoparticles or incorporation into the nucleic acid delivery system (Scheme 6.1).

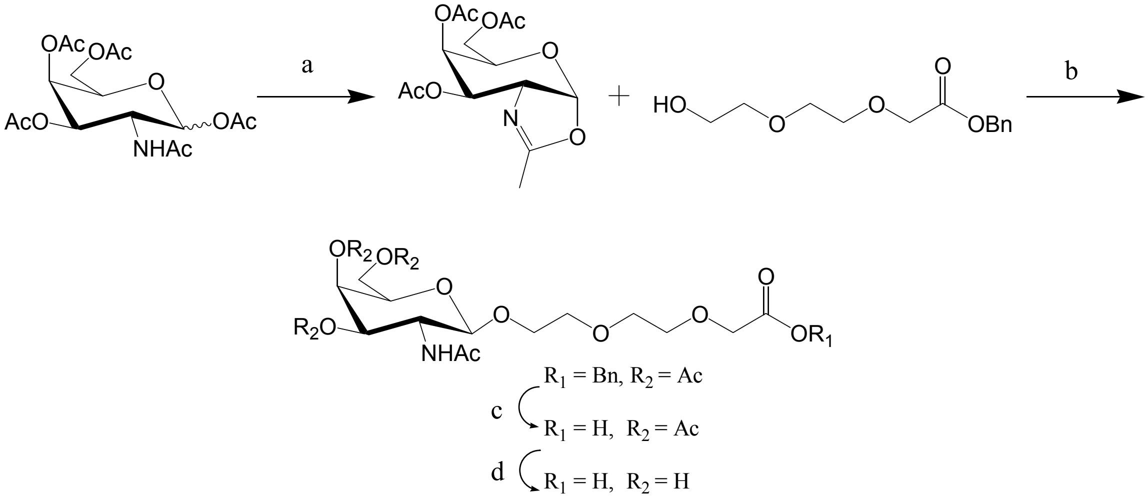

Scheme 6.1. Synthesis of GalNAc-carboxylic acid ligand.[16] Reagents: (a) TMSOTf, (b) TMSOTf, (c) H2/Pd/EtOAc and (d) NaOMe.

In place of the benzyl ester, similar protected amine compounds can be used, but the reaction would only be simplified slightly.

Binding studies have compared interactions of different acylated derivatives of galactosamine to RHL-1, the major subunit of the rat ASGPr.[13, 17] As the length of the acyl side chain increased from formyl to propionyl, affinity increased with the propionyl derivative having approximately 8 times stronger binding than the methyl derivative (GalNAc). A thioacetyl derivative (GalNSAc) was found to bind slightly better than the propionyl derivative, while steric hindrance is suspected of reducing binding of the thiopropionyl derivative. GalNSAc bound 9 times stronger than did GalNAc.

By modifying the galactose structure, Lee[18] found that the axial 4-OH of galactose contributes strongly to binding between Gal or GalNAc and the carbohydrate recognition domain (CRD) of RHL-1. An equatorial 4-OH group is prohibitory to binding when the 2-acetamido group is present. It was also determined that the lectin can accommodate a bulky substituent at 6-OH of galactose, indicating that substituents on 6-

OH do not interact with the binding site, or that the binding site is spacious. Proposed molecular interaction between RHL-1 and GalNAc similarly depict the 6-OH group as directed out of the binding cavity. A negatively charged group at C-6 does interfere with binding, as do bulky aglycons α-anomerically linked to galactose.

In a follow-up study, Lee *et al.*[19] found that the methylene group (C-6) contributes to binding, with significantly decreased interaction for all compounds lacking the methylene group, such as those with methyl ester, carboxylic acid, amidine or amide substituents. Only slight improvements, of less than 50%, could be realized by varying this C-5 substituent. There appears to be a nonspecific and possibly hydrophobic interaction between the aglycon and the lectin, with increases in binding strength of up to an order of magnitude possible by modifying this unit. In particular, there appears to be a strong interaction between the lectin and an amidino group on the third atom from the anomeric carbon, while a 4-fold improvement could be realized from large hydrophobic aglycons such as 6-aminohexyl. Attachment of an acetyl group to 2-OH of methyl α-galactopyranoside increased its inhibitory power to that of GalNAc.

In considering additional sugar modification, there appears to be little potential for gain by modifying the C-5 substituent, and the methylene should be maintained. The strong binding and tight cavity indicate that modification of 4-OH is likely to prove fruitless. Modifications at C-2 have been made, and 7-9 times increase in binding affinity can be realized with propionyl or thioacetyl derivatives of GalNAc. These sugar modifications may be worthwhile since they are not as laborious as other selective sugar modifications. Since substituting the ether linkage for a thioether linkage did not significantly affect binding, opportunity appears to exist only at C-3 for additional structure modification. It is my opinion that the selective functionalization at this position is not immediately worth the considerable time commitment that would be required, since much can be learned more immediately from syntheses first of a monovalent GalNAc ligand, then a GalNPr ligand. Depending on the results of *in vivo* uptake experiments with these ligands, a decision would then be made to be content with one of these ligands, to proceed with synthesis of the bivalent ligand or to pursue further sugar modification. *A priori*, I believe that synthesis of a bivalent ligand will make a much more dramatic improvement on vector targeting than could additional sugar modification. Synthesis of the bivalent ligand may not be any more difficult than selectively modifying galactose at the C-3 position.

6.3 Future Consideration: Variation in Surface Density of Ligand

While a single ligand may bind a single cell-surface receptor, such interaction is not necessarily sufficient to result in the cascade of events leading to ligand internalization. It has been demonstrated that while proteins with more galactose residues per molecule have higher binding affinities with ASGPr,[18] 23 nm nanoparticles bearing 60 surface lactose molecules were about four times more effective at targeting hepatocytes than were 23 nm particles with over 300 lactose molecules.[20] The 23 nm nanoparticles bearing over 300 lactose molecules were taken up by Kupffer cells to a much greater extent than were 23 nm nanoparticles bearing 60 surface lactose molecules. This range of 60-300 lactose per 23 nm particle corresponds to about 6-30 *p*mol/cm^2 galactose on the nanoparticle surface. In the present study, surface galactose densities of about 30 *p*mol/cm^2 were employed, so additional gain may be realized by decreasing the surface density of galactose.

With 27 nm liposomes, Sliedregt *et al.*[21] found that at a loading ratio of 5% (w/w) of glycolipid targeting molecule, particles were primarily processed by the hepatic ASGPr. But at a targeting loading ratio of 50% (w/w) resulted primarily in Kupffer cell uptake. However, the increased specificity of GalNAc for hepatocytes appears to increase the loading window that still results in hepatocyte targeting,[22] with further benefit coming from incorporation of a triantennary GalNAc ligand into the liposome. Despite the decreased concern of Kupffer cell uptake with GalNAc ligand, there may still be an optimal ligand density on the surface to give maximum uptake into hepatocytes through the entire volume of the liver. Once GalNAc ligands are incorporated into the system, and optimal particle size for hepatocyte uptake is nailed down, the effect of ligand density could be investigated.

6.4 References

1. Davis, M. E.; Pun, S. H.; Bellocq, N. C.; Reineke, T. M.; Popielarski, S. R.; Mishra, S.; Heidel, J. D., Self-assembling nucleic acid delivery vehicles via linear, water-soluble, cyclodextrin-containing polymers. *Current Medicinal Chemistry* **2004,** 11, (2), 179-197.
2. Lee, Y. C.; Townsend, R. R.; Hardy, M. R.; Lonngren, J.; Arnarp, J.; Haraldsson, M.; Lonn, H., Binding of synthetic oligosaccharides to the hepatic Gal GalNac lectin–Dependence on fine-structural features. *Journal of Biological Chemistry* **1983,** 258, (1), 199-202.

3. Connolly, D. T.; Townsend, R. R.; Kawaguchi, K.; Bell, W. R.; Lee, Y. C., Binding and endocytosis of cluster glycosides by rabbit hepatocytes–Evidence for a short-circuit pathway that does not lead to degradation. *Journal of Biological Chemistry* **1982,** 257, (2), 939-945.

4. Stockert, R. J., The asialoglycoprotein receptor–Relationships between structure, function, and expression. *Physiological Reviews* **1995,** 75, (3), 591-609.

5. Rice, K. G.; Weisz, O. A.; Barthel, T.; Lee, R. T.; Lee, Y. C., Defined geometry of binding between triantennary glycopeptide and the asialoglycoprotein receptor of rat heptocytes. *Journal of Biological Chemistry* **1990,** 265, (30), 18429-18434.

6. Lee, R. T.; Lin, P.; Lee, Y. C., New synthetic cluster ligands for galactose/N-acetylgalactosamine-specific lectin of mammalian liver. *Biochemistry* **1984,** 23, (18), 4255-4261.

7. Biessen, E. A. L.; Beuting, D. M.; Roelen, H.; Vandemarel, G. A.; Vanboom, J. H.; Vanberkel, T. J. C., Synthesis of cluster galactosides with high-affinity for the hepatic asialoglycoprotein receptor. *Journal of Medicinal Chemistry* **1995,** 38, (9), 1538-1546.

8. Kichler, A.; Schuber, F., Comparative affinity of synthetic multi-antennary galactosyl derivatives for the Gal/GalNAc receptor of rat hepatocytes and peritoneal macrophages. *Journal of Drug Targeting* **1998,** 6, (3), 201-205.

9. Andre, S.; Frisch, B.; Kaltner, H.; Desouza, D. L.; Schuber, F.; Gabius, H. J., Lectin-mediated drug targeting: Selection of valency, sugar type (Gal/Lac), and spacer length for cluster glycosides as parameters to distinguish ligand binding to C-type asialoglycoprotein receptors and galectins. *Pharmaceutical Research* **2000,** 17, (8), 985-990.

10. Sarkar, M.; Liao, J.; Kabat, E. A.; Tanabe, T.; Ashwell, G., Binding-site of rabbit hepatic lectin. *Journal of Biological Chemistry* **1979,** 254, (9), 3170-3174.

11. Baenziger, J. U.; Maynard, Y., Human hepatic lectin–Physiochemical properties and specificity. *Journal of Biological Chemistry* **1980,** 255, (10), 4607-4613.

12. Lee, R. T.; Lee, Y. C., Facile synthesis of a high-affinity ligand for mammalian hepatic lectin containing three terminal N-acetylgalactosamine residues. *Bioconjugate Chemistry* **1997,** 8, (5), 762-765.

13. Kolatkar, A. R.; Leung, A. K.; Isecke, R.; Brossmer, R.; Drickamer, K.; Weis, W. I., Mechanism of N-acetylgalactosamine binding to a C-type animal lectin carbohydrate-recognition domain. *Journal of Biological Chemistry* **1998,** 273, (31), 19502-19508.

14. Ozaki, K.; Lee, R. T.; Lee, Y. C.; Kawasaki, T., The differences in structural specificity for recognition and binding between asialoglycoprotein receptors of liver and macrophages. *Glycoconjugate Journal* **1995,** 12, (3), 268-274.

15. Fadden, A. J.; Holt, O. J.; Drickamer, K., Molecular characterization of the rat Kupffer cell glycoprotein receptor. *Glycobiology* **2003,** 13, (7), 529-537.

16. Westerlind, U.; Westman, J.; Tornquist, E.; Smith, C. I. E.; Oscarson, S.; Lahmann, M.; Norberg, T., Ligands of the asialoglycoprotein receptor for targeted gene delivery, part 1: Synthesis of and binding studies with biotinylated cluster glycosides containing N-acetylgalactosamine. *Glycoconjugate Journal* **2004,** 21, (5), 227-241.

17. Iobst, S. T.; Drickamer, K., Selective sugar binding to the carbohydrate recognition domains of the rat hepatic and macrophage asialoglycoprotein receptors. *Journal of Biological Chemistry* **1996,** 271, (12), 6686-6693.

18. Lee, R. T., Binding-site of the rabbit liver lectin specific for galactose N-acetylgalactosamine. *Biochemistry* **1982,** 21, (5), 1045-1050.

19. Lee, R. T.; Myers, R. W.; Lee, Y. C., Further-studies on the binding characteristics of rabbit liver galactose N-acetylgalactosamine-specific lectin. *Biochemistry* **1982,** 21, (24), 6292-6298.

20. Bijsterbosch, M. K.; Vanberkel, T. J. C., Uptake of lactosylated low-density-lipoprotein by galactose-specific receptors in rat-liver. *Biochemical Journal* **1990,** 270, (1), 233-239.

21. Sliedregt, L.; Rensen, P. C. N.; Rump, E. T.; van Santbrink, P. J.; Bijsterbosch, M. K.; Valentijn, A.; van der Marel, G. A.; van Boom, J. H.; van Berkel, T. J. C.; Biessen, E. A. L., Design and synthesis of novel amphiphilic dendritic galactosides for selective targeting of liposomes to the hepatic asialoglycoprotein receptor. *Journal of Medicinal Chemistry* **1999,** 42, (4), 609-618.

22. Rensen, P. C. N.; Sliedregt, L.; Ferns, A.; Kieviet, E.; van Rossenberg, S. M. W.; van Leeuwen, S. H.; van Berkel, T. J. C.; Biessen, E. A. L., Determination of the upper size limit for uptake and processing of ligands by the asialoglycoprotein receptor on hepatocytes *in vitro* and *in vivo*. *Journal of Biological Chemistry* **2001,** 276, (40), 37577-37584.

APPENDICES

APPENDIX A: GALACTOSE SURFACE CONCENTRATION DETERMINATION

APPENDIX B: NANOPARTICLE EXOCYTOSIS BY FRESHLY ISOLATED, CULTURED HEPATOCYTES

APPENDIX C: ISOLATION OF NON-PARENCHYMAL LIVER CELLS AFTER NANOPARTICLE INJECTION

APPENDIX D: EFFECT OF NANOPARTICLE DOSE ON UPTAKE BY SUSPENDED HEPATOCYTES

Appendix A: Galactose Surface Concentration Determination

As described in the Methods and Materials section of Chapter 3, the surface density of galactose on the nanoparticles was determined with the Amplex Red Galactose/Galactose Oxidase Kit from Molecular Probes. However, comparison to a galactose standard curve at 10-30 minutes, as suggested in the kit, did not yield reproducible results.

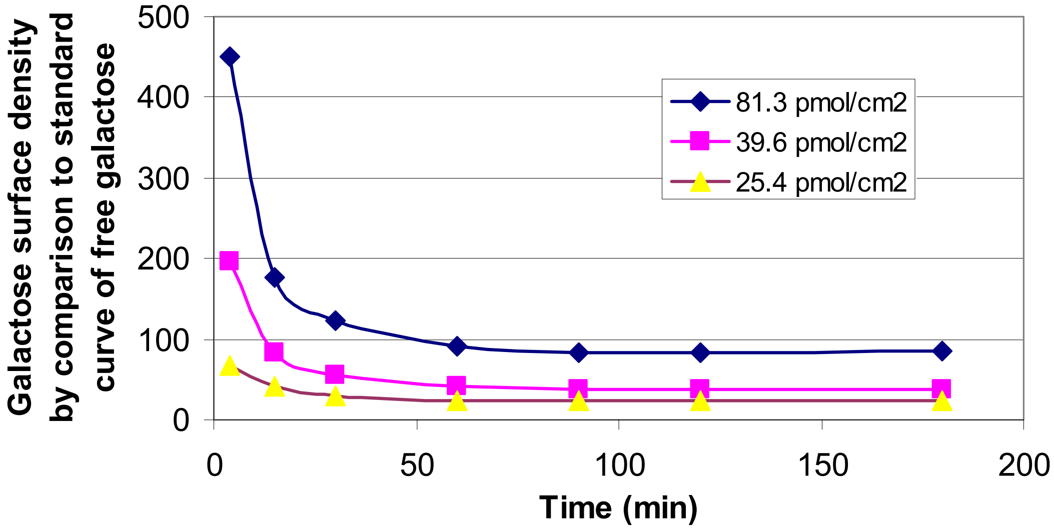

Figure A.1. Calculated surface density of galactose on nanoparticle surfaces by comparison to a standard curve of free galactose in solution.

As shown in Figure A.1, the calculated surface density of galactose varied considerably over time, as determined by comparison to a standard curve of 6 different concentrations of galactose in solution. This difference can be explained by the high local concentration of galactose on the nanoparticle surface. After diffusing to find a single nanoparticle, the galactose oxidase enzyme is able to quickly jump from galactose to galactose on the nanoparticle surface. However, in solution, the enzyme must diffuse much longer distances between galactose molecules at every jump. Therefore, reaction on the nanoparticle surface occurs much more quickly than does oxidation of galactose in solution. Since the rate of oxidation of galactose ultimately defines the measured absorbance of the solution, an artificially high concentration of galactose on the nanoparticle surfaces is initially measured. Only after about 120 minutes does the calculated surface density of galactose level off. The reported values of galactose surface density are taken as averages of multiple measurements at times greater than 120 minutes. Glucose was found to have no reactivity in this system, and methoxy-terminated nanoparticles of all sizes were correctly identified at all times as having no galactose on their surfaces.

Appendix B: Nanoparticle Exocytosis by Freshly Isolated, Cultured Hepatocytes

Nanoparticle type	% Dose in Lysate, Warm Wash	% Dose in Lysate, Cold Wash
Gal-50	14.9%	21.9%
MeO-50	7.7%	9.0%
Gal-140	0.9%	1.6%
MeO-140	1.0%	1.5%

Table B.1. Effect of wash buffer temperature on dose of nanoparticles following incubation with freshly isolated hepatocytes. After removal of nanoparticle-containing media, wash buffer of either $37^{O}C$ or $2^{O}C$ was incubated on the plated cells for 5 minutes. Wash buffer was then removed, cells were lysed and fluorescence of cell lysate was compared to standard curves of nanoparticles in unadulterated hepatocyte lysate.

As shown in Table B.1, exocytosis of nanoparticles appears to be a significant concern. While about 22% of the Gal-50 dose was present in hepatocytes following a 5 minute wash with cold buffer, only about 15% of the dose was present after a similar wash with warm buffer. Similar behavior was seen in all other nanoparticles studied.

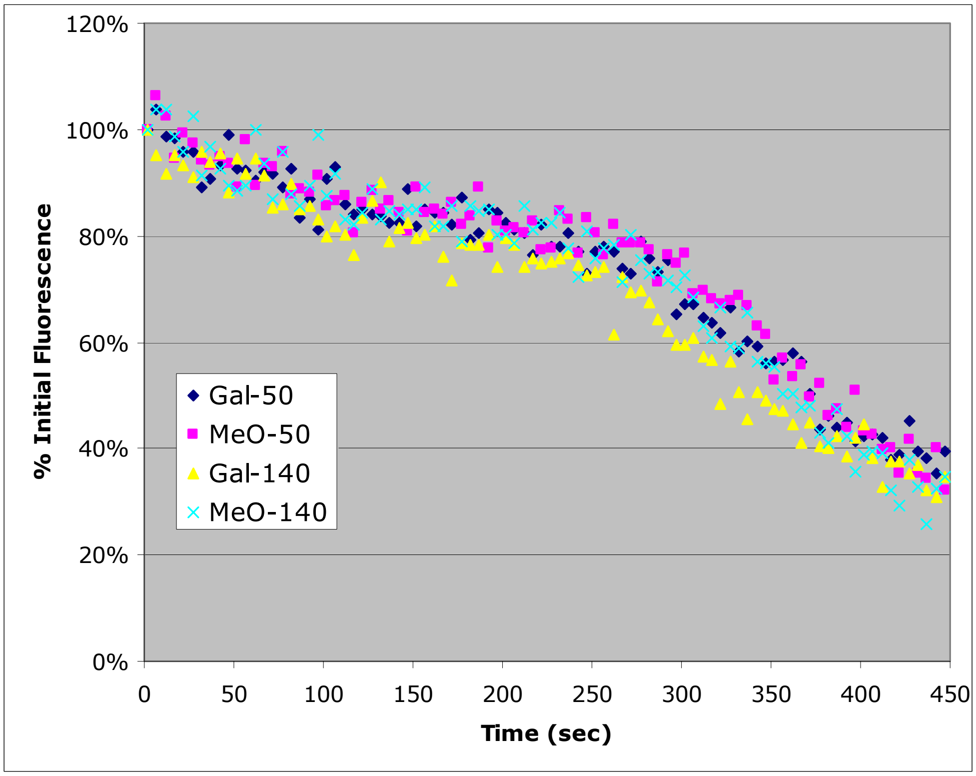

Figure B.1. Kinetics of exocytosis of nanoparticles from suspended freshly isolated hepatocytes.

In Figure B.1, the rapid rate of exocytosis of nanoparticles is seen. In this experiment, hepatocytes were incubated at 37^{O}C with nanoparticles for 30 minutes. Nanoparticle-containing media was then removed, hepatocytes were resuspended in fresh media and data collection was begun within 10 seconds. Despite the relatively low uptake of 140 nm nanoparticles by suspended hepatocytes, the kinetic exocytosis profiles of all four nanoparticles collapse onto one curve. Based on this result, it may be suggested that the primary mechanism of exocytosis of all four nanoparticles by suspended hepatocytes is similar.

Rudolph and Regoeczi,[1] working with suspended rat hepatocytes, observed a rapid release of pinocytosed material, while material internalized via receptor-mediated endocytosis was released more slowly. Within 7.5 minutes, only about 20% of the dose internalized by pinocytosis remained. This is not dissimilar from the results shown in Figure B.1 with about 35% of the dose remaining after that time.

Binding and endocytosis of ASGPr appear to be maintained through a continuous reutilization of plasma membrane receptors rather than through their replacement from the intracellular receptor pool that is known to exist for ASGPr.[2] Even if Gal-50 are being internalized by an ASGPr-mediated mechanism, there is a legitimate concern then that the ligand may be caught in this short-circuit pathway of receptor recycling that has been shown to occur with a $t_{1/2}$ of about 4 minutes.[3] Independent of the mechanism, quantitation of nanoparticle uptake by hepatocytes *in vivo* is complicated by such rapid exocytosis.

B.1 References

1. Rudolph, J. R.; Regoeczi, E., Relationship between pinocytic rate and uptake of transferrin by suspended rat hepatocytes. *Biology of Metals* **1991,** 4, (3), 166-172.
2. Stockert, R. J.; Howard, D. J.; Morell, A. G.; Scheinberg, I. H., Functional segregation of hepatic receptors for asialoglycoproteins during endocytosis. *Journal of Biological Chemistry* **1980,** 255, (19), 9028-9029.
3. Schwartz, A. L.; Fridovich, S. E.; Lodish, H. F., Kinetics of internalization and recycling of the asialoglycoprotein receptor in a hepatoma-cell line. *Journal of Biological Chemistry* **1982,** 257, (8), 4230-4237.

Appendix C: Isolation of Non-Parenchymal Liver Cells after Nanoparticle Injection

Unlike the rapid exocytosis observed following nanoparticle uptake by hepatocytes, no evidence of nanoparticle exocytosis was observed in cultured Kupffer cells. This result is in agreement with a literature finding[1] that after phagocytosis of carbon particles, Kupffer cells entered a physiological state where receptor recycling does not take place. We may therefore consider isolating Kupffer cells following tail-vein injection of nanoparticles without concern of misrepresented uptake data due to nanoparticle exocytosis.

Quantification of uptake by individual cell-types in the liver would facilitate identification of relationships between nanoparticle structure and *in vivo* response. Along these lines, we injected $8\text{x}10^{11}$ beads per 20 g mouse, then isolated non-parenchymal cells after 20 minutes. Non-parenchymal liver cells were isolated by the Non-parenchymal Liver Cell Core of the Research Center for Alcoholic Liver and Pancreatic Diseases, as previously published.[2] FACS was performed at the Flow Cytometry Core at the USC Health Sciences campus.

Bead Type	% FITC-positive Kupffer cells	% FITC-positive Hepatic stellate cells
Gal-50	29.30 +/- 4.72	<1%
MeO-50	3.37 +/- 0.49	<1%
Gal-140	76.88 +/- 3.03	<1%
MeO-140	28.76 +/- 3.01	<1%

Table C.1. Fraction of nanoparticle-containing Kupffer cells after their isolation from mouse livers that were exposed to nanoparticles by tail-vein injection of $8*10^{11}$ nanoparticles per 20 g Balb/c mouse.

In Table C.1, we can clearly see that Gal-140 are primarily taken up by Kupffer cells, and that nearly all Kupffer cells contain Gal-140. Though almost 30% of Kupffer cells contain MeO-140 nanoparticles, the mean fluorescence of MeO-140-containing Kupffer cells was less than 10% of the mean fluorescence of Gal-140-containing Kupffer cells. Further, a wide distribution of fluorescence values were seen following Kupffer cell exposure to Gal-140, while a narrow distribution was seen in Kupffer cells exposed to MeO-140. Therefore, we see that not only is the percentage of Kupffer cells that phagocytosed MeO-140 much lower than the percentage that phagocytosed Gal-140 (29% versus 77%), the number of beads taken up by the average Kupffer cell is also much lower for MeO-140.

In this experiment, the percent of FITC-positive Kupffer and Hepatic stellate cells is determined after tail-vein injection in mice. The percentage of FITC-positive hepatocytes could not be determined similarly due to rapid exocytosis of nanoparticles from hepatocytes. Additionally, because the data shown in Table C.1 for 50 nm and 140 nm nanoparticles were collected months apart with different instrument settings, it is impossible to accurately compare the mean fluorescence values of 50 nm and 140 nm nanoparticles. Including all liver cell types, each injected dose contains approximately 4000 nanoparticles per cell, so it is conceivable to have 100% FITC-positive cells, with each cell having internalized 40 nanoparticles, and only 1% total uptake. Therefore, direct comparison of the data presented in Figure C.1 to the data presented in Figure 5.3 is not possible.

We also see that almost 30% of Kupffer cells exposed to Gal-50 have internalized some of the nanoparticles. By microscopy, we saw that hepatocytes were the primary site of internalization of Gal-50, but clearly there is room for increased specificity. In the future directions section of this report, the next steps in ligand synthesis is discussed.

FACS analysis was also performed on Hepatic stellate cells, but no evidence of nanoparticle internalization was seen (Table C.1).

C.1 References

1. Kolb, H.; Vogt, D.; Kolbbachofen, V., Does the D-galactose receptor on Kupffer cells recycle? *Biochemical Journal* **1981,** 200, (2), 445.

2. Xiong, S. G.; She, H. Y.; Takeuchi, H.; Han, B.; Engelhardt, J. F.; Barton, C. H.; Zandi, E.; Giulivi, C.; Tsukamoto, H., Signaling role of intracellular iron in NF-kappa B activation. *Journal of Biological Chemistry* **2003,** 278, (20), 17646-17654.

Appendix D: Effect of Nanoparticle Dose on Uptake by Suspended Hepatocytes

As described in the Methods section, hepatocytes were detached from 10 cm^2 plates and resuspended in colorless, complete hepatocyte media. Following overnight incubation at $37^{O}C$ and 5% CO_2, the cells were spun down, resuspended in colorless media without FBS or Cu^{2+} or Zn^{2+} ions and incubated for an additional two hours. The cells were then washed, resuspended and counted, filtered and distributed to individual tubes for experimentation. Following appropriate incubation with beads, cell suspensions were transferred to FACS tubes on ice.

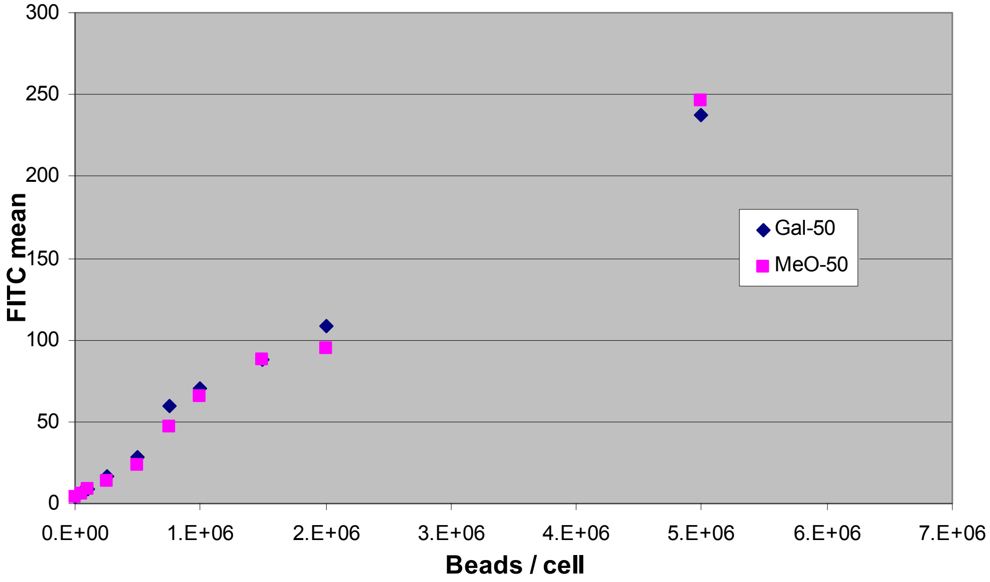

Figure D.1. Effect of nanoparticle dose on uptake into suspended hepatocytes, in media containing Cu^{2+} and Zn^{2+} ions.

The importance of Cu^{2+} and Zn^{2+} ion-removal prior to uptake experiments is shown by the results in Figure D.1. In that experiment, suspended hepatocytes were maintained in colorless D-MEM/F-12 media (Invitrogen) until the experiment was begun. Gal-50 or MeO-50 nanoparticles were added to the hepatocytes in D-MEM/F-12 medium and incubated for 45 minutes at 37^{O}C under 5% CO_2 atmosphere to allow equilibrium to be reached. The presence of galactose on the nanoparticle surface has no impact on uptake relative to the nontargeted equivalent, MeO-50.

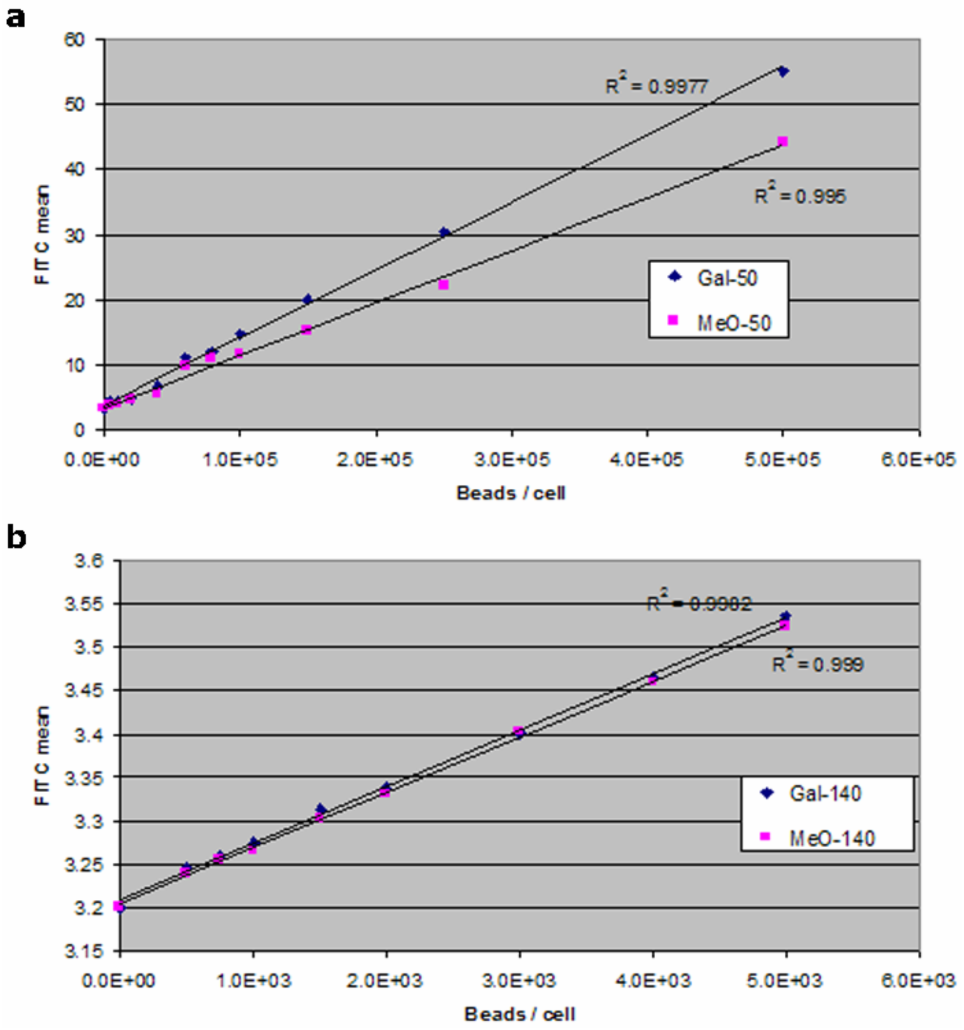

Figure D.2. Effect of bead concentration on mean fluorescence of suspended primary hepatocytes.

Incubation of hepatocytes in Opti-MEM media that does not contain Cu^{2+} or Zn^{2+} ions for two hours, followed by cell wash in Opti-MEM, allows the impact of galactose to be seen (Figure D.2). The strong linear correlation between FITC mean and nanoparticle dose is in agreement with the hypothesis that pinocytosis is the primary mechanism of nanoparticle uptake by suspended hepatocytes. However, this data alone does not conclusively single out any mechanism of uptake. In pinocytosis, the rate of uptake is directly proportional to the concentration of macromolecules or particles in the extracellular fluid, but rates of pinocytosis may be 20,000 times slower than uptake via ASGPr-mediated endocytosis.[1] Free galactose in solution with nanoparticles was not found to significantly impact uptake results.

D.1 References

1. Kjeken, R.; Mousavi, S. A.; Brech, A.; Gjoen, T.; Berg, T., Fluid phase endocytosis of [I-125]iodixanol in rat liver parenchymal, endothelial and Kupffer cells. *Cell and Tissue Research* **2001,** 304, (2), 221-230.